Investigation of the Phase transformation in FePtM nanoparticles (M= Ag, Cu) at atomic scale for optimized oxygen reduction catalysis.

Xu Chen

To cite this version:

Xu Chen. Investigation of the Phase transformation in FePtM nanoparticles (M= Ag, Cu) at atomic scale for optimized oxygen reduction catalysis.. Physics [physics]. Normandie Université; Université de Wuhan (Chine), 2019. English. NNT : 2019NORMC235 . tel-02469343

HAL Id: tel-02469343

https://theses.hal.science/tel-02469343v1

Submitted on 6 Feb 2020

THÈSE

Pour obtenir le diplôme de doctorat

Spécialité PHYSIQUE

Préparée au sein de l'Université de Caen Normandie

En cotutelle internationale avec Université de Hubei , CHINE POPULAIRE

Investigation of the Phase transformation in FePtM nanoparticles (M= Ag, Cu) at atomic scale for optimized oxygen reduction catalysis.

Présentée et soutenue par
Xu CHEN

Thèse soutenue publiquement le 29/11/2019 devant le jury composé de		
Mme VALERIE POTIN	Maître de conférences HDR, Université de Bourgogne	Rapporteur du jury
M. TIANYOU ZHAI	Professeur, Huazhong university of science and tech.	Rapporteur du jury
M. JUN CHEN	Professeur des universités, Université Caen Normandie	Membre du jury
M. QIMING LIU	Professeur, Université de Wuhan	Membre du jury
M. HAO WANG	Professeur, Hubei University	Membre du jury
M. YI WANG	Senior scientist, Max Planck Institute	Membre du jury
Mme JUN ZHANG	Professeur, Hubei University	Membre du jury
M. PIERRE RUTERANA	Directeur de recherche au CNRS, ENSICAEN	Directeur de thèse

Thèse dirigée par PIERRE RUTERANA, Centre de recherche sur les ions, les matériaux et la photonique (Caen)

Acknowledgements

First, I sincerely express my deepest gratitude to my thesis supervisors of Prof. Hao Wang, Dr. Pierre Ruterana and Prof. Peter A. van Aken, without whom none of the work presented here could have been possible. I am grateful to all of them for guiding and encouraging me throughout my doctoral study and for offering me the freedom and opportunity to develop my own ideas on FePt functional nanomaterial and characterization by Transmission Electron Microscopy.

Special thanks go to Dr. Yi Wang, my daily supervisor in Stuttgart center of electron microscopy (StEM). He is always active with academic ideas and patient with detail guidance. I have been and will always appreciate Dr. Yi Wang's selfless support and decisive help for my doctoral study.

I am very grateful to all the collaborators from the different institutes involved in my PhD project. It has been a pleasure to work with Prof. Hanbin Wang, Miss Dan Shu and Mr. Tianci Wu of Hubei University on studying FePt nanoparticle synthesis and their catalysis property. I would thank Kersten Hahn's and Peter Kopold's support for STEM and TEM experiments in StEM group of Max plank institute for solid state research. I appreciate Ute Salzberger and Marion Kelsch for professional assistance on general TEM sample preparation. I am very grateful to Marie Pierre Chauvat from ENSICAEN CIMAP, who trained me on TEM and FIB. It is not possible to list every one here, my grateful thanks go indeed to all not mentioned from the different teams and laboratories of StEM, CIMAP and Prof. Hao Wang's group in HUBU.

I would like to thank the following people that were involved not only in my work but also in everyday life in the laboratory, sincere thanks go to Dr. Surong Guo who was continuously sharing fruitful discussions from plasma to catalysis. I highly appreciated StEM administrative assistant, Caroline Heer, for her warm cares and great help in scheduling. I also want to acknowledge Prof. Jun Zhang, Dr. Hai Zhou, Dr. Houzhao Wan, Dr. Guokun Ma, who have been helpful with research.

I would like to thank my friends, Laifa, Quantong, Albert, Hichem, Hongguang, Yu-mi, Dan, Robin, Nilesh, Tao, Yuanshan, Chao, Xuejiao,…Thanks for all the fruitful discussions we have had and all the enjoyable moments we have spent together during these years.

The last but not the least, I would like to give my deepest gratitude to my family.

Table of contents

Abstract

Recently, proton-exchange-membrane fuel cells (PEMFC) have attracted considerable attention as a modern energy conversion device, due to their advantages of high efficiency, low emission and unlimited sources of fuels. They are predicted to constitute ultimate solutions to issues around novel electric vehicles and stationaries. The main challenge for PEMFC large–scale application is the problem surrounding the platinum catalysts used in their cathode, namely low activity and stability, and thus results in high Pt loading and high costs. Therefore, developing highly efficient catalysts for this cathodic oxygen reduction reaction (ORR) is the key towards the fabrication of commercial fuel cell devices. In this regard, chemical ordered FePt nanoparticles exhibit a high potential because of enhanced activity and durability simultaneously in acid operation environment. However, there are still challenges related to the synthesis of ordered FePt nanoparticles, and a fundamental understanding on their structure/performance relationship is still lacking. In this work, we carried out one–pot synthesis of these FePt nanoparticles by Ag/Cu additives with the objective to investigate their ordering structure and electrochemical catalysis performance, as well as performance enhancement. The superior activity of our samples has been demonstrated and state-of-the-art scanning transmission electron microscopes (STEM), with sub-angstrom scale spatial resolution, have been used to determine the corresponding structure of alloys. The main results are summarized as follows:

1. Uniform and chemical ordered FePtAg nanoparticles have been successfully synthesized by a one–pot method with octadecylamine solvent. Ag was adapted to *in-situ* promote phase transformation of FePt in high boiling temperature (320~345 °C) solvents. Magnetic measurements show that FePtAg nanoparticles with a high coercivity of 5.23 kOe have been successfully produced, this is significantly higher than from nanoparticles synthesized using hexadecylamine (2.84 kOe) and trioctylamine (2.81 kOe) solvents. Structural characterization demonstrated that the FePtAg particles synthesized in octadecylamine, with a diameter of 3.5 ± 0.5 nm, are smaller in size and more uniform than those synthesized in hexadecylamine and trioctylamine solvents. The octadecylamine, hexadecylamine and trioctylamine high boiling-temperature solvents play a significant role in shaping up the morphology, structure and magnetism of FePtAg nanoparticles, by governing the nucleation and growth of ordered FePtAg nanoparticles.

2. Ordered FePtCu nanoparticles are prepared by one–pot method, with controllable composition of 10% ~ 40% for Cu, 30% ~ 50% for Fe and Pt. The Cu alloying effect is found to be the driving force for FePt ordering in this synthesis method, which is effective up to a Cu content of 40%. The optimized core–shell CuFePt catalyst with Pt-enriched surface exhibits 0.5 A/mg$_{Pt}$ mass activity and a factor of 4 better than commercial Pt/C (0.13 A/mg$_{Pt}$). The current density of CuFePt drops only 3.0% after 1000 cycling measurement, demonstrating enhanced durability than Pt/C (34.2% decay). The morphology and structure evolutions between solid solution FePtCu alloy and core–shell CuFePt have been explained. The composition effects of Fe, Pt and Cu on structure of FePtCu nanoparticles has been investigated and it was shown that core–shell CuFePt formed for 20% atom ratio of Cu and more than 40% of Fe. The particle size increases with the Fe or Cu ratio, and the particles are sintered for Fe (50%) and Cu (> 20%). This study demonstrates that high performance *fct*–FePt ORR catalysts are not only ordered but also should have a core–shell structure.

3. To investigate the crystalline behavior of ordered FePtCu, *i. e.*, their morphology and elemental evolution during one–pot synthesis, *quasi-in-situ* and *in-situ*-heating work was carried out in TEM. It was found that core–shell CuFePt nanoparticles were initially formed with six branches shape at reaction time of 20 min. The particles size increased at 40 min but kept the same structure, which means that the system was still in anisotropic growth. For 1 h particles, they evolved into core–shell CuFePt with truncated–octahedron shape, most probably due to the surface atoms of these branches migrated onto 111 bulk surfaces. Finally, Cu diffused out from core and uniformly distributed in the particle at 2 h, forming solid-solution FePtCu alloy particles with spherical shape. Therefore, anisotropic growth, surface atoms diffusion and bulk atomic diffusion govern the FePtCu crystalline growth in sequence. The truncated–octahedron CuFePt nanoparticles (1 h) have a mass activity of 11.7 times higher than Pt/C, and exhibit 0.5% half-wave potential loss after 5000 potential cycles. The branched CuFePt nanoparticles (20 min) have a mass activity of 12.1 times higher than Pt/C, and show 3.1% half-wave potential loss after cycling; while the solid-solution FePtCu nanoparticles (2 h) have a mass activity of 5.3 times higher than Pt/C and show 2.9% mass activity loss after 5000 potential cycles. This work shows the way towards the synthesis of nanoparticle FePtCu alloys for high performance low–platinum nanostructures for oxygen reduction reaction.

Résumé

Récemment, les piles à combustible à membrane échangeuse de protons (PEMFC) ont attiré beaucoup d'attention en tant que dispositif de conversion d'énergie moderne, en raison de leurs avantages de combustibles à haut rendement, à faibles émissions et disposant de ressources illimitées. Ils devraient constituer la solution idéale aux problèmes liés aux nouveaux véhicules électriques et aux sources stationnaires. Le principal défi pour les applications à grande échelle de la PEMFC est le problème des catalyseurs au platine utilisés dans leur cathode, à savoir leur faible activité et leur stabilité, ce qui entraîne une charge élevée de Pt et des coûts élevés. Par conséquent, la mise au point de catalyseurs plus efficaces pour cette réaction de réduction de l'oxygène cathodique (RRO) est la clé de la fabrication de dispositifs de piles à combustible de niveau commercial. Dans cette optique, les nanoparticules de FePt offrent un potentiel élevé en raison d’une activité et d’une durabilité accrues dans un environnement de fonctionnement acide. Cependant, les meilleurs résultats ont été obtenus pour la phase ordonnée et la synthèse de nanoparticules FePt ordonnées pose encore des problèmes. Aussi, une compréhension fondamentale de leur relation structure/performance est-elle encore attendue. Dans ce travail, nous avons réalisé une synthèse « one-pot » de ces nanoparticules de FePt avec des additifs Ag/Cu dans le but d'étudier leurs performances pour une catalyse électrochimique, ainsi son optimisation. L'activité supérieure de nos échantillons a été démontrée dans cette recherche menée au microscope électronique à transmission à balayage (STEM) avec une résolution spatiale à l'échelle de l'angström, pour déterminer la structure et la chimie de ces alliages.

Les principaux résultats sont résumés comme suit:

1. Des nanoparticules de FePtAg ordonnées ont été synthétisées avec succès par une méthode « one-pot » avec un solvant octadécylamine. Ag a été adopté pour favoriser la transformation in situ de FePt dans des solvants à haute température d'ébullition (320 ~ 345 ° C). Des mesures magnétiques ont montré que les nanoparticules de FePtA ayant une coercivité élevée de 5,23 kOe ont été produites, ce qui est nettement supérieur au résultat sur des nanoparticules synthétisées à l'aide de solvants hexadécylamine (2,84 kOe) et

trioctylamine (2,81 kOe). La caractérisation structurale a démontré que les particules de FePtAg synthétisées dans l'octadécylamine, d'un diamètre de 3,5 ± 0,5 nm, ont une taille inférieure et sont plus uniformes que celles synthétisées dans les solvants hexadécylamine et trioctylamine. Les solvants octadécylamine, hexadécylamine et trioctylamine à haute température d'ébullition jouent donc un rôle important dans la formation de la morphologie, de la structure et du magnétisme des nanoparticules de FePtAg, en contrôlant la nucléation et la croissance de nanoparticules ordonnées de FePtAg.

2. En parallèle, les nanoparticules de FePtCu ont été préparées selon la méthode « one-pot », avec une composition contrôlable de 10% à 40% pour le Cu, de 30% à 50% pour le Fe et le Pt. L'effet d'alliage de Cu s'est avéré être la force motrice pour l'activité de l'alliage FePt dans cette méthode de synthèse, avec efficacité jusqu'à une teneur en Cu de 40%. Le catalyseur cœur/enveloppe optimisé Cu FePt avec une surface enrichie en Pt présente une activité massique de 0,5 A / mgPt soit 4 fois supérieure à celle du Pt/C commercial (0,13 A / mgPt). La densité de courant de CuFePt ne chute que de 3,0% après 1000 mesures cycliques, démontrant ainsi une durabilité accrue par rapport au Pt/C. La morphologie cœur-coquille et l'évolution de structure vers l'alliage FePtCu en solution solide ont été expliquées. Il a été démontré que, pour les nanoparticules de FePtCu, la structure coeur-coquille avait lieu pour un rapport atomique à 20% de Cu et à plus de 40% de Fe. La taille des particules augmente avec le rapport Fe ou Cu et les particules sont agglomérées pour Fe (50%) et Cu (> 20%). Cette étude a démontré que les catalyseurs haute performance fct – FePt ORR sont non seulement ordonnés, mais devraient au mieux avoir une structure avec cœur riche en Cu et enveloppe riche en Pt.

3. Pour étudier la formation du FePtCu ordonné, i. e., la morphologie et l'évolution élémentaire au cours de la synthèse « one-pot », une étude du comportement en température a été effectué par STEM. Cette investigation nous a permis de mettre en évidence que les nanoparticules de CuFePt cœur-coquille apparaissent d'abord sous une forme de six branches pour un temps de réaction de 20 min. La taille des particules augmente à 40 min tout en conservant la même structure, ce qui signifie que le système est encore en croissance anisotrope. A une heure, les nanoparticules deviennent du CuFePt en

forme d'octaèdre tronqué, probablement dû au fait que les atomes des branches ont migré sur des surfaces {111}. Enfin, à 2 h de réaction, le Cu diffuse hors du cœur de la structure et se répartit uniformément dans la particule FePtCu qui devient alors une solution solide de forme sphérique. Par conséquent, la croissance anisotrope, la diffusion des atomes de surface et la diffusion atomique régissent la croissance cristalline de FePtCu selon le temps de fabrication dans la méthode « one-pot ». En ce qui concerne les performances, les nanoparticules de CuFePt d'octaèdre tronqué (1 h) ont une activité massique 11,7 fois supérieure à celle de Pt / C et présentent une perte de potentiel de 0,5% après 5000 cycles de potentiel. Les nanoparticules de CuFePt ramifiées (20 min) ont une activité de masse 12,1 fois supérieure à celle de Pt/C et montrent une perte de potentiel de demi-onde de 3,1% au même stage d'utilisation. Alors que les nanoparticules de FePtCu en solution solide (2 h) ont une activité massique 5,3 fois supérieure à celle du Pt/C, elles présentent une perte d'activité massique de 2,9% après 5000 cycles. Ainsi, la technique suivie pour la fabrication de nos nanoparticules s'avère donc efficace pour optimiser l'activité catalytique dans la réduction de l'oxygène en ce qui concerne l'activité, la durabilité et la réduction des coûts par utilisation de moins de Pt.

Chapter 1

State of the art

Novel energy materials and techniques are attracting renewed attentions, due to the constantly growing demand of energy and increasing environmental issues caused by consumption of fossil fuels.[1-3] It is a challenge for countries all over the world to develop green and efficient energy generation and energy storage devices. Fuel cells (FC) are electrochemical energy conversion devices that transform chemical energy of fuels into electricity.[4-5] In 1838, Sir William Grove invented the first fuel cell. Nearly a century later in 1932, the first commercial fuel cell was invented, following the invention of the H_2–O_2 fuel cell by Francis Thomas Bacon. The alkaline fuel cell, also known as the Bacon fuel cell, has been used in NASA space programs since the mid-1960s to generate power for satellites and space capsules. Since then, fuel cells have attracted extensive attentions of scientific and technical researchers in many other directions, such as primary/backup power for commercial, industrial and residential buildings, as well as stationaries. They are also used to power transportations in civil and military vehicles.

As compared to batteries, fuel cells do not need recharging as long as fuels are constantly supplied.[6] As compared to thermal engine, it has advantages of high energy conversion efficiency, low carbon emission, low noise, and choice of renewable energy sources.[7] According to the electrolyte used, fuel cells can be classified into five categories, *i. e.*, proton exchange membrane FC, alkaline FC (AFC), phosphoric acid FC (PAFC), molten carbonate FC (MCFC) and solid-state oxide FC (SOFC).[8] Their operation and application properties can be summarized in Table 1.1. The energy efficiency of fuel cells is typically between 40 % and 65 % (chemical-energy to electric-energy conversion), however, if a cogeneration is utilized to capture the waste heat, more than 85% energy conversion efficiency can be obtained. According to Pike Research prediction, the fuel cell market is growing and the stationary fuel cell market will reach 50 GW in 2020. Among fuel cells, PEMFC is characterized by its high efficiency, low working temperature, simplicity and quick start–up.[9-10] It is predicted to be an adequate solution to issues around novel energy vehicles, as well as high potential for portable electronics and stationaries.[11-12]

Table 1.1 Operating and applicable properties of main types of fuel cells[13]

Type of fuel cell	Electrolyte	Working Temp	Efficiency	Advantages	Challenges	Applications
PEMFC	Perfluoro-sulfonic acid	50 ~ 80 (°C)	45 ~ 60	• Low temperature • Quick start up • Electrolyte	• Expensive catalyst • Sensitive to fuel impurities	• Transportations, vehicles, buses • Distributed generation • Portable power • Backup power
AFC	KOH	60 ~ 90 (°C)	40 ~ 60	• Alkaline electrolyte, high performance • Low cost components	• Sensitive to CO_2 in fuel and air • Electrolyte management	• Military • Space
PAFC	H_3PO_4	160 ~ 220 (°C)	40 ~ 55	• Increased tolerance to fuel tolerance • High temperature enables *CHP*	• Expensive catalyst • Long start up • S sensitive	• Distributed generation
MCFC	Solution of lithium, sodium, and potassium carbonates	600 ~ 700 (°C)	60 ~ 65	• High efficiency • Fuel flexibility • Compatible with various catalyst • Suitable for *CHP*	• High temperature damage • Long start up • Low power density	• Distributed generation • Electric utility
SOFC	Oxides ceramics	800~1000 (°C)	55 ~ 65	• High efficiency • Fuel flexibility • Compatible with various catalyst • Solid electrolyte • Suitable for *CHP*	• High temperature corrosion and breakdown of cell components • Long start up and limits shutdowns	• Auxiliary power • Electric utility • Distributed generation

**CHP*: Combined Heat and Power

1.1. PEMFC

PEMFCs are considered as one of the most promising energy conversion devices of the 21th century. They have the potential to replace combustion engines due to their potentials of achieving higher efficiency and lower environment harmful gas emission. Still, for large-scale application, their performance needs to be further optimized and its cost should be reduced to a level that is competitive with current energy conversion devices.

1.1.1 PEMFC Description

In a PEMFC as shown in Fig. 1.1, the cathode is the most critical of the performance controlling component, the multifunctional bipolar plate and proton exchange membrane electrolyte are the second important components, as well as the water management in

PEMFC system. A PEMFC device has two electrodes, the cathode and anode electrodes, and electrolyte between them. The electrolyte is ion conducting but electron insulated. In addition, it need fuels, such as hydrogen gas and oxygen gas. Chemical reactions take place at these two electrodes, which generate potential difference between them and can be used to drive a load of external circuit, as shown by following equations[14]:

$$\text{Total reaction} \qquad 2\ H_2 + O_2 \rightarrow 2\ H_2O \qquad E_{\text{cell}}{}^0 = 1.23\ \text{V} \tag{1.1}$$

$$\text{Anode} \qquad H_2 \rightarrow 2\ H^+ + 2\ e^- \qquad E_a{}^0 = 0.00\ \text{V} \tag{1.2}$$

$$\text{Cathode:} \qquad O_2 + 4\ H^+ + 4\ e^- \rightarrow 2\ H_2O \qquad E_c{}^0 = 1.23\ \text{V} \tag{1.3}$$

Hydrogen oxidization reaction (HOR) takes place at the anode, meanwhile producing two protons and two electrons, as shown of eqn. (1.2). The protons diffuse through the anode and the electrolyte to the surface of cathode, whereas, the electrons pass through the external circuit to the cathode, which is the driving force for the load. Along the cathode side, protons and electrons can reduce oxygen molecules into water, as shown of eqn. (1.3). The reaction product is only water, which means this is a clean technology. H_2O can be split into H_2 and O_2 by electrolysis/photocatalysis techniques and this is a loop that governs this clean energy production cycle.

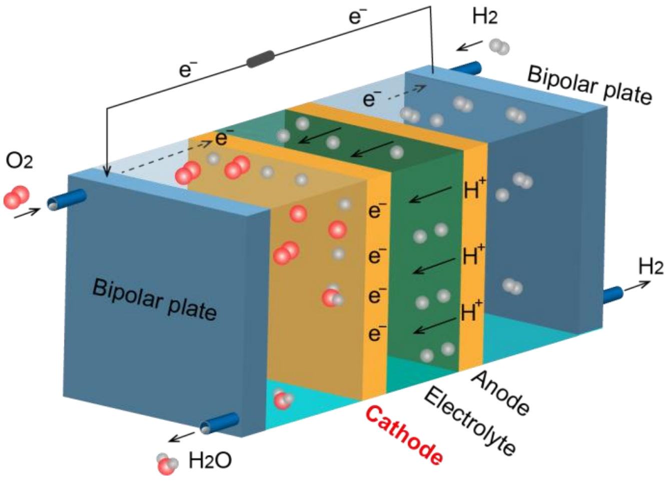

Fig. 1.1 An illustration of a PEMFC device.

1.1.2 PEMFC Applications

According to the output power between 1 W and 250 kW, PEMFC systems have three main applications of portable electronics, transportation, and stationary. For the systems, the working voltages are higher than theoretical output voltage of a single fuel cell of 1.23

V, and the PEMFC needs to be stacked in series to compile with the output voltage, and in parallel to generate the desired power density.

Among these applications, PEMFCs primarily focus on transportations, mainly due to their potential impact on the environment, e.g. the control of emission of the carbon dioxide and fuel sustainability.[15] Most issues are associated with the conventional internal combustion engines, which primarily depend on hydrocarbon fuels. The typical power range for this type of applications, such as passenger cars, utility vehicles, and buses, ranges from 20 kW to 250 kW.[16] Honda, Toyota, Hyndai, General Motors, *etc.* fuel cell vehicles have been demonstrated, e.g., DaimlerChrysler B-Class, Honda FCX, Chevrolet HydroGen, and Toyota FCHV, as shown in Fig. 1.2.[17] Mercedes-Benz did a world tour with their B-Class fuel cell vehicle in 2011. This hydrogen powered fuel cell vehicle was driven for more than 30 000 kilometers around the globe, starting and ending in Stuttgart. Great breakthroughs have been made by scientific and technical researchers, with a milestone event of Toyota, who firstly issued a commercial fuel cell vehicle *Mirai* in 2014.[18] Honda Clarity and Hyundai ix35 FCEV have also been introduced to the market recently. In China, Dalian Institute of Chemical Physics, Tsinghua University, Tongji University, Wuhan University of Technology, New Energy Power Cooperation, Shanghai Shenli Company, *etc.* research institutes or universities or companies are also making outstanding contributions to the development of fuel cells. Three fuel cell buses were selected for the third batch of new energy vehicles in 2019. The three fuel cell buses were developed by Zhongtong Bus (as shown in Fig. 1.2), Shanghai Shenlong and the Nantong Yukai, respectively. The successfully developed PEMFC power system has also been used in ships, submarines and aircraft.[13]

Fuel cell application on stationary offers even greater market opportunity than transportation, this is primarily focused on small scale (50–250 kW for decentralized use, or <10 kW for households). Wang *et al.* present and investigated a 5 kW hydrogen PEMFC system for a stationary power generator, including the key components, specifications, configuration and operation characteristics.[16, 19] It exhibits an energy conversion efficiency of more than 30%. Ladewig et al. analyzed another 5 kW PEMFC stack with 75 cells, which use a natural gas reformer and hydrogen purification membrane unit.[20] The system was installed in Belfort, France with natural gas from the local supply. Hwang and Zou investigated the combine heat and power (CHP) efficiency and achieved a high energy conversion efficiency of ~81%.[21]

Another promising application of PEMFC is portable power supply with power less than 100 W, and major electronics companies, such as Toshiba, Sony, Motorola, LG, and Samsung, have in-house research/design units for portable fuel cells. While, high cost and low durability are main challenges for these applications.

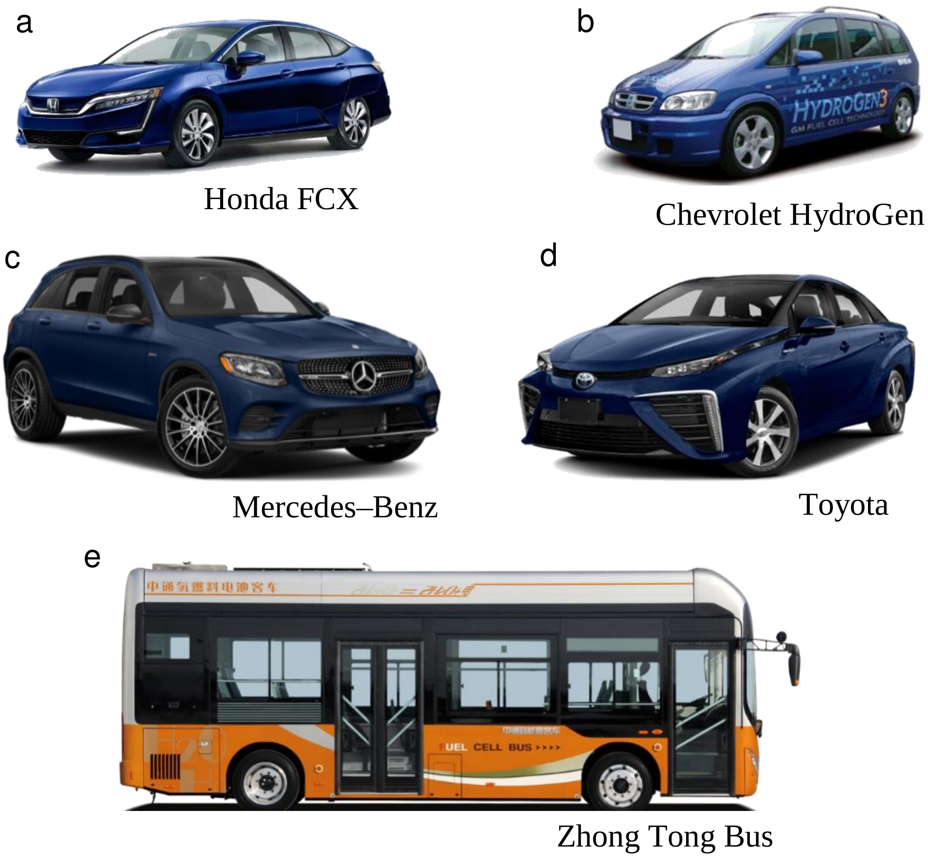

Fig.1.2 Fuel cell vehicles from different automakers. a) FCX by Honda. b) Chevrolet concept vehicle powered by hydrogen fuel cell. c) Mercedes-Benz Mercedes GLC F-Cell, commercially available since 2018. d) One of the first such sedan-like vehicles to be sold commercially since 2014 by Toyota . e) Hydrogen fuel cell of Zhongtong, LCK6900FCEV.

1.1.3 Challenges

The expected wide range of applications of PEMFC has not yet been attained due to the high cost and low durability. In the past years, the PEMFC cost has been reduced from \$275/kW of 2002, \$73/kW of 2008, and \$40/kW for today state-of-the-art PEMFCs.[15, 22] However, this is still higher than the US Department of Energy (DOE) near-term cost (\$30/kW) target for PEMFCs for transportation applications. Over 40% of the current cost of state-of-the-art PEMFCs arises from Pt catalysts used in the cathode. Meeting PEMFC lifetime requirements of 8,000 hours for cars with equivalent of 150,000 miles, as well as 20,000 hours for buses with less than 10% performance loss,[22] remains a challenge due to catalyst deactivation. The high power density (>1.0 W/cm^2) needed for transportation is still limited by inefficient mass transfer and charge transport in membrane electrode assemblies (MEAs), especially at ultra-low Pt loadings (<0.1 mgPt/cm^2).

Pt is known as the most efficient single metal catalyst for PEMFC cathode, *i.e.*, oxygen reduction reaction (ORR) catalysis, shows the volcano curve of ORR catalysts of Fig. 1.3a.[23] Moreover, carbon loaded platinum nanoparticles (Pt/C) is the state-of-the-art commercial fuel cell catalyst with best comprehensive performance (activity and durability in acid electrolyte), and it is used as a benchmark in laboratory to evaluate performance of new developed catalysts.[24] However, the ORR rate is around five orders of magnitude slower than the HOR at the anode. Consequently, the cathode of a PEMFC typically contains 80–90% of the total Pt in the stack, meanwhile, over 40% of the current cost of PEMFC arises from this Pt.[25-27] Due to the scarcity and high cost of platinum, the target total Pt–loading is required to be below 0.125 mg/cm^2 in 2020, according to the DOE requirements. At present, 0.4 mg/cm^2 or more catalysts are used in PEMFC cathode.[28] To output practical power density, an overpotential of 0.4 V usually generates due to the sluggish ORR kinetics, resulting in significantly decreased open circuit voltage of the PEMFC devices below the theoretical value of 1.23 volts.[29]

Thus, it is urgent to find substitution catalysts with high activity and low cost. In current investigations, low–Pt catalyst and non–Pt catalyst are the two main directions. For now, the non–Pt catalyst, including carbide and nitride, are still inefficient under acid and electrochemical fuel cell environment. For low–Pt catalyst, we can see from Fig. 1.3a that the activity of Pt does not reach the top of catalyst volcano curve. A use of alloy effect has been an important breakthrough in ORR catalyst research; this allowed alloying Pt with cheaper transition metals M (Fe, Co, Ni, *etc.*) can improve the activity of Pt atoms, as shown in Fig. 1.3b.[30-33] As ORR is a heterogeneous electrocatalysis reaction, surface Pt atoms only take part in a catalytic reaction but not the bulk Pt atoms. In PtM alloys, cheaper transition metal atoms substitute the positions of bulk platinum as compared to pure Pt nanocrystal, which can reduce the usage of Pt content and thus reducing the cost.[34] Among these materials, ordered FePt is quite promising due to their simultaneously enhanced activity and durability in acid fuel cell environment.[35]

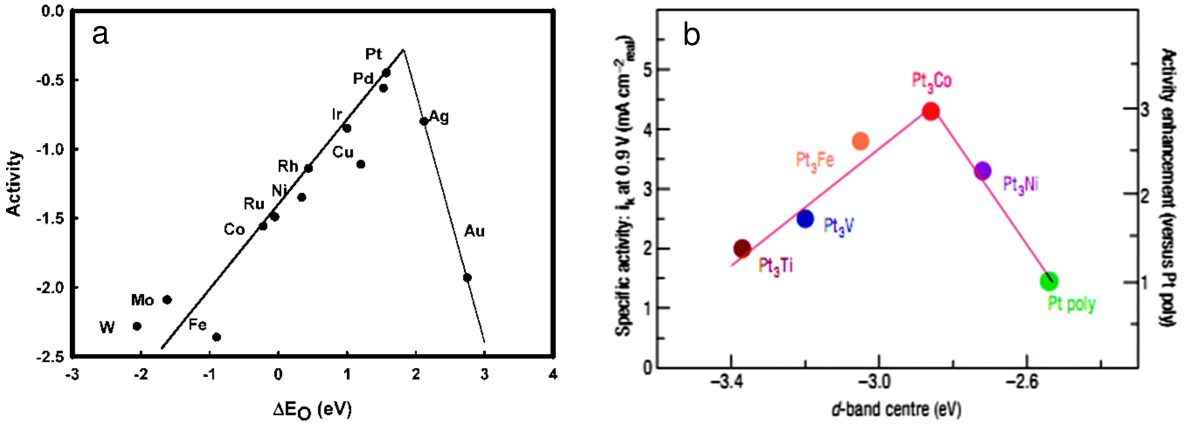

Fig. 1.3. a) Volcano curve of metal catalysts' activity for ORR.[23] b) Volcano curve of Pt-based alloy catalyst for ORR.[36]

1.2. ORR catalyst development

1.2.1 Basics of ORR

The electrochemistry of oxygen has been extensively and intensively studied, due to its fundamental complexity and importance for many practical systems. Oxygen reduction is a critical reaction of biological respiration in life process, a half reaction of metal air batteries, and a cathodic reaction of electrocatalysis cells. Oxygen reduction is also of fundamental interest because it is the rate that determines step for the overall performance of PEMFC. Pt and Pt-based catalysts are the most important catalyst for oxygen reduction for PEMFC,[37-38] so the mechanisms of oxygen reduction at Pt will be the first focus in the following discussion. In acid aqueous environment, oxygen reduction occurs roughly through two different pathways: either a four-electron reduction pathway from O_2 to H_2O or a two-electron pathway from O_2 to H_2O_2. Thermodynamic electrode potentials of ORR in different electrolytes are summarized in Table 1.2.[37] The 4-electron direct pathway is highly preferred to occur at potentials close to its thermodynamic electrode potential of 1.23 V for fuel cell applications, meanwhile with and attaining satisfactory reaction speed. As for the mechanisms, the 2-electron reduction pathway is used for producing H_2O_2 in industry, however, it is harmful for ORR efficiency and fuel cell performance as it reduces the effective electron transfer number. The 1-electron reduction pathway is of importance in the exploration of the ORR mechanism. In this study, we measured the ORR activity in acid electrolyte.

Table 1.2 Thermodynamic electrode potentials of electrochemical oxygen reductions[37]

Electrolyte	ORR reactions	Thermodynamic electrode potential at standard conditions (V)
Acidic electrolyte	$O_2 + 4H^+ + 4e^- \rightarrow H_2O$	1.229
	$O_2 + 2H^+ + 2e^- \rightarrow H_2O_2$	0.70
	$H_2O_2 + 2H^+ + 2e^- \rightarrow 2H_2O$	1.76
Alkaline electrolyte	$O_2 + H_2O + 4e^- \rightarrow 4OH^-$	0.401
	$O_2 + H_2O + 2e^- \rightarrow HO_2^- + OH^-$	–0.065
	$HO_2^- + H_2O + 2e^- \rightarrow 3OH^-$	0.867

As conventionally admitted, the first step of ORR catalysis is adsorption of O_2 on the Pt surface. Then reduction reactions of O_2 on the surface of Pt, followed by a product desorption processes. To develop efficient fuel cell catalyst, it is necessary to understand the ORR dynamics at atom or molecular scale, and to find the rate determine step. To this end, density functional theory (DFT) study, combined with experimental investigation, has been a powerful tool to investigate the binding energy for intermediates of ORR, such as O_2, O, OH, OOH, H_2O_2 and H_2O.[39-40] Fig. 1.4 shows all the possible O_2 reduction processes on (111) surface of Pt, with all the reaction intermediates according to the calculation results.

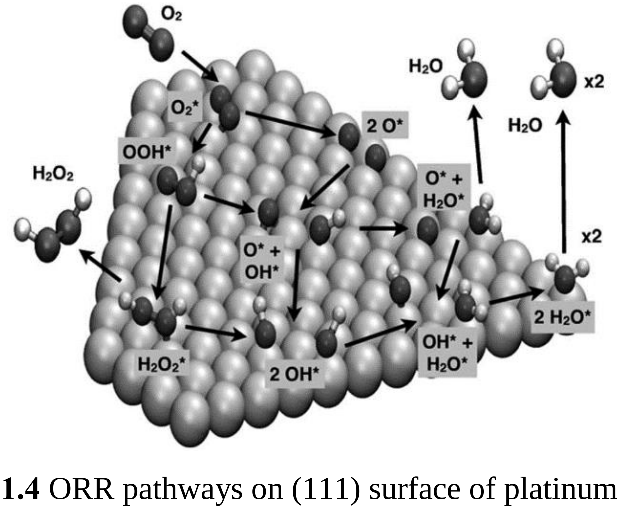

Fig. 1.4 ORR pathways on (111) surface of platinum.[40]

It is commonly accepted that ORR catalyzed by Pt–based catalyst occurs predominately through four-electron transfer pathways. Thus, these pathways can be simplified into a Dissociative pathway and an Associative pathway, as shown in following equations.[23, 41]

Dissociative pathway

$$O_2^* \rightarrow 2O^* \tag{1.4}$$

$$O^* + H^+ + e^- \rightarrow OH^* \tag{1.5}$$

$$OH^* + H^+ + e^- \rightarrow H_2O \tag{1.6}$$

Associative pathway

$$O_2^* + H^+ + e^- \rightarrow OOH^* \tag{1.7}$$

$$OOH^* + H^+ + e^- \rightarrow H_2O + O^* \tag{1.8}$$

$$O^* + H^+ + e^- \rightarrow OH^* \tag{1.9}$$

$$OH^* + H^+ + e^- \rightarrow H_2O \tag{1.10}$$

At low electrode potential ORR follows the Associative pathway, which involves an absorption of O_2 molecular and the protonation of it into OOH*, which then afterwards be reduced into O*, OH* and water in sequence. At high electrode potential (> 0.8 V), a Dissociative pathway of ORR takes place due to low dissociative energy of O_2 (0.26 eV). In Dissociative pathway, O_2 molecular is directly split into O*, which then reacts with proton and electron to form OH* and finally water.[41] The difference between the above two pathways is when the O–O bond breaks, but it may be with the same importance that the first electron transfers are their rate determine step, respectively.

The ORR undergoes a four-electron process, which must involve the breaking of the O-O bond and the formation of the O-H bond. Studies have shown that the break of O-O bonds and the formation of O-H bonds are mutually competing and constrained. On one hand, the adsorption strength of O_2 on the platinum surface determines the ease of breaking the O-O bond. If the O* adsorption on Pt is too weak, it is not leading to the adsorption of O_2 and the break of O-O bonds. In addition, if the O* adsorption on Pt is too strong, the protonation of oxygen is inhibited, causing the active site of Pt to be covered, hindering the further adsorption of O_2 and the break of O-O bonds. Therefore, the adsorption strength of O* or OH* on Pt play a key role on the activity of ORR.

1.2.2 Pt facet effect for enhanced ORR

As a model catalyst, platinum single crystal electrodes with low index surfaces have been widely used for studying oxygen reduction activity and related mechanisms.[42]

Platinum single crystal catalysts are prepared from small beads, obtained by fusion and subsequent slow crystallization of high purity platinum wire.[43-44] After cooling, the resulting single crystal beads were oriented, cut and polished into platinum electrodes with specific surfaces. It has been shown that the ORR activity in $HClO_4$ electrolyte follows an order of Pt(111) ≈ Pt(110) >Pt(001) (Fig. 5a). [45-47] Theoretical studies have suggested a volcano type response for the ORR activity on Pt single crystals as a function of adsorbed oxygen containing species, with the (111) facet at the top of this curve. To extend this concept to PEMFC application using Pt nanoparticles, one research direction to enhanced ORR is to construct polyhedron particles, especially, octahedron limited by 111 surfaces. Juan M. Liu and co-workers also investigated high index surfaces with higher activity (Fig. 5b), due to orientation of their steps and terraces.[6] While, the stability of high index surface Pt is a big concern, and the mechanism of higher ORR activity on high index surfaces has not been well understood and need further investigation. The results on Pt single crystal films have been a large interest for understanding ORR mechanisms and have guided the development of more active nanoparticle catalysts and alloy catalyst.[48-51]

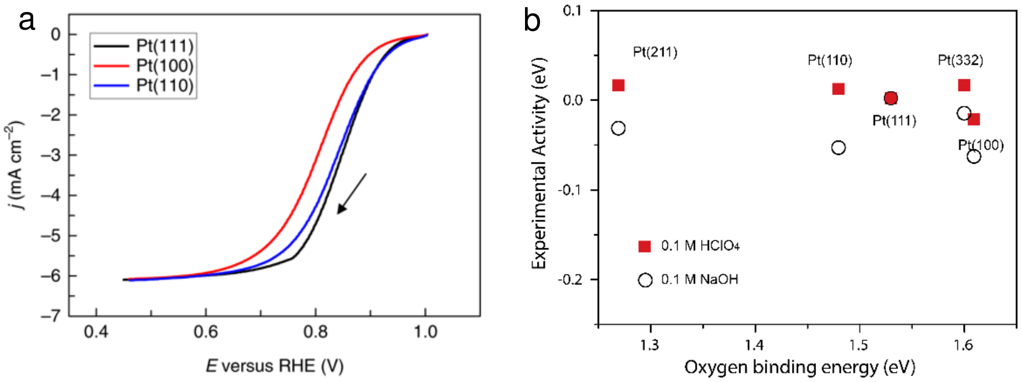

Fig. 1.5 a) Polarization curves of the ORR process at three low index Pt(hkl) surfaces.[45] b) Volcano plots for the oxygen reduction reaction on Pt single crystal (111), (110), (100), (332) and (211) surfaces.[47]

1.2.3 Size effect of Pt particles for ORR

For carbon black–supported Pt nanoparticles (Pt/C) catalysts, their specific area activity and mass activity have a certain relationship with the size of Pt particles, namely, the so-called size–effect. As shown in Fig. 1.6, Shao *et al.* reported that as long as the size of Pt particles increases from 1 nm to 5 nm, their specific area activity gradually increases, and the mass activity reaches an optimized size of around 2.2 nm.[52] According to theory, Pt

(111) surfaces have a minimum surface energy compared to other surfaces, which can also explain why experimental synthesized Pt nanoparticles have an almost sphere shape limited by 111 terraces, which is the most thermodynamically stable configuration. The ratio of the 111 terrace sites gradually increase along with the increase of Pt diameter, while the proportion of the kink/ledge atoms decreases. The catalytic activity of the kinks and steps is low due to much stronger oxygen binding energy. Meanwhile, when the particle size increases, the surface/bulk atomic ratio decreases, resulting in a decrease in the specific mass activity of Pt. Therefore, due to the competition of both effects, the specific mass activity of Pt particles is maximum at around 2.2 nm.

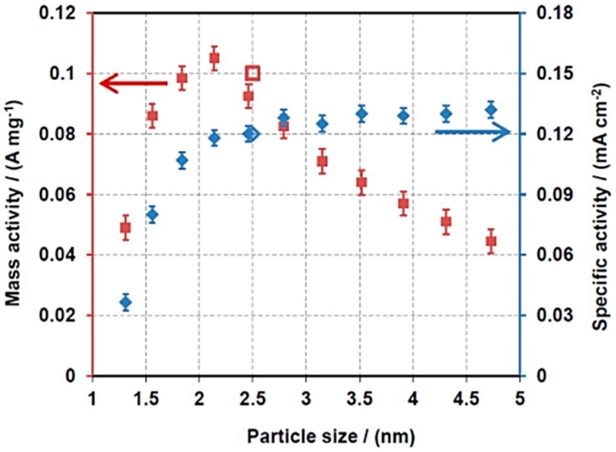

Fig. 1.6 The mass activity and specific area activity of Pt nanoparticles with various size from 1 nm to 5 nm.[6]

On the other hand, Watanabe *et al.* proposed that this size effect is not dependent on the size of the platinum particles, however, it should dependent on the distance (*d*) between adjacent Pt particles.[53] The authors used a colloidal method to prepared highly dispersed platinum catalyst with different sizes (1 ~ 5 nm), and loaded them onto high surface area carbon black supports with different Pt weight ratio, to adjust the spatial distribution of Pt on carbon. The size of Pt particles and *d*, were calculated by an indirect method based on surface area of Pt/C. The mass activity of Pt with different size and *d*, was reported to show linear relationship with Pt dispersion, while no obvious dependence of Pt size. Accordingly, they concluded that the specific activity of Pt increased with *d* from around 14 to 20 nm, but keeps constant for further increase *d* to ~28 nm, which means that the specific activity of Pt is fully achieved at 20 nm. Arenz and co–workers' reported that the difference in specific activity between carbon supported Pt particles with various size from 1 to 5 nm is very small, and the mass activity increases with increasing catalyst dispersion, in three different electrolytes.[38, 54-55] This may be due to different particle preparation methods and measurement protocols. For such studies, more defined catalysts, direct image and probe techniques and simulations would be very necessary for deeper understanding.

The size effect has also been investigated in low-Pt catalyst of Pt-based alloys. Gan *et al.* investigated ORR size effect of de-alloyed $PtNi_3$ nanoparticles with diameter between 3 and 10 nm. The $PtNi_3$ particles with initial particle size of 6 ~ 8 nm (5 ~ 6 nm after dealloying) showed the best durably and activity. They proposed that it was due to their highest retained Ni contents under the acidic ORR condition.[56] Wang et al. investigated monodisperse $CoPt_3$ nanoparticles with size between 3 and 9 nm.[57] They reported that the specific area activity of $CoPt_3$ increased along with the particle size from 3 to 9 nm, while the highest mass activity of 4.5 nm particles was measured.

1.2.4 Alloy effect of platinum for ORR

Another important breakthrough of this research area has been the discovery that alloying Pt with transition metals, such as Fe, Co, Ni and Cu, can enhance the activity of Pt atoms for ORR, meanwhile, it can save the Pt usage and thus reduce the catalyst cost.[58-59] Various reasons have been proposed to explain the superior Pt alloy catalysts – electron effect or geometric effect, as discussed below.

First, alloying with another metal can downshift the *d*-band center of Pt, which is called electronic effect.[60] This is shown in Fig. 1.7 for an example of Co, which exhibits the density of states *versus* energy for Pt and the evolution during its alloying process until Pt-Co. As can be noticed, there is a noticeable filling of the *d*–band of Pt from the higher level *d*–band states of the Co.[61-62] Density functional calculations reveal that downshifts of the *d*–band center of Pt atoms leads to a lower degree of adsorption of oxygenated species (OH* and O*) and increases the number of active sites accessible to oxygen, and therefore help to improve the ORR performance. Stamenkovic *et al.* have carried out systematic investigation of Pt_3M surfaces to analyze the relationship between surface electronic structure of *d*-band center and their ORR activity, as shown in Fig. 1.3b.[63] The *x*-axis is the Pt *d*–band center of Pt_3M surface, and the *y*-axis is their specific activity. It can be seen that Pt_3M exhibit 1 ~ 3 times high specific activity, as compared to bulk Pt.

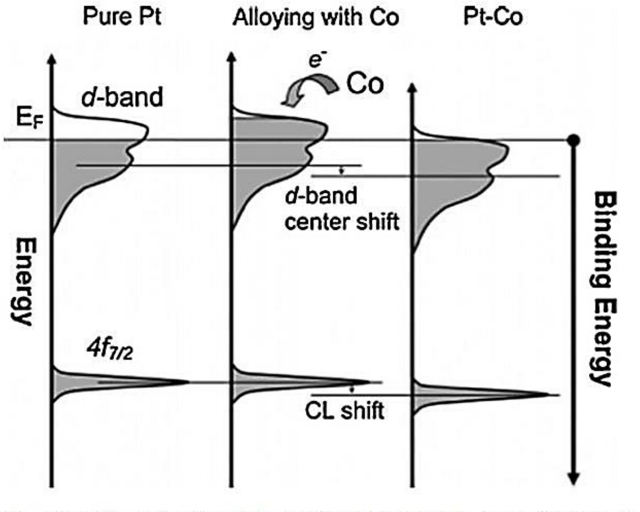

Fig. 1.7 Schematic explanation of the alloying effect on the electronic structures of Pt and CoPt.[61-62]

Simulation and experimental results revealed that the heterogeneous Pt catalysts with a strain between the substrate and the Pt layer could achieve higher catalytic activity for ORR catalysis.[38, 64-65] Peter Strasser *et al.* have reported an interesting diagram of CuPt system to study this strain/geometric effect.[66] By dealloying of CuPt nanoparticles, a few atomic Pt layers formed on mother CuPt particle, for which different lattice parameters can be achieved by adjusting the compositions of Cu and Pt. As shown in Fig. 1.8, the dash line is DFT calculation results between ORR rate and strain, which shows a volcano shape. The theoretical activities for the ORR are calculated as a function of the oxygen binding energy on strained Pt(111) surfaces. The volcano shape implies that compressive strain first enhances the overall ORR activity by reducing the oxygen binding energy, and thereby, lowers the activation barriers for proton and electron transfer processes. Beyond a critical strain, however, the oxygen binding becomes too weak and the catalytic activity is predicted to decrease because of an increased activation barrier for either oxygen dissociation or the formation of a peroxyl intermediate. The blue and red triangle spots are experimental results on strained Pt surface of CuPt particles and we can see that enhanced ORR catalysis achieved for all the CuPt compositions with compression strain. The authors believe that surface Pt lattice relaxes strain to bulk Pt and this is the reason why there is no volcano shape trends for experimental results.

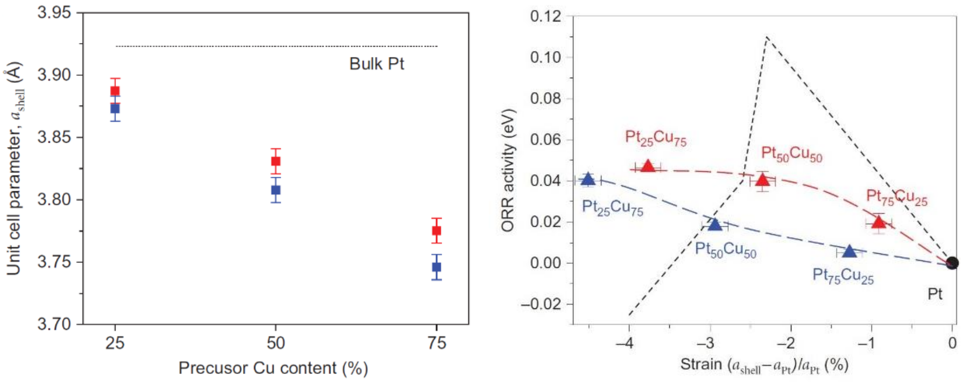

Fig. 1.8 Experimental and theoretical relationships between electrocatalytic ORR activity and lattice strain.[66]

Therefore, Pt-based alloy catalysts have attracted extensive attentions recently, due to its highly promising for PEMFC application, i.e., can solve insufficient activity and high cost issues surrounding now available Pt catalyst. With the advancements of synthetic chemistry, theory calculation and high resolution transmission electron microscopy techniques, various Pt–based nanostructures have been investigated in laboratory for ORR: Polyhedrons[67-71], core–shell structure[72-75], 1–D nanorods/nanowires[76-78], nanoframe structure[79], porous structure and single atom catalyst[80-81], as well as non-Pt catalyst.[82-94] Because of stability issues of the cathode in an acidic and electrochemical environment, non-Pt catalysts are not yet available for the fuel cell industry.

There has been improved ORR activity demonstrated by PtM alloys, which are normally prepared with a face–centered cubic (*fcc*) and solid solution structures. However, the durability of these catalysts is limited and insufficient to prevent M dissolution under corrosive ORR conditions, where the cathode operates at potentials far above the dissolution potentials of the M metals,and results in extensive M loss which compromises the benefits that the M brings to the PtM structures.[95] In the effort of searching for the more efficient form of Pt, a new strategy of controlling Pt alloy structure attracts much attention. For instance, ordered FePt with a chemically ordered face–centered tetragonal (*fct*) structure, namely, $L1_0$ or intermetallic structure can dramatically enhance the ORR stability and activity simultaneously. Besides, atomic positions of cubic MPt are randomly occupied by Pt and M atoms, leads to varying surface composition and randomly distributed active sites.[95] In contrast, ordered intermetallic phases have definite composition and structure, providing predictable control of the catalytic process.

1.2.5 Ordered FePt alloy for enhanced ORR

Initially synthesized FePt particles in solution are with *fcc* phase, which are coated with a layer of MgO and then converted to *fct*–FePt by thermal treatment at 750 °C. Fig. 1.9a shows an 8 nm *fct*–FePt/MgO particles after annealing, demonstrating monodispersed FePt particles and uniformly coating of MgO. This is low magnification TEM image, governed by mass-thickness contrast. FePt are heavier than MgO, resulting in darker contrast in the image.

Kim and co–workers have investigated this structure–dependent FePt nanoparticles catalysts, and reported that ordered structure *fct*–FePt nanoparticles are more active and stable than both disordered *fcc*–FePt and commercial Pt/C catalyst.[35, 96-98]

Next, they carried out acid treatment of *fct*–FePt/MgO particles in 0.5 M H_2SO_4 from 1 to 6 h, during this process MgO layers will be removed and Fe dissolved from FePt. The *fcc*-FePt/MgO particles acid treatment was also done to measure the acid resistance. Fig. 1.9b shows the composition evolution of the two FePt structures after acid treatment. The ordered FePt is found more robust in acid environment; disordered FePt nanoparticles suffered a heavy Fe loss of 36.5% in 1 h, while ordered FePt particles showed only a small Fe loss of 3.3%.

The FePt particles with two structure types and benchmark Pt/C catalyst were deposited on glassy carbon electrode to evaluate their ORR performance in 0.5 M H_2SO_4 electrolyte. Fig. 1.9c shows the polarization curves for the three samples. At the half–wave potential of 0.53 V, the ORR current densities generated by the *fct*–FePt and the *fcc*–FePt are 3.5 and 2 times the value measured from the commercial Pt/C.

The stability of these catalysts has been measured in O_2-saturated electrolyte at a scan rate of 50 mV/s for 1000 cycles. Fig. 1.9d shows the polarization curves after these cycles, the current densities at the half-wave potential were decreased by 20% for commercial Pt/C and 27% for *fcc*–FePt, however, only 14% for the *fct*–FePt catalysts. As result, it is clear that the activity and durability of the Pt-based alloy particles catalyst dependent on both their composition and structure.

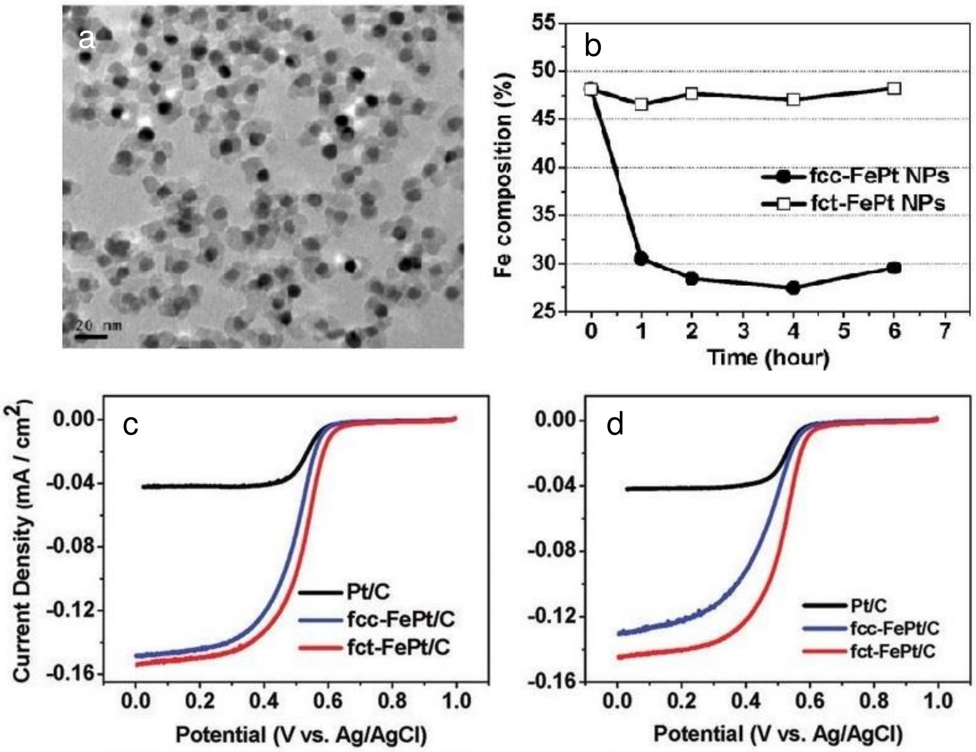

Fig. 1.9 a) TEM image of the 8 nm fct-FePt/MgO nanoparticles after thermal treatment. b) Time-dependent composition changes of *fcc* and *fct*-FePt nanoparticles after acid treatment in electrolyte. ORR polarization curves of commercial Pt/C, *fcc*-FePt/C, and *fct*-FePt/C c) before and d) after cycling measurement.[96]

Li and co-workers reported a controlled improve *fcc*−*fct* transition method to achieve fully ordered FePt nanoparticles and showed that the highest *fct*-ordering degree enhanced FePt ORR catalysis.[97] Fully ordered *fct*−FePt of 8.8 nm are prepared by annealing dumbbell shape FePt-Fe_3O_4 particles coated by MgO protect layer. Partially ordered FePt, *fcc*−FePt and benchmark Pt/C catalysts are used as reference to characterize this *fct*−structure effect on oxygen reduction.

Fig. 1.10a shows the ORR polarization curves of the above catalysts in 0.1 M $HClO_4$ electrolyte. The half–wave potential ($E_{1/2}$) increases and follows the order of Pt/C < *fcc*–FePt < partially ordered *fct*–FePt < fully ordered *fct*–FePt, with value of 0.883 V, 0.890 V, 0.927 and 0.958 V, respectively. This constitutes an evidence of activity improvement by fully ordered FePt on ORR, meanwhile the *fct*–structure effect.

Fig. 1.10b shows the durability measurement of fully ordered FePt nanoparticles after 20k cycles. The fully ordered *fct*−FePt particles also show remarkable durability in the ORR test conditions, demonstrating only slight performance loss after 10k and 20k cycles. They also show no particle morphology change and very small Fe/Pt composition variation from 50/50 to 47/53.

The authors also try to measure the performance of fully ordered FePt catalyst as an H_2−air PEMFC device cathode, as shown in Fig. 1.10c. The open circuit voltage for the commercial Pt/C is 0.959 V and around 30 mV lower than that of the *fct*−FePt catalyst (0.989 V) with the same Pt loading. The *fct*−FePt shows ~48% improved performance in the kinetically limited region than the Pt catalyst (0.378 A/cm^2 vs. 0.256 A/cm^2 at 0.8 V). The maximum power density measured from the *fct*−FePt-based cells was 0.70 W/cm^2, higher than that from the Pt-based one (0.63 W/cm^2).

Fig. 1.10d is a STEM image of *fct*−FePt after durability measurement, which confirms an ordering structure of *fct*-FePt with alternating intensity between Fe and Pt, due to Z-contrast mechanism of HAADF–STEM. These preliminary data indicate that the fully ordered *fct*−FePt is a catalyst with much desired activity and durability for practical applications in PEMFC.

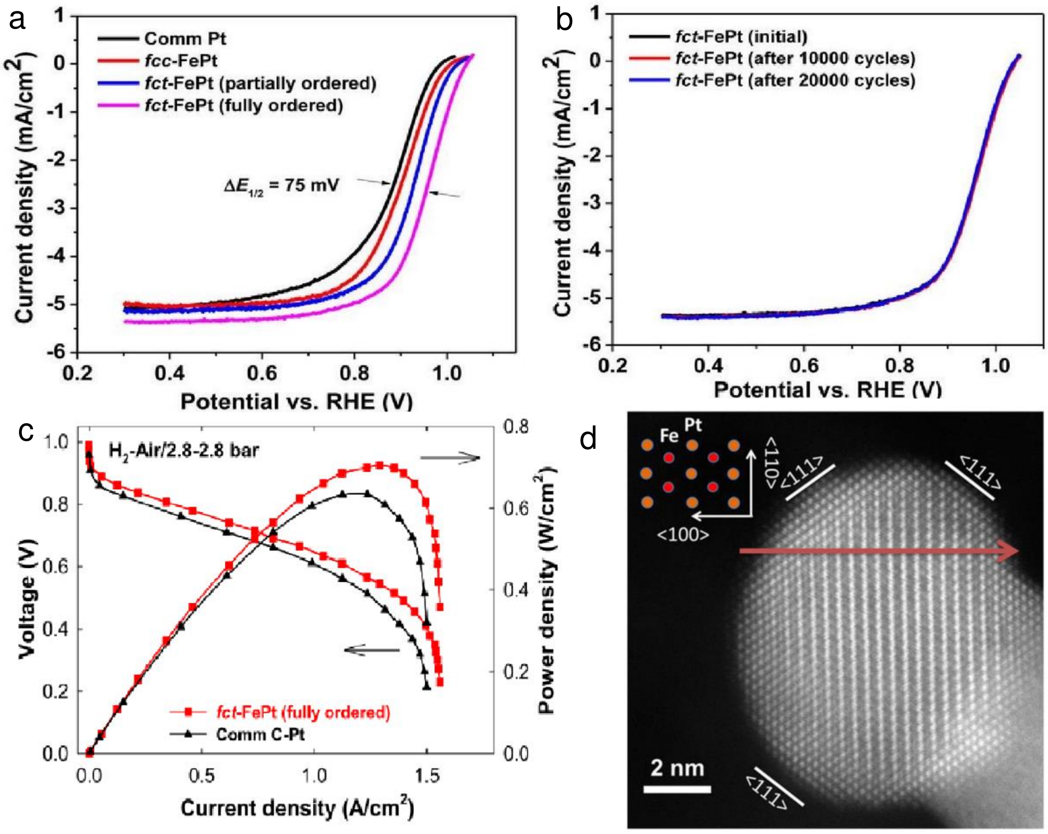

Fig. 1.10 a) ORR polarization curves of commercial Pt/C, phase transformed FePt nanoparticles. b) Durability measurement of fully ordered FePt nanoparticles. c) Fuel cell device performance of fully ordered FePt and Pt/C. d) High resolution STEM image of a fully ordered FePt nanoparticle.[97]

Further modification of fully ordered FePt nanoparticles surface with a size of 8.0 nm was carried out by acid washing and post thermal treatments.[98] Experimentally, *fct*−FePt nanoparticles were dispersed and stirred in 0.1 M $HClO_4$ acid solution at 60 °C for 12 h, followed by annealing at 400 °C for 2 h, results in *fct*–FePt@Pt structure with two atomic layers Pt surface. The presence of *fct*–FePt in the alloy core induces compression strain of Pt shell with a suitable thickness, thus can improve their ORR catalysis due to strain effect and alloy effect. A concept catalyst is prepared and extensive studies have carried out on their catalysis performance, especially in PEMFC device setup at 60 °C.

Fig. 1.11a~c demonstrate its structure by high resolution STEM–HAADF and STEM–EDX mapping image (blue colour is Fe, red colour is Pt), which demonstrate the core/shell structure of $L1_0$–FePt/Pt catalyst.

ORR polarization curve and accelerated durability test were conducted to demonstrate the catalyst activity and stability, as shown in Fig. 1.11d. The mass activity of the $L1_0$–

FePt/Pt drops from 0.70 to 0.68 A/mg$_{Pt}$ at 0.9 V, while commercial Pt/C shows a drop of mass activity from 0.13 to 0.005 A/mg$_{Pt}$.

Fig. 1.11e shows the fuel cell device performance measurement, compromised with $L1_0$–FePt/Pt and Pt with the same size, respectively. It shows initial and durability performance of $L1_0$–FePt/Pt superior to Pt in the completely potential range, demonstrating that it is the the excellent activity and durability of intermetallic $L1_0$-FePt structure in practical fuel cell setup.

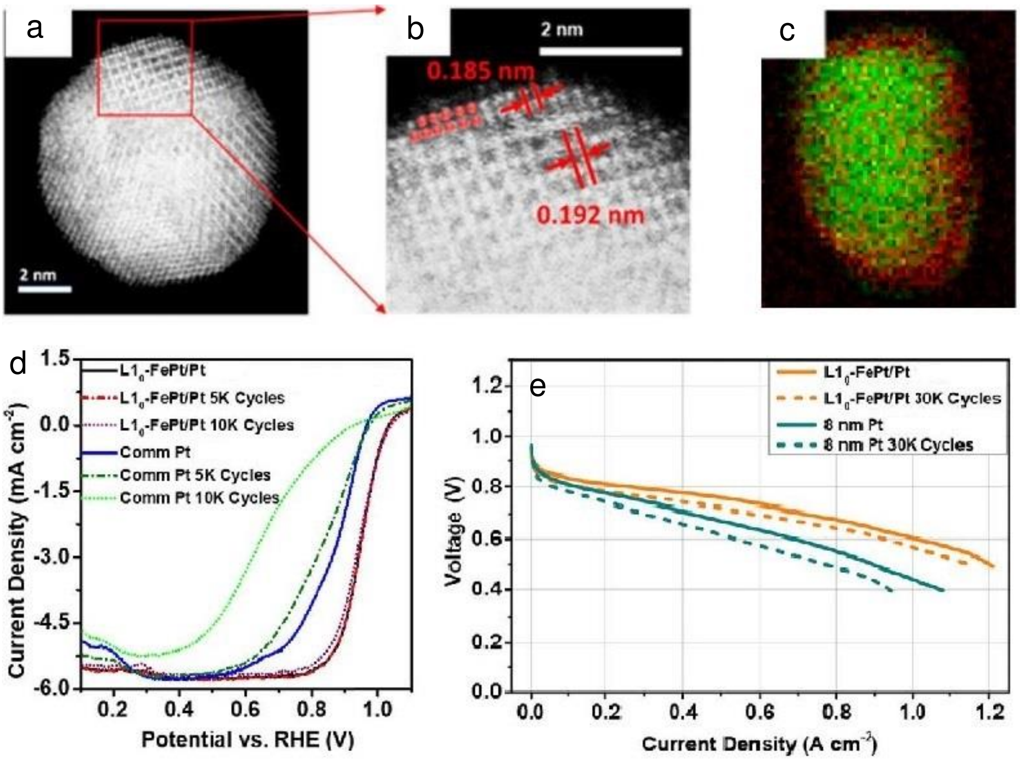

Fig. 1.11 a) HAADF−STEM image of a representative $L1_0$−FePt/Pt NP with ~2 atomic layers of Pt shell and b) its enlarged image. c) 2D EELS elemental mapping image of a $L1_0$−FePt/Pt particle, where Fe is colored green and Pt is colored red. d) ORR polarization curves of the $L1_0$−FePt/Pt and commercial Pt tested before and after the durability test. e) Fuel cell polarization curves recorded from the fuel cell device assembled with the $L1_0$−FePt/Pt and 8 nm Pt catalysts.[98]

1.3 FePt basics

According to the equilibrium Fe−Pt phase diagram of Fig. 1.12, the FePt binary alloy has three ordered phases with different atom ratios, i.e., FePt ($L1_0$, *fct*) and $FePt_3$/Fe_3Pt ($L1_2$, *fcc*).[99-100] At high temperature, FePt crystallizes in the *fcc* structure and is disordered.

The magnetic properties of Fe−Pt alloys are closely related to chemical ordering and stoichiometry. Ordered Fe_3Pt and FePt are ferromagnetic. $FePt_3$ is ferromagnetic in the disordered high temperature phase, while it is antiferromagnetic in the ordered $L1_2$ structure. There is a structural transformation from disordered *fcc*−FePt to $L1_0$−FePt, when the temperature decreases while keeping the same stoichiometric ratio.

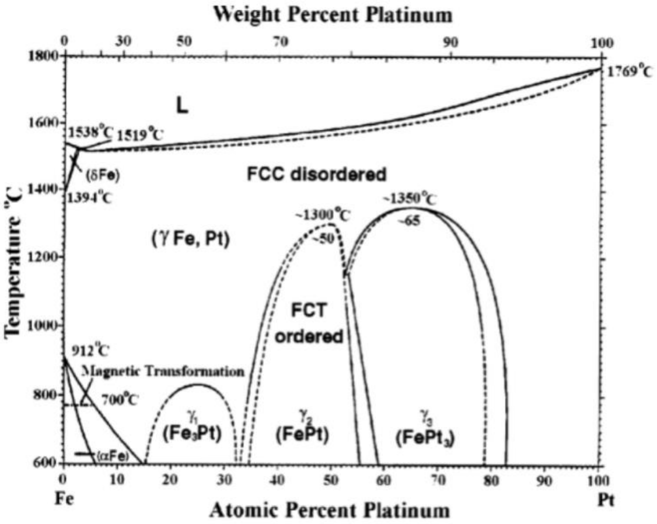

Fig. 1.12 Phase diagram of FePt system.[99]

The atom models of FePt with different compositions/structures and according powder X-ray diffraction patterns can be seen in Fig. 1.13. For *fcc*–FePt crystal, Fe and Pt atoms randomly occupy positions of face-centered cubic unit cell, having lattice parameter *a* of 3.84 Å. Its X-ray diffraction diagram shows characteristic cubic structure with (111), (200) and (220) peaks. For *fct*−FePt, Fe and Pt atoms alternatively stack along [001] direction of a face-centered tetragonal structure, forming an ordered intermetallic. The transition from the *fcc*−FePt to the *fct*−FePt structure can be achieved by thermal treatment, referred to as ordering process. This ordering process results in a FePt unit cell contraction in the *c*−axis direction and a decrease in the lattice constant *c* (3.71 Å), meanwhile a stretch of FePt unit cell along *a*/*b* directions and increase of lattice constant *a* and *b* (3.85 Å). Compared with the *fcc*−FePt, the (111) plane spacing of the $L1_0$−FePt structure also decreases, and corresponding (111) peak shifts to a high angle of XRD curve. Moreover, the characteristic (001) and (110) peaks of ordered FePt appear in the XRD curve, and the 002 peaks splitting, which is usually used to monitor the chemical ordering of FePt nanocrystal.

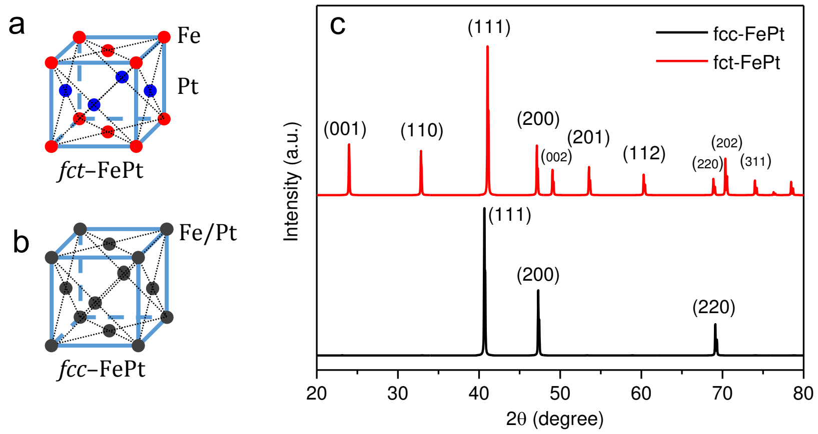

Fig. 1.13 Atomic models of FePt with different compositions, a) *fct*−FePt and b) *fcc*−FePt, and c) the powder X−ray diffraction patterns showing the new peaks for that in the *fct* diagram (red).

Theory calculation has been used to calculate the surface energy of $L1_0$–FePt surface energy, as shown in Table 1.3.[101] When a FePt crystal is cleaved on any one of the 100, 011, and 111 planes, two exposed surfaces consist of both Fe and Pt atoms in the same composition. The cleavage energies Gc for those planes, taking into account relaxation, are 4.23, 3.95, and 3.49 J/m^2, respectively. Correspondingly, the specific surface energies, $\gamma_s = Gc/2$, are 2.12, 1.98, and 1.74 J/m^2, respectively. Two equilibrium shapes of FePt crystals, in a two-dimensional plot perpendicular to the 011 viewing direction, were constructed based on the surface energy anisotropy, as shown in Fig 1.14.

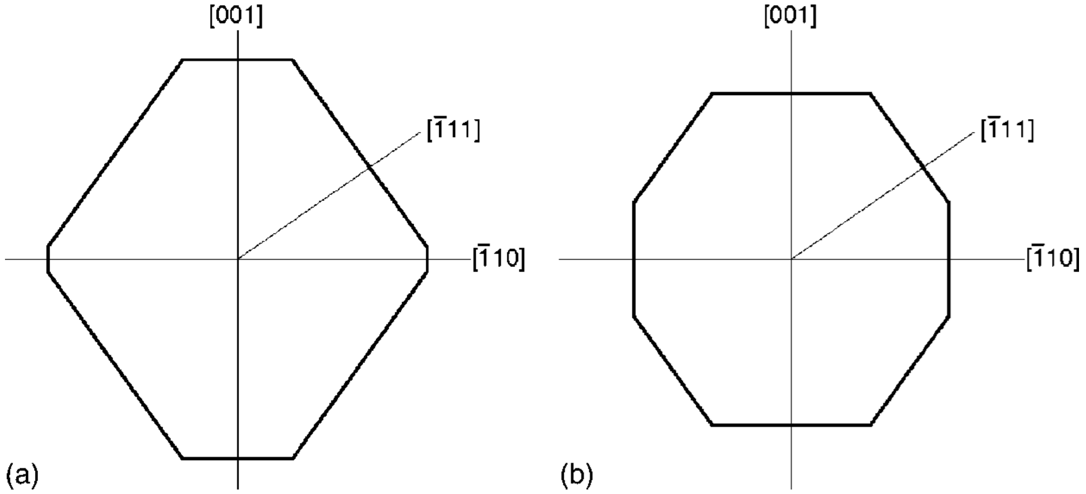

Fig. 1.14 Two equilibrium crystal shapes of an $L1_0$–FePt particle, projection along the [110] direction.[101]

Table 1.3 Cleavage energy G_c and surface energy γ_s of L1_0–FePt[101]

(*hkl*)	Unrelaxed	Relaxed	
	G_c	G_c	γ_s
100	4.32	4.23	2.12
001	4.42	4.37	–
011	4.22	3.95	1.98
110	4.39	4.08	–
111	3.54	3.49	1.74

Generally, the directly synthesized FePt alloys usually have a disordered *fcc* structure, and exhibit low durability for ORR in acidic solution.[102] In contrast, ordered intermetallic phases have definite composition and structure, providing predictable control of the catalytic processes. Furthermore, the ordered structure enhances the chemical and structural stability of the catalytic particles.[22, 95, 103-106] Sun and co-workers have performed model investigation on this structure–dependent FePt nanoparticles catalysis, and demonstrated that L1_0 structure FePt nanoparticles are more active and stable than both the A1–FePt and commercial Pt/C catalyst.[96] Goodenough and co-workers demonstrate that ordered Fe_3Pt/C catalysts exhibit much higher activity and durability than disordered Fe_3Pt/C and Pt/C.[95] Similar results can also be found by CoPt system, Abruña et al. demonstrated that intermetallic Pt_3Co nanoparticles are more active and durable than the disordered Pt_3Co and Pt/C.[107] In addition, the authors believe that the high activity and durability can be ascribed to a thin Pt–rich shell forming on Pt_3Co surface, and the stable intermetallic Pt/Co arrangement in the core. Our recent studies indicate that the intermetallic FePtCu nanoparticles can be synthesized by one–pot method and show superior ORR performance than commercial Pt/C. While, the core–shell structure is quite interesting but sensitive to the alloy composition.[108]

The magnetic properties can be also used to characterize the FePt ordering degree.[109] As can be seen in Fig. 1.15, the coercivity of FePt nanoparticles synthesized at different temperatures, demonstrating positive or linear correlation between the coercivity and FePt chemical ordering degree.

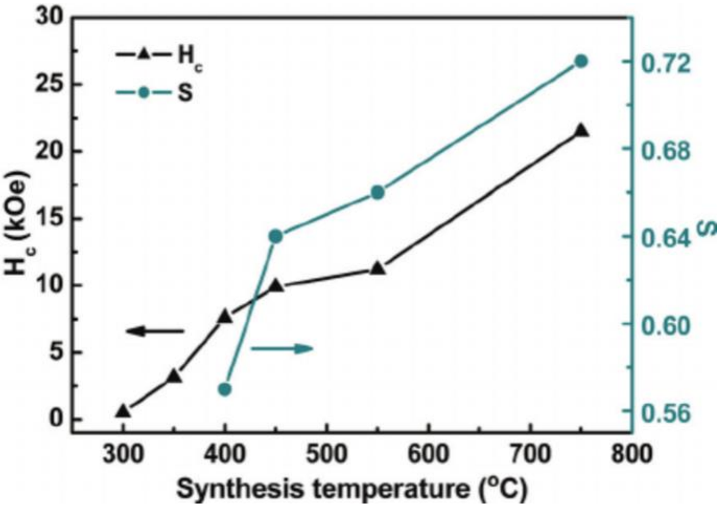

Fig. 1.15 The coercivity *Hc* and chemical ordering degree *S* of FePt nanoparticles.[109]

Chapter 2

Experimental Methodology

This chapter presents the techniques that have been used to carry out this work, starting by how our materials have been fabricated and then characterized. The characterization has been an iteration between catalytic activity measurements, structural investigation by X–ray diffraction and transmission electron microscopy with the synthesis process in order to try to optimize the properties of the materials toward high performance fuel cells.

2.1 One–pot synthesis of ordered FePtAg/FePtCu

2.1.1 Nucleation and growth mechanisms of nanocrystal in solution

Conventionally, wet–chemistry methods are prevalent for their low cost, high yield, high versatility in surface chemistry, shape and size controllability, as compared with physical synthesis methods. The nucleation and growth of nanocrystals from liquid–phase have been the subject of investigations for almost 70 years and is fairly well understood.[1] According to LaMer theory, nanocrystal formation splits into three distinct stages: a pre-nucleation of monomers, a seed nucleation stage, followed by the seed growth phase, as illustrated in Fig. 2.1.[110] As the reaction proceeds with reaction time, the concentration of free monomers increases in solution. Then, the seed nucleation corresponds to the burst formation of nuclei from a supersaturated solution of monomers. The initial nucleation event reduces the local monomer concentration in the solution below super-saturation, prohibiting more nuclei from forming. After that, the nuclei undergo diffusional growth as monomers from the surrounding solution which feed them. Such monomer attachment/diffusional growth is also governed by crystal growth models, e.g. Ostwald ripening, oriented attachment or coalescence. Ostwald ripening theory describes the relationships between size and solubility of nanoparticles. The smaller crystal is susceptible to dissolution due to high solubility, which in turn, promotes the larger particle growth in size. For coalescence effect, it is random for the attachment, whereas for the orientated attachment, it is specific of crystalline alignment for attachment to occur.[111]

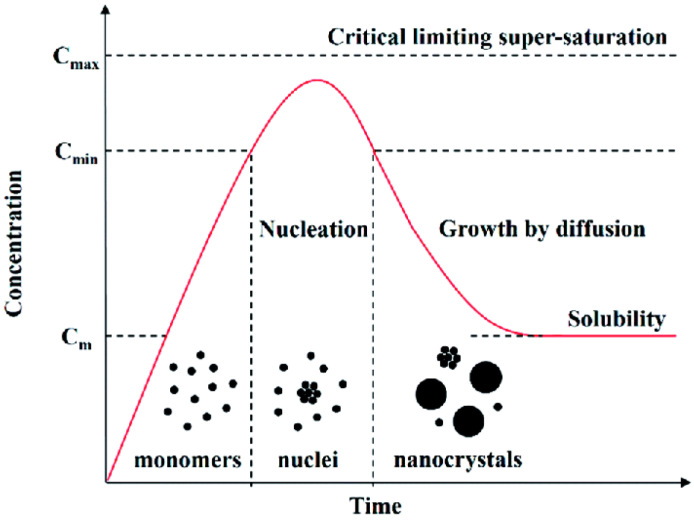

Fig. 2.1 LaMer theory of particle growth.[110]

2.1.2 Seed mediated method

Seed-mediated growth strategy is characterized by separating the crystal nucleation and the crystal growth steps, making the synthesis controllable. There are two main procedures involved: the synthesis of seed nanocrystals and the subsequent crystal growth on its surface. A general illustration of seed-mediated strategy is shown in Fig. 2.2.[112] The ageing and purification processes of seeds sometimes may be needed. The well-defined seeds are dispersed into a supersaturated solution in order to perform crystal growth on the preformed seeds/templates. The colloidal seeds can be used in the original reaction medium or collected and then dispersed into a different medium.[112] In both cases, the growth under carefully controlled conditions can transform the seeds into nanocrystals with a well–controlled composition, size, shape, and structure.

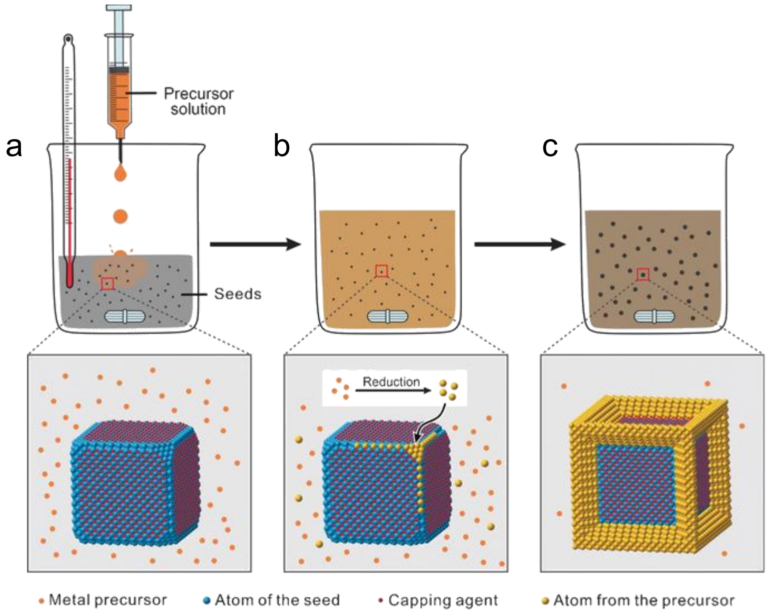

Fig. 2.2 Illustration of a general strategy to synthesize colloidal metal nanocrystals – seed-mediated method.[112] a) Injection of the precursors into a vessel containing seeds and other reactants, such as solvent and reductants. b) The metal precursor cations are decomposed or reduced into zero-valent atoms, which grow on the surface of seeds. c) Further growth results in formation of well-defined nanocrystals.

Core–shell FePtM/FePt (M = Pd, Au) nanowires have been reported by seed-mediated synthesis method.[113] FePtM nanowires have an average diameter about 2.5 nm and a typical length of 20−100 nm, which are used as seeds to grow 0.3~1.3 nm FePt shell on the FePtM core. The composition of FePtM core and the thickness of FePt shell were found critical for oxygen reduction reaction catalysis, FePtPd/FePt with 0.8 nm shell exhibited the highest activity. This result proves the importance of performance optimized by controllable strategy of seed-mediated.

Core–shell Au@FePt nanoparticles have been synthesized by seed-mediated synthesis method.[114] The sizes Au are controlled to have 4, 7, and 9 nm and the FePt shell was controlled to have 0.5, 1, and 2 nm thickness. It has been found that the catalytic activity of methanol oxidation is dependent on the FePt thicknesses, but not much on the Au core sizes. The 1 nm FePt shell has been found to be the optimal thickness for catalysis, offering not only high activity, but also enhanced stability.

FePt–Au hybrid nanoparticles have been reported by seed-mediated synthesis. Three kinds of FePt with concave–cube shape (11 nm), cube–shape (8 nm) and truncated–cube (5 nm) shape were synthesized and serving as seeds. Au particles preferred to grow on the octahedral apexes of FePt seeds, forming FePt–Au hybrid nanoparticles. The Au particle attachments on FePt octahedral apex depends on the seeds morphology, which are eight for concave–cube FePt, four for cube–shape FePt and two for truncated–cube FePt.

However, seed mediated method is limited for producing nanomaterials with large scale, due to low mass yield of less than 2 mg per batch.[115] Furthermore, precise attentions are needed: the preparation and quality of the seeds, the parameters of growth such as precursor concentrations, reaction temperature and the purity of reactants and reaction vessels. It is also limited to synthesize nanocrystals smaller than the seeds. A strategy to overcome these drawbacks is to combine crystal nuclei and growth into a one-pot process.

2.1.3 One–pot method

In synthetic organic chemistry, one–pot synthesis is a method whereby reactants are subjected to successive multistep chemical reactions in just one reactor, which has been used for a long time.[116] One–pot method has also been widely developed for metal nanoparticle synthesis, which offers a number of advantages, such as reduction of reaction steps/time, operational simplicity, energy efficiency, minimization of the purification process, therefore fulfilling some of the objective of green and sustainability chemistry.[115] In theory, crystal nucleation and growth theory governs the synthesis processes on one–pot method, although most nanostructures synthesized are obtained by trial and error studies.[117] A illustration of one–pot synthesis of metal nanoparticles is shown in Fig. 2.3.

Fig. 2.3 Illustration of one–pot method for synthesis of metal nanoparticles. The reactants containing metal precursors, stabilized agents, reductants and solvent are all put into a vessel. After successive multistep chemical reactions of decompositions or reductions, metal nanocrystals are obtained.[118]

FePt nanostructures with various shapes, sizes, compositions have been synthesized by one–pot method. Sun and co–workers synthesized monodispersed FePt nanospheres by two chemistry methods.[119-121] One is a reduction of $Pt(acac)_2$ and decomposition of $Fe(CO)_5$ with surfactants of oleyl amine and oleic acid. The FePt composition is tunable by changing the molar ratio of metal precursors, and their size (3 ~ 10 nm) is adjustable by *in situ* enlarging 3 nm FePt seeds with more reactants or controlling the surfactant to metal precursor ratio. The Fe complex precursor was decomposed and the Pt salt reducted in similar reaction conditions, which resulted in the simultaneous nucleation and growth of FePt into spherical shaped nanoparticles. The other is a reduction of $FeCl_2$ and $Pt(acac)_2$ precursors with dual reductants, this lead to monodisperse 4 nm FePt nanoparticles.

Moreover, FePt nanowires and nanocubes can be synthesized by modifying the synthesis conditions, including the solvent, precursor, surfactants, reductants and heating condition. For instance, FePt nanoparticles with three different morphologies of dendrite, sphere and cube shapes have been reported.[122] One–dimentional FePt nanostructures of nanowires have been reported through decomposition of metal pentacarbonyl and reduction of platinum acetylacetonate in sodium oleate solution of 1–octadecene and oleylamine.[123] The FePt nanowires diameters is 2~3 nm. The length of the nanowires is tunable from 200 nm down to 20 nm by controlling the volume ratio of oleylamine and octadecene.

One–pot synthesis thus shows versatile to synthesize morphology, size and composition controllable FePt nanocrystals, with least number of processing steps possible, shorten time and low cost.

2.1.4 Ordered FePt preparation in solution

The as–synthesized FePt nanostructures are normally *fcc* phase, therefore, thermal annealing at optimized temperature of around 550 °C is needed to promote the FePt transform from *fcc* to *fct*.[119] However, annealing is usually performed on dried nanopowders, which often results in particle aggregation, and may lead to the degradation of the particle uniformity. High-temperature annealing also destroys the organic ligands surrounding the nanoparticles, which takes away the advantage of the specific chemical functionality of the end groups, useful for chemical recognition and self-assembly into monolayers.

To address this issue, coating methods with inorganic materials, such as MgO, Fe_3O_4, SiO_2, MnO have been applied and resulted in preventing the FePt agglomeration during thermal treatment.[96, 124] Subsequently the coated shell can be removed in a subsequent process, but during this conversion from *fcc* to *fct* is often incomplete and additional chemical processes are induced. For instance, by coating the *fcc*–FePt nanoparticles with a layer of MgO, the *fcc*–FePt/MgO could be converted to the *fct*–FePt/MgO without FePt aggregation at 750 °C for 6 h under 95% Ar + 5% H_2.[96] The MgO coating was removed by a dilute acid wash, and ferromagnetic *fct*–FePt nanoparticles could be stabilized by oleic acid and dispersed in hexane. Fully ordered face–centered tetragonal (fct) FePt nanoparticles are synthesized by thermal annealing of the MgO–coated dumbbell–like FePt–Fe_3O_4 nanoparticles followed by acid washing to remove MgO.[97] Later on, a salt matrix method was developed. However, this method still requires the synthesis of *fcc*-FePt nanoparticles in a solution environment first, which has a limited yield and the yield will further reduce after removal of the matrix.

Another method is introducing a third metal additive to promote the *fcc*–FePt ordering during annealing process, by reducing the annealing temperature. Silver is commonly regarded with similar effects with Au on FePt ordering and grains growth. Kang *et al.* prepared 3.5 nm FePtAg nanoparticles, and they found that Ag additive promoted the *fcc* to tetragonal phase transition, thereby reducing the temperature required for this transition by some 100 to 150 °C compared with pure FePt nanoparticles.[128] After anealing at 400 °C for 30 min, the coercivity of the films containing FePtAg nanoparticles was more than 3.4 kOe, while the films containing FePt nanoparticles were superparamagnetic. Later on, an optimized doping content of 15% Ag was found to promote FePt ordering and 10 kOe FePtAg was achieved at 500 °C thermal treatment.[129] While, without Ag, FePt nanoparticles showed only 2 kOe coercivity. Wang *et al.* prepared ordered FePtAg nanoparticles using a one–step method without post–thermal annealing, while with reaction temperature of 340 °C and extended reaction time of 3 h.[130] A record breaking coercivity of 7.6 kOe FePtAg nanoparticles were obtained at high Ag doping content of 29%.

Tzitzios *et al*. prepared FePtAu and FePtAg nanoparticles with different compositions via a modification of the polyol process.[131-133] The 13% doping exhibited the greater transformation, i.e. at lower temperature. The addition of Au and Ag to the FePt alloy lowers the ordering temperature to 350 and 375 °C, respectively. Annealing at various temperatures showed the transformation toward the fct to starts abruptly. They proposed that a third metal of Au or Ag most probably plays the role as a catalyst in the ordering processes.

Yang *et al.* synthesized doped $L1_0$–FePt by sol–gel method.[100] The authors reported that Au doping promoted the $L1_0$ ordering, thereby reducing the temperature required for this transition by more than 100 °C, as compared with pure FePt nanoparticles with no additives.[100] While, Cu doping played a significant role in changing the structure and magnetism of $L1_0$–FePt, and with the increase of Cu content, the coercivity increased but the magnetization decreased.[134]

An important discovery in this area is that these additive atoms can *in-situ* promote FePt ordering in some high boiling temperature solvents, this is also called direct/one–pot synthesis of ordered FePt. Harrell *et al.* firstly reported one–pot synthesis of ordered FePtAu nanoparticles with high coercivity in high boiling temperature (300 ~ 360 °C) solvent of hexadecylamine.[125] Ordered FePtAu exhibited coercivity ranged from a few hundred oersteds to a few thousand oersteds, depending on the concentration of gold additive and the synthesis temperature. The size of the FePtAu nanoparticles is around 8 nm. Kinge *et al.* reported the one–pot synthesis preparation of *fct*–FePtAu nanoparticles with the highest coercivity of 4.8 kOe with 5.8 ± 2.3 nm diameter, with reaction time extension to 3 h.[126] FePtAu nanoparticles grow bigger in size and become uneven along with increase of the synthesis temperature. Yu *et al.* reported the synthesis of *fct*–FePtAu nanoparticles with the highest coercivity of 12.15 kOe, which was achieved through 32% Au doping and particle size is 11.0 ± 1.0 nm.[127] When Au doping content decreased to 14%, the measured coercivity was 4.5 kOe with particle size of 6.5 ± 0.5 nm.

Direct one–pot method is thus an efficient strategy, with minimum preparation processes, for *fct*–FePt nanoparticle synthesis, as compared to MgO or salt coating and additive induced methods, which both need post annealing. Furthermore, one–pot method is highly promising for large–scale production of ordered FePt as fuel cell catalysts. However, the crystal nucleation and crystal growth of FePt nanostructures synthesized by one–pot methods are with limited investigation. Classical and new nucleation and growth behaviors have been found in one–pot synthesis, although the experimental methodologies were mainly based on trial and error strategy. Based on above analysis, we carried out one–pot synthesis of ordered FePt nanoparticles with Ag/Cu additives, and investigated their ordering mechanisms for more efficient catalysis.

FePtM (M= Ag or Cu) nanoparticles were synthesized with one–pot method in different solvents, i.e., octadecylamine, hexadecylamine and trioctylamine. A solvent needs pre-processes such as being melted into liquid state at temperature below 100 degree if necessary, and being degassed with high purity nitrogen bubbling to remove the dissolved air in the solvents. Then, Fe, Pt and M sources were resolved into the solvent in a 100 mL three-necked round-bottom flask under mechanical stirring. After the metal precursors dissolved in the solvent, a clarified liquid can be obtained. Then, the surfactants and reduction reaction are added into the solution, meanwhile, keeping nitrogen bubbling, mechanical stirring and low temperature around 100 degree. 1, 2–hexadecanediol is used as reduction reactant, oleic acid and oleylamine are used as surfactants. Then, the solution was gradually heated to slightly boiling state (320 ~ 345 °C) at a rate of 10 °C/min, following by refluxing for 20 min to 3 h.

After refluxing, the as-prepared black solution is cooled down to room temperature; where nitrogen introduction and mechanical stirring are stopped. The FePtM nanoparticles are washed by adding 50 mL ethanol in the solution and the separation is carried out through centrifugation at 5000 rpm or by a magnet. The yellow-brownish supernatant is then discarded. Further purification of the product was performed by dispersing the product into hexane, precipitating with ethanol and then centrifuging for three more times. Finally, the purified nanoparticles were dispersed in 10 mL hexane for characterizations.

For FePtAg nanoparticle synthesis, $Pt(acac)_2$, $Fe(acac)_3$ and AgAc are used as precursors. FePtAg has been synthesized in three high boiling temperature solvents of octadecylamine, hexadecylamine and trioctylamine solvents, and the solvent effect on FePtAg structure has been studied.

For FePtCu nanoparticle synthesis, $Pt(acac)_2$, $FeCl_2/Fe(acac)_3$ and $Cu(acac)_2$ are used as metal sources, hexadecylamine is used as solvent. The chloride anions play a critical role in the crystalline growth of FePtCu. The composition of FePtCu was firstly designed with same Fe/Pt ratio and different Cu concentration, $(FePt)_{100-x}Cu_x$ (x=10, 20, 30 and 40). The reaction precursors were resolved into the solvent in a 100 mL three-necked round-bottom flask with mechanical stirring, including 0.40~0.35 mmol $Pt(acac)_2$, 0.40~0.35 mmol $FeCl_2$, 1.5 mmol 1,2-hexadecanediol, 0.10~0.40 mmol silver acetate. $Fe_xPt_{80-x}Cu_{20}$ (x=30, 35, 45 and 50) can be synthesized with the same procedures.

For investigating the FePtCu nucleation and growth mechanisms and further studying the dynamics of FePtCu ordering, we carried out *quasi-in-situ* characterization of one–pot synthesized FePtCu, by acquiring the intermediates of 20 min, 40 min, 1 h and 2 h reaction time. $FeCl_2$, $Pt(acac)_2$ and $Cu(acac)_2$ were dissolved into 20 ml hexadecylamine at 80 °C under magnetic stirring, and constant nitrogen bubbling in advance for 20 min, forming light blue colour solution. After that, oleylamine/oleic acid surfactants and 1, 2–hexadecanediol reductant were added into the solution and then the reaction system temperature was gradually raised to 320 °C, during which the solution colour changes into dark blue and black colour afterwards. FePtCu nanoparticle intermediates were acquired after refluxing at 320 °C for 20 min, 40 min, 1h and 2h.

2.2 Half-cell evaluation of ORR catalyst

Rotating disk electrode with a porous catalyst film has been the most widely used technique to characterize the supported catalysts in liquid electrolytes, since it was proposed by Stonehart and Ross in 1976.[135-137] The general principle of fabricating a RDE with a fuel cell catalyst can be explained as follow: catalyst powders are firstly loaded on porous carbon black, and then dispersed into alcohol or its mixture with water to form colloidal ink. Then the ink is drop coated on glassy carbon electrode, forming a uniform film after drying. During this process, the quality of the ink, the solvent composition and drying process are vital for the quality of the film. To mitigate the mass transfer effect during ORR activity measurements, glassy carbon electrode is rotated to increase the mass transfer rate of oxygen at the electrode surface. The intrinsic activity of the catalysts can be derived according to the Koutecky-Levich equation:[138-139]

$$\frac{1}{j}=\frac{1}{j_k}+\frac{1}{j_l} \tag{2.1}$$

$$j_l=0.62nFcD^{2/3}\omega^{1/2}\nu^{-1/6} \tag{2.2}$$

$$j_l=0.62nFcD^{2/3}\omega^{1/2}\nu^{-1/6}=B\omega^{1/2} \tag{2.3}$$

$$B=0.62nFcD^{2/3}\nu^{-1/6} \tag{2.4}$$

$$\frac{1}{j}=\frac{1}{j_k}+\frac{1}{j_l}=\frac{1}{j_k}+\frac{1}{B}\omega^{-1/2} \tag{2.5}$$

where, j is the the measured disk electrode current density (A/cm^2), j_k is the kinetic current density (A/cm^2), j_l is the diffusion limiting current density (A/cm^2), n is overall number of electrons transferred, F is Faraday constant, F = 96485 C/mol, c is O_2 concentration, $c = 1.26\times10^{-6}$ mol/cm^3, D is diffusion efficiency of O_2, D = 1.9×10^{-5} cm^2/s, ν is viscosity of the electrolyte, $\nu = 1.009\times10^{-2}$ cm^2/s. The large current densities common in fuel cell operation cannot be reached because oxygen solubility in electrolyte is low, and limiting currents are small, ~6 mA/cm^{-2} at a rotation rate of 1600 r/m. The technique therefore aims at determining the kinetic current at 0.9 V, calculated from the measured current after applying corrections for ohmic potential drop, capacitive background currents, and mass transport (Koutecky-Levich equation, eqn.2.2). This current is normalized to the total true electrochemical catalyst surface area (ECSA), determined specific area activity, or specific mass activity to the total Pt mass on the electrode.

Fig. 2.4a is a typical polarization curve obtained by Linear Sweep Voltammetry (LSV) technique of electrochemistry.[140-142] The scan rate is between 5 and 20 mV/s, with a potential window between 0 and 1.1 V. Before electrochemical measurement, the electrolyte must be oxygen saturated, which is achieved by bubbling high-purity O_2 in for at least 40 minutes in advance and then keep oxygen bubbling during the whole measurement processes. It is recommended to bubble oxygen for 10 min before LSV measurement, due to it needs to be quantitatively analyzed.

Cyclic voltammetry (CV) is the most used electrochemical technique in electrochemistry and can be used to characterize the reaction behavior at different potentials.[143-144] Fig. 2.4b shows the CV curves of Pt and Pt alloy in 0.5 M H_2SO_4 electrolyte with a potential window from 0 to 1.4 V at scan rate of 50 mV/s. Between 0 and 0.3 V, electrochemical absorption and desorption of hydrogen happen at reductive scan and oxidize, respectively.[143] Between 0.3 V and 0.5 V, it is electric double layer mainly originate from the carbon black and no redox reactions happens in this region. Above 0.5 V, electrochemical absorption and desorption of oxygen-containing group (OH^- at lower potential region, O_2* at higher potential region) happen, resulting in redox peaks. For CV measurement of ORR catalyst, catalyst first cycling in N_2–saturated electrolyte between 0 and 1.2 V until the CV curve becomes stable, at a scan rate of 100 mV/s to activate the electrode. Then record the CV curve at 50 mV/s scan rate, with potential window of 0 ~ 1.2 V.

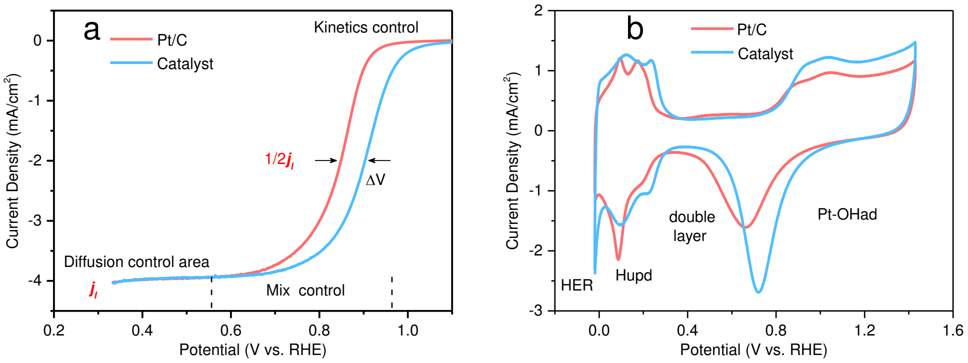

Fig. 2.4 Typical electrochemical a) CV and b) LSV curves of benchmark Pt/C and as-synthesized catalyst, and the characteristics/parameters used to compare their activity.

Stability is another important factor of ORR catalyst. Catalyst durability is measured by cycling the potentials with a potential window between 0.6 and 1.0 V in O_2–saturated electrolyte.[141] The CV and LSV curves are measured before and after this durability cycling, to compare and evaluate the catalyst stability. Smaller the shift of LSV and less decrease of specific area mean better durability.

The more direct approach to measure the performance of ORR catalyst is membrane electrode assembly, and determination of its performance as a fuel cell device, in namely two–electrode configuration. And finally, its performance is compared with the benchmark catalyst of state-of-the-art carbon loaded platinum catalyst. However, it is generally impractical due to the membrane electrode assembly and characterization are time consuming, require specific equipments, accurate control of gas pressures, temperature, and relative humidity, and abundant catalyst materials. Besides, it loses advantages of detail analysis of a single electrode electrochemical behavior, as a standard benefit of three–electrode setup.

For oxygen reduction catalysis measurement, the as-synthesized FePtCu nanoparticles and Vulcan XC-72R carbon black with a mass ratio of Pt : C = 1 : 2 were mixed in 2 mL hexane solvent and sonicated for more than 1 h to form uniform colloid. Then the organic surfactants on FePtCu were removed by low temperature thermal treatment at 300 °C for 2 hours in 5% H_2/Ar atmosphere, followed by dispersing FePtCu/C in 1 mL of isopropanol and 20 μL of 5 wt% nafion solution under sonication for 15 min to form a uniform ink. Commercial Pt/C (20 wt. % loading) was suspended in a mixture of deionized water, isopropanol, and Nafion (v/v/v = 4/1/0.05) to form an ink. Then, FePtCu/C catalysts along with commercial Pt/C were deposited on a rotation disk electrode (RDE, Pine) with a glassy carbon surface, and were evaluated for their catalytic ORR performance in Ar/O_2 saturated 0.5 M H_2SO_4 electrolyte or 0.1 M $HClO_4$ electrolyte. For the measurement of the electrochemical properties of these as-prepared electrodes, cyclic voltammetry (CV) and linear sweep voltammetry (LSV) were recorded via a computer controlled electrochemical workstation (CHI660D). As-fabricated FePtCu or Pt/C electrodes wre used as the working electrodes, and an Ag/AgCl electrode as the reference electrode and a Pt wire as the counter electrode.

2.3 TEM

The principle of the transmission electron microscope (TEM) is similar to that of the optical microscope, but in this case, the used light comes from high energy electrons. Fig. 2.5 illustrates a TEM instrument with its components and according working mechanism. TEM optical system contains three sections, the electron source, the illumination system, and the imaging system.[146] The electron gun, along with two or three condenser lenses are used to shape the electron beam that illuminates the thin specimen. The diameter of the beam and the intensity in the final TEM image are governed by the illumination design and operation, because the electron beam passes through a set of condenser lenses focusing the beam of electrons with a desired diameter. The beam-specimen interactions occur at the objective lens system, where the specimen is positioned. As the source can be considered as a point located far from the objective, which is a convergent lens, two basic images are formed at this level, a diffraction pattern in the focal plane and an image in the image plane, both are then further magnified by the post specimen imaging system. On this, the illumination system is used to shape the beam either as parallel or convergent. Whereas the parallel beam is extensively used for conventional microscopy investigations in imaging and diffraction for investigation of structure, as well as defect up to atomic scale, the convergent mode applies to scanning TEM (STEM). The imaging system generates a magnified image or a diffraction pattern of the specimen on a fluorescent screen or on a CCD camera system. The operation of this imaging system determines the magnification of the TEM image, while the spatial resolution that can be obtained from the microscope, is largely influenced by the design of the imaging lenses. Image contrast and quality can be modified using apertures such as the condenser aperture and/or objective aperture.

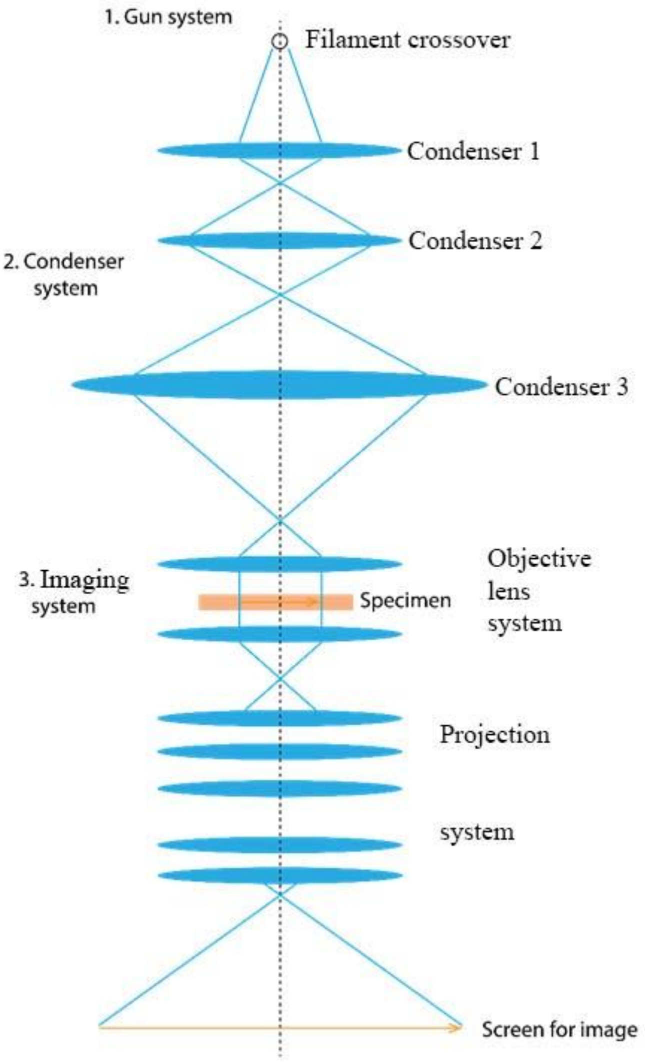

Fig. 2.5 Main components and working optical diagram of TEM.

Electron microscopes employ electromagnetic lenses so that they can control the electron beams and form images. The function of the lenses is to transform a point of an object into a point of an image, and to focus parallel rays to a point in the focal plane of another lens. The behavior of all the lenses in a standard TEM can be approximated to the action of a converging glass lens on visible monochromatic light. Electromagnetic lenses consist of two parts: a windings of wire and a cylindrically symmetrical core, namely, pole piece. The pole piece is soft magnetic material, such as soft iron, with a hole drilled through it. By controlling current applied to the windings of wire, we can generate an adjustable magnetic field in this hole, where the incident electron beam pass through. The electrons follow a helical trajectory which converges at a fine focal point after they emerge from the lens.

In TEM, there are two or three condenser lenses between the electron gun and the specimen. The condenser system allows for the control of the beam spot size and the beam convergence angle. The condenser lens system of TEM performs the following tasks:[147]

1) Focusing of electron beam on a specimen, and sufficient image intensity even when magnification is high
2) Producing of a small electron probe for microanalysis, microbeam electron diffraction techniques and the scanning electron microscopy mode

The objective lens is the most important lens in TEM: it forms the images and diffraction patterns of specimen, which are magnified by the following lenses. At the specimen surface, an image of the electron density distribution is formed by the objective lens. A diffraction pattern is generated in the back focal plane of the objective lens and then the combination of the diffracted beams forms an image in the image plane of the objective lens. The projection lenses below the objective lens are used to focus and further magnify the image or the diffraction pattern onto the viewing screen. An ultimate magnification is reachable by the use of these lenses each capable of a magnification of up to twenty times. The first projector lens in the column is generally named as intermediate lens, which can switch between the image mode and the diffraction mode. In diffraction mode, the intermediate lens focuses on the back focal plane of the objective lens, thus, the diffraction pattern is projected onto the viewing screen. In image mode, the intermediate lens focuses on the image plane of the objective lens, and the image of project is projected onto the viewing screen. To attain quantitative information about the materials microstructure, the TEM can be employed to generate several image types or diffraction patterns obtained from desired regions of the specimen. An objective aperture is situated near the objective lens. The aperture limits and controls the collection angle of the lens and therefore the angular spread of the electrons.

2.3.1 Aberration corrected TEM

The magnetic lenses in TEMs cannot be made free from aberrations and will change the phase and amplitude of the electron wave as it passes through. There are many aberrations which characterized by the corresponding aberration coefficients, that have been discussed in detail by Haine and Cosslett.[148-149]

For instance, the spherical aberration (coefficient Cs) causes the image to be blurred because points are imaged as discs, as shown in Fig. 2.6. It is due to that the lens has uneven strength from its edge and center, stronger in the edge part and weaker in the center part. Thus, the focus point of lens edge is closer to the lens, as compared to the center part of lens. We then have a blurred disk with least confusion, and its radius Δr_s can be given by $\Delta r_s = Cs \cdot \beta^3$, where *Cs* is the spherical aberration constant, β is the lens aperture.[150-151]

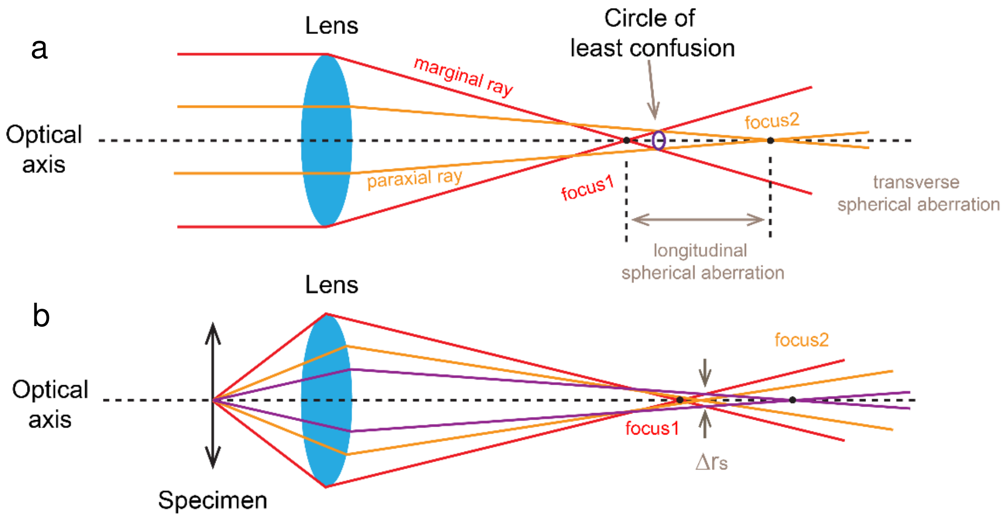

Fig. 2.6 Schematic diagram of aspherical aberration for a) focusing an initially parallel beam, and b) focusing electrons from an object.[150]

Therefore, the point resolution deteriorates with increasing β. The mechanism for aberration correction was suggested more than 60 years ago by Scherzer with pioneering attempts to reduce it to practice by Crewe, Rose, Haider, Krivanek and others over the last 60 years. Essential to successful *Cs* correction is precisely control the corrector alignment, which finally is possible today also because of advances in computer technology. Two distinct paths have been and are being pursued for *Cs* correction hardware: hexapole systems for TEM, quadrupole and octupole systems for STEM. Fig. 2.7a shows the optical image of a *Cs* corrector, consisting of a hexapole and other transfer lens, which can be adjusted and kept stable with a high accuracy. Fig. 2.7b shows its working mechanism. While the hexapole design exhibits relative simplicity, it is not simply extendable for *Cc* correction and has larger intrinsic *Cc*. The quadrupole/octupole design can be extended to *Cc* correction with addition of electrostatic elements (Wien Filter, a device consists of perpendicular electric and magnetic fields that can be used as a velocity filter for charged particles), but the configuration is much more complex and exhibits large off-axis aberrations, the latter is more suitable for STEM for which the effects of *Cc* are mitigated by high angle annular dark field imaging.

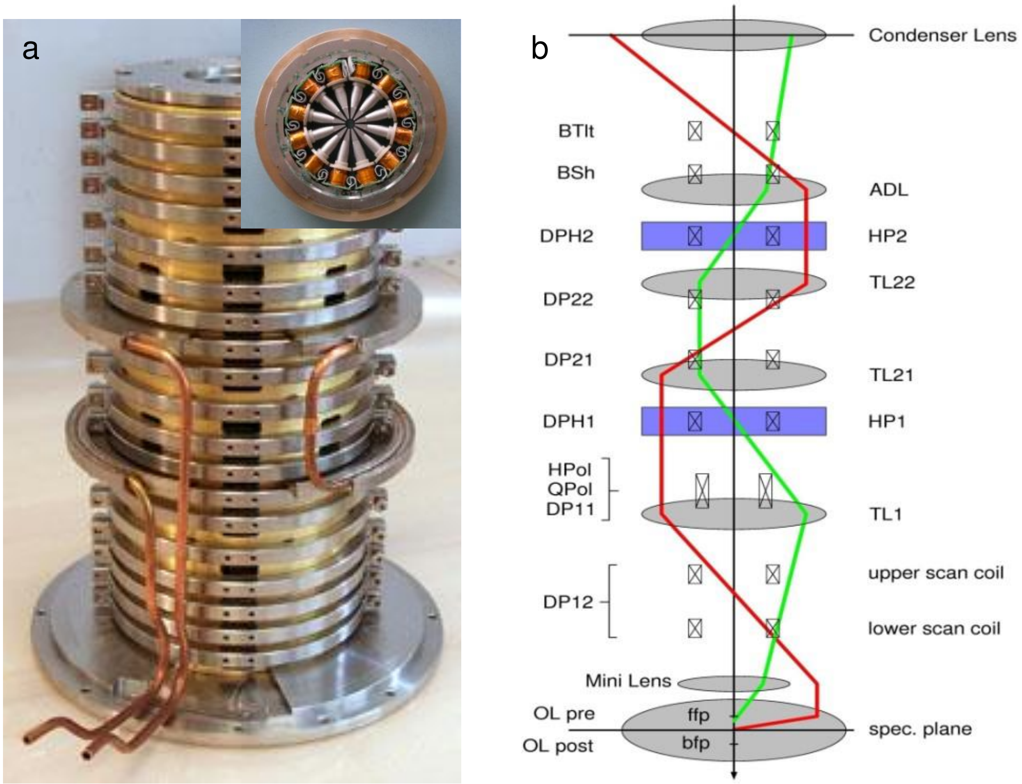

Fig. 2.7 a) An optical side-view image of a spherical corrector, the inset is its top view image. b) The ray diagram for correcting *Cs* by a corrector.[151]

The chromatic aberration arises because of variation of electron wavelength/energy, resulting in spread of the electron beam. It leads to a rainbow distribution at the edge of an image because light of different color is refracted at different angles. A disc of confusion, radius r_c is produced, given by $\Delta r_c = Cc \cdot \beta \cdot \Delta E / E_0$, where Cc is the chromatic aberration constant of the lens or chromatic coefficient, ΔE is the deviation of the electron energy from its mean value E_0.

Astigmatism occurs when the lens exhibits different focal lengths, depending upon the plane of the ray paths. Thus, again a point on the object is imaged as a disc of confusion, radius Δr_A, given by $\Delta r_A = \Delta f_A \cdot \beta$, where Δf_A is the maximum difference in focal length from astigmatism. This defect may be corrected using electromagnetic lenses that produce a small controllable magnetic field.

2.3.2 TEM, HRTEM and STEM Imaging

The most standard mechanism, which takes part in the image contrast formation in the TEM, is mass-thickness contrast. This contrast originates from incoherent elastic scattering of electrons. As electrons penetrate the specimen, they are scattered by elastic nuclear interaction. Hence, the image formed from thick regions appears darker due to the less electrons transmitted from that region. In contrast, the image formed from a thin area, appears brighter in the image plane due to the less scattering occurred in that area. Contrast in TEM images can be also due to the electron waves phase difference, which are scattered through a specimen. Whereas bright- and dark-field TEM modes usually use only the direct beam or a single diffracted beam, the phase contrast method uses the interference of two or more beams. Phase contrast imaging is the basis for the so called high-resolution TEM (HRTEM).

The spatial resolution of the conventional transmission microscopes is determined by the objective lens optical quality as most of the scattering for image formation takes place inside. For imaging purposes, the TEM objective lens role can be represented by a contrast transfer function (CTF), which modulates the amplitudes and phases of the electron diffraction pattern formed in the back focal plane of the objective lens, and thus shows the phase shifts due to the combination of spherical aberration and defect of focus. The phase shift of the objective lens can be represented by a single phase factor χ, given by,

$$\chi(u) = \pi \Delta f \lambda u^2 + \frac{1}{2}\pi C_s \lambda^3 u^4 \tag{2.10}$$

where *Cs* is the spherical aberration coefficient, λ is the wave length of electrons, *Δf* is the defocus value, *u* is the spatial frequency.

The phase contrast in the formed image follows the fluctuations of the CTF. The presence of zeros in the CTF means that we have gaps in the output spectrum, which do not contribute to the output signal: it is as if these frequencies were filtered out. In 1949, Scherzer put forward that the CTF could be optimized by balancing the effect of spherical aberration against a particular negative value of *Δf*, known as Scherzer defocus, which occurs at

$$\Delta f_{Sch} = -1.2\sqrt{C_s \lambda} \tag{2.11}$$

At this defocus all the beams will have nearly constant phase out to the first crossover of the zero axis. Up to this crossover point, the CTF has the same phase and the contributing frequencies are easily interpretable. This crossover point is defined as the instrumental resolution limit by the reciprocal value of the first crossover value,

$$r_{Sch} = 0.66 \sqrt[4]{C_s \lambda^3} \tag{2.12}$$

This is the best performance that can be expected from a microscope unless we use image processing schemes to extract more information. After the crossover, oscillations in the CTF make the information at high spatial frequencies difficult to interpret. However, if the CTF is fully known for the instrument used, image reconstructions from focal or tilt series can make use of these frequencies. All spatial frequencies are then sampled and transferred to the same phase in the CTF to form a reconstructed image. The resolution limit in such an image is in theory the information limit of the microscope as determined by the envelope damping function. The effect of the envelope is to impose virtual aperture in the back focal plane of the objective lens, regardless of the setting of focus. CTF concept is also used in STEM mode derived by Cowley, also called electron *Ronchigram* CTF.[152]

After the practical realization of the *Cs* corrector, more materials science questions have been addressed. Atom column dumbbells can be imaged correctly. Optimum contrast conditions were found for high resolution imaging with spherical aberration corrected instruments, which are negative Cs imaging conditions – that means negative Cs and over focus – resulting in white atom contrast on dark background. They are especially useful for imaging weakly scattering centers or light atoms especially in the surrounding of strongly scattering heavy atoms, which was not possible before.

In STEM, a small convergent electron probe scans over a specific region of a sample. At each spot, the generated signal is simultaneously collected by selected detectors to generate an image. As shown in Fig. 2.8, three types of detectors are used to obtain STEM images: BF detector, annular dark field (ADF) detector, and high angle ADF (HAADF) detector. The BF detector collects the direct beam from a point on the specimen, with a scattering angle $\theta < 10$ mrads. The ADF detector is a disk with a hole in its center. The ADF image formation is similar to the diffraction mode in TEM, with $10 < \theta < 50$ mrads. The measured contrast mainly originate from the electrons diffracted in crystalline areas, it also comes from the incoherent Rutherford scattering. For HAADF, the hole of the detector is Larger than in ADF with $\theta > 50$ mrads. Thus, it detects electrons that are scattered to higher angles and almost only incoherent Rutherford scattering contribution to the image.

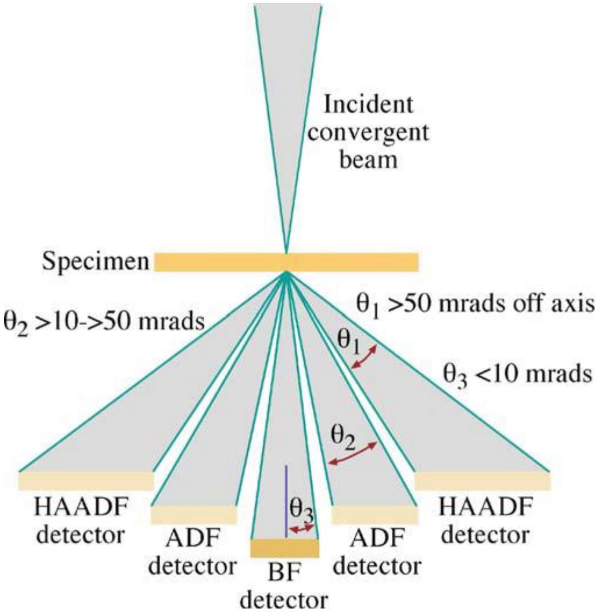

Fig. 2.8 The various electron detectors in a STEM.[151]

The electrons scattered outside the illumination cone are used for dark-field imaging and can be called ADF. Both thermal diffuse scattering (TDS) and Bragg scattering make important contributions to the ADF images. Therefore, as a rough guide, the inner collection semi-angle should be at least three times the convergence semi-angle for incoherent imaging, and ideally amounts to five times to eliminate effects of thickness oscillations in crystals. Imaging with electrons scattered at such large angles is called HAADF STEM imaging, which is dominated by localized TDS favoring a simple interpretation in terms of an incoherent imaging mode and shows atomic number contrast owing to predominant electron scattering at the potential of the nucleus, similar to Rutherford scattering. It is known that the intensity in HAADF STEM images is proportional to $t \cdot Z^a$, where t is a sample thickness, Z is the atomic number of an element and a is a parameter between 1.5 and 2.0, depending on the exact sample composition and detector geometry. For qualitative determination of atom species and calculations of atomic column distances, HAADF STEM imaging is widely used due to the simple interpretation and the absence of contrast reversal. However, quantitative interpretation of the intensities in HAADF image needs simulations for comparison.

The large central hole of the HAADF detector allows convenient integration with EELS, which allows atomic–resolution imaging to be obtained simultaneously with chemical analysis. Currently, STEM images are widely used for lattice displacement analysis although images distort due to sample drift and scan distortions make the measurement challenging. This can be overcome by fast acquisition of multi–frame images and post–processing of image stack with advanced image alignment methods.[153-156] With these methods, few picometers measurement precision can be achieved for STEM EELS spectrum imaging.[153]

2.3.3 Analytical EDX and EELS

The interaction of the TEM energetic electron and the thin lamella generates numerous signals that can be usefully detected for the local characterization of the sample (as shown in Fig. 2.9). The directions shown for each signal do not always represent the physical direction of the signal, but indicate, in a schematic way, where the signal is strongest or where it can be detected.[151]

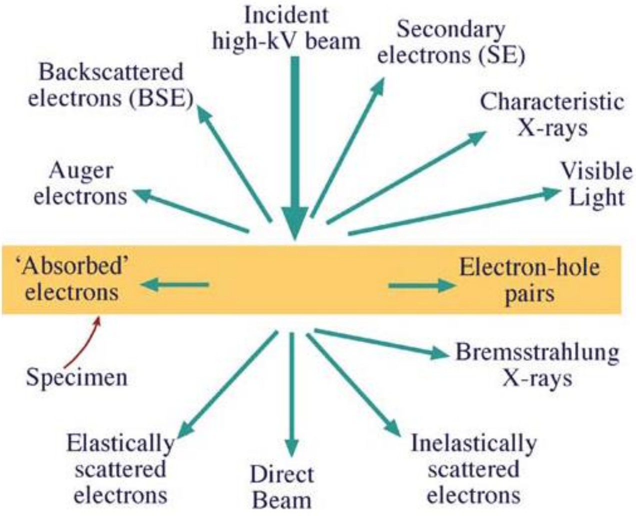

Fig. 2.9 Signals generated when a high-energy beam of electrons interacts with a thin specimen.

EDX

Energy dispersive X-ray spectroscopy (EDX) is a qualitative and quantitative X-ray analytical technique that allows for the identification of elements with atomic number $Z > 3$ as well as for elemental ratio quantification. EDX is considered as a non-destructive analytical technique, that is, the sample can be reanalyzed many times. However, very often materials can damage under the electron beam. Using this method, a quick overview of the elements present in the solid specimen can be obtained. An electron beam is focused on the sample and the electrons from the primary beam penetrate the sample and interact with its atoms. The X-rays resulting from these interactions are further detected by an energy dispersive detector which displays a spectrum of intensity (number of X-rays) versus energy. The energies of the characteristic X-rays allow for the identification of the elements of the sample, while the intensities of the characteristic X-ray peaks allows for the quantification of the concentrations of the elements. However, to obtain the real concentrations, certain corrections to the raw intensities are needed. The general approach for thin samples (*i.e.* absorption or fluorescence within the sample can be neglected) in TEM is the Cliff-Lorimer method. In this method, for a binary system (a substance composed of two elements A and B), characteristic X-ray intensities I_A and I_B are measured. Then, the concentration ratio of the two elements C_A/C_B is obtained from the equation $C_A/C_B=k_{AB}\cdot I_A/I_B$, where k is termed the Cliff-Lorimer factor (or k-factor) which is related only to the atomic-number for thin samples (the X-ray absorption and the fluorescence are minimal). The Cliff-Lorimer factor can be different in each TEM/EDX system and it depends also on the voltage being used. For ternary or higher order systems, the same equation applies to each pair of elements (AB, BC, etc.) keeping in mind that the assumed elements must constitute 100% of the specimen ($C_A + C_B + \ldots + C_{\mathrm{N}} = 100\%$).

EELS

Electron energy-loss spectrometry (EELS) analyzes the changes of the kinetic energy of electrons that have come through the specimen, displayed as a spectrum as a function of electron intensity and loss of electron energy. By analyzing the spectrum, the chemistry, electron structure and bonding information of specimen can be extracted at even atomic scale, making EELS highly a powerful technique in material science. There are three distinct regions in an EELS spectrum, *i. e.*, a zero-loss, a low-loss and a core-loss regions, according to various energy-loss mechanisms. The working condition of STEM-EELS acquisition and related mechanisms are shown in Fig. 2.10. We can see its advantage that ADF imaging and analytical spectrum can be simultaneously obtained. As compared to EDX, EELS are more analytical sensitive and with higher spatial resolution, while EELS require thin enough specimen to get information and enough understanding of processing the spectra.

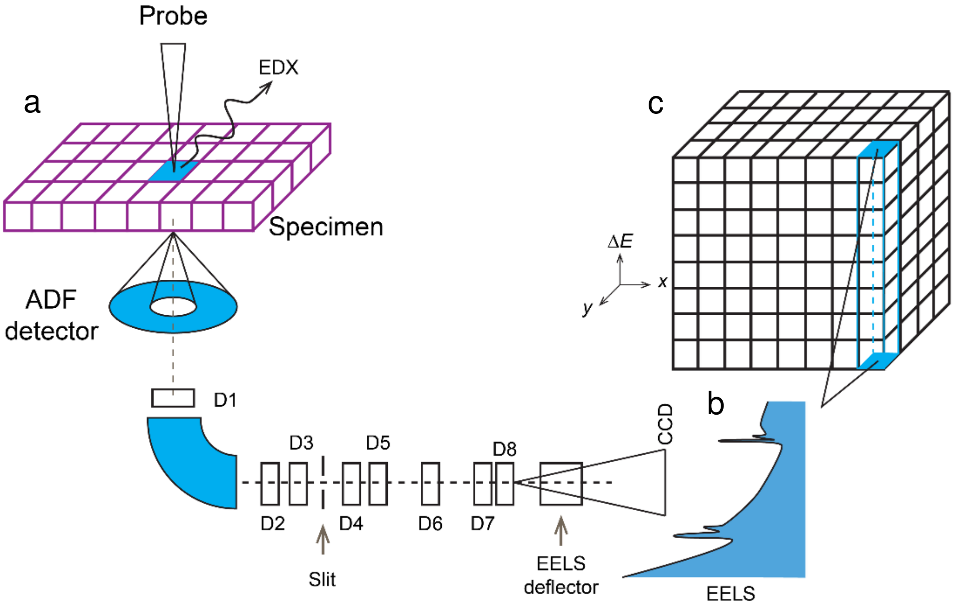

Fig. 2.10 A schematic working diagram of electron loss spectroscopy and type of spectrum that can be acquired a) interaction and detection, b) spectrum image, c) an individual spectrum, detected intensity versus the lost energy.

This technique constitutes a powerful method which bring about detailed analytical data from a sample in an electron microscope equipped with scanning mode and an adequate spectrometer. By acquiring multimodal data in scanning mode, a highly accurate information about the local chemistry and electronic structure from precise positions within a scanned image is obtained.

EELS zero-loss region

One of the main features of EELS spectrum is the zero loss peak (ZLP), primarily originated from unscattered electrons, elastic scattered electrons, and electrons suffered only a slight energy loss (less than the width of the ZLP). The width of the ZLP reflects the energy spread of the primary electrons and the resolution of the spectrometer. It also provides the energy resolution for the final EELS spectrum, which indicates how much detail can be expected from the low-loss and core-loss region (note that in the core-loss region features are mostly smeared by lifetime broadening). With the use of a cold field-emission cathode, the energy resolution is typically between 0.4 eV and 0.7 eV. Therefore, phonon scattering, which occurs in the range of few tens of meV, is included in the ZLP. Only very recently further improvement of the EELS energy resolution to about 5~10 meV has opened the door to study phonons. The ratio between inelastic and elastic scattering includes the sample thickness information. In addition, the ZLP together with the low-loss region provides the information for removing multiple scattering effects from the low loss and core-loss region.

EELS low-loss region

Inelastic scattering from outer-shell electrons leads to excitation of volume and surface plasmons, which are collective oscillations of the valence electrons, but also to interband transitions of single electrons from the occupied valence-band states into the empty states of the conduction band. The low-loss region of an EELS spectrum provides information similar to optical spectroscopy, containing valuable information about the band structure and in particular about the dielectric function of a material. This low-loss region can also include parasitic losses due to the excitation of Cherenkov radiation, which should be identified and excluded from the low-loss EELS analysis.

EELS core-loss region

Inelastic scattering at energies above 50 eV are caused by ionization of inner-shell electrons and are therefore characteristic of the atomic elements in the specimen. It is straightforward to identify the edges by looking at their edge on-set energy and comparing it with reference tables. The full range of possible edges in the energy-loss spectrum is shown in Fig. 2.11. Bonding and electronic structure only have a marginal effect on the position of these peaks. In favorable cases, when the edges do not overlap, identification and quantification can be carried out. Moreover, the specific shape near the onset of a core-loss edge contains information about the bonding and electronic structure in the material. In fact, through their interaction, the fast electron probe the locally unoccupied density of states. These studies are termed as electron energy-loss near-edge spectroscopy (ELNES). Further above the edge, extended energy-loss fine structure spectroscopy (EXELFS) can be seen as a very weak oscillations around the ideal edge shape. This deviation is caused by interference of a secondary ejected electron wave which leaves the excited electron and its backscattered waves from neighboring atoms. The technique can reveal data on the interatomic distances and the number of neighboring atoms in the specimen.

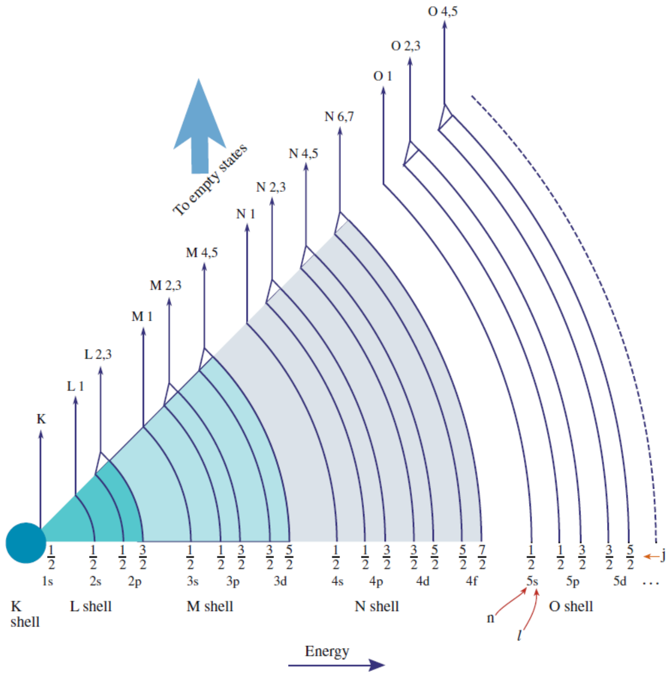

Fig. 2.11 The full range of possible edges in the energy-loss spectrum due to core-shell ionization and the associated nomenclature.[151]

2.4 Systematic characterization methods

X-ray diffraction

The crystal structure of the FePtM nanoparticles in this thesis were measured with A25 rotating anode powder X-ray powder diffractometer (Bruker D8) with Cu $K\alpha$ radiation (λ = 0.1541 nm). The FePtM powders with similar weight were put onto a standard glass XRD substrate, and then covered and flattened into a thin film by a slide glass. The working mechanism of XRD can be roughly illustrated in Fig. 2.2. The Bragg equation is derived from the reflection from a stack of parallel atomic planes according to Fig. 2.12a. The incident beam is reflected by a lattice plane with d_{hkl}, and constructive interference occurs in the condition of Bragg law

$$2\, d_{hkl}\cdot \sin\theta = n\cdot \lambda \tag{2.13}$$

Fig. 2.12a provides an elegant visual description of what goes on when X–rays are scattered by a crystal, however, it can not explain the understanding and value of n for practical measurement. The n is normally simplified to 1 in powder XRD, as can be shown in the reflection sphere in Fig. 2.12b. The reflection sphere has a radius of 1/λ. Then we can modify equation above into

$$1/\lambda\cdot \sin\theta = 1/2\ d_{hkl}{}^{*} = 1/2\cdot (1/\,d_{hkl}) \tag{2.14}$$

$$d_{hkl} = \lambda/(2 \sin\theta) \tag{2.15}$$

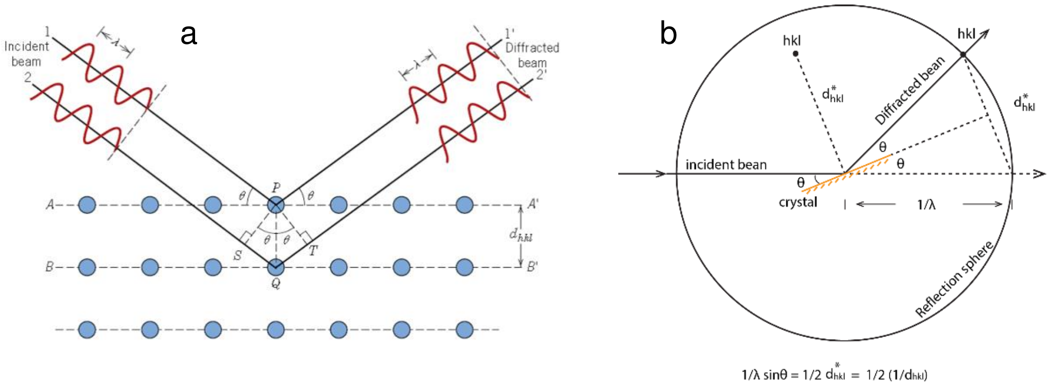

Fig. 2.12 a) Geometry of the Bragg reflection analogy and b) a schematic of the $\theta \sim 2\theta$ geometry with a X-ray incident beam and the diffraction beam.

The chemical ordering degree of FePt can be calculated based on integrated intensities of XRD spectrum according to eqn 2.16

$$S = 0.85\,(I_{001}/I_{002})^{1/2} \tag{2.16}$$

Other characterization methods are also used in this thesis. For instance, the size and morphology of the nanoparticles were characterized using field emission scanning electron microscope (FESEM, JSM7100F JEOL). The composition of the FePtAg nanoparticles was measured by X-ray Fluorescence (XRF 1800, Tsushima) and inductively coupled plasma atomic emission spectroscopy (ICP-OES). The magnetic properties of the FePtAg nanoparticles were measured to characterize the ordering of FePtM, by using a Quantum Design Physical Property Measurement System (PPMS). The particle size analysis is carried out by ImageJ software.[145]

Chapter 3

Ordered FePtAg nanoparticles with super fine size

3.1 Introduction

From above analysis, we can find that direct one–pot synthesis of ordered FePt with Au or Ag can efficiently enhance the chemical ordering of magnetic FePt nanostructures with minimum preparation processes. However, an additive always promotes particle growth and decreases their size and shape uniformity, due to a ternary metallic structure. Therefore, to optimize the one–pot synthesis method, it is very important to optimize the synthesis procedures of FePt to systematically obtain nanoparticles with small and uniform grain size. This objective is reached by understanding and controlling the solvent effects that have been extensively studied in organic reactions.[116, 157] Indeed, solvents influence the rates of chemical reactions, chemical equilibria, product yielding rate and even the chemical reaction processes. Obviously, various inorganic FePt nanostructures with controlled morphologies can be produced in different organic solvents. For instance, spherical FePt nanocrystals, FePt obloids, and FePt nanorods can be obtained in dioctyl ether, benzyl ether/octadecene, and oleylamine solvents.[158] FePt nanowires have been found to be strongly solvent–dependent and organic amine plays an important role in the reaction.[159] Therefore, the solvents should be carefully chosen as they have strong effects on controlling the synthesis of FePt nanostructures. Based on these considerations, we investigated the ordered FePt nanoparticles synthesis in three different high–boiling temperature solvents of octadecylamine, hexadecylamine and trioctylamine, respectively.[118] The silver additive was chosen to promote the phase transformation, it is cheaper and easier to remove by acid washing as compared with gold. The morphology, structure and magnetism of FePtAg nanoparticles were investigated in detail and the solvent effect on the FePtAg nuclei and growth have been carefully investigated and will be discussed in the following.

3.2 Results

To characterize the structure of the as-synthesized FePtAg nanoparticles, we carried out XRD measurement. Fig. 3.1(a) illustrates the XRD patterns of the FePtAg nanoparticles synthesized in the above different solvents. The diffraction peaks at 24.0, 32.9, 41.2, 47.4, 53.5, 70.8 and 83.7° exactly match the (001), (110), (111), (200), (201) and (311) planes of the *fct*–FePt (pdf No. 43–1359), indicating that the as-made nanoparticles were partially $L1_0$ phase, which is consistent with the desired ordering we aimed at. The diffraction peaks at 37.9, 44.2 and 64.7°can be assigned to the (111), (200), and (220) planes of metal Ag (pdf No. 1–1167). As can be seen, the (001) and (110) peaks of the *fct*-FePtAg synthesized in octadecylamine are stronger than in hexadecylamine and octadecylamine, which is a clear evidence of the important role of the solvents.

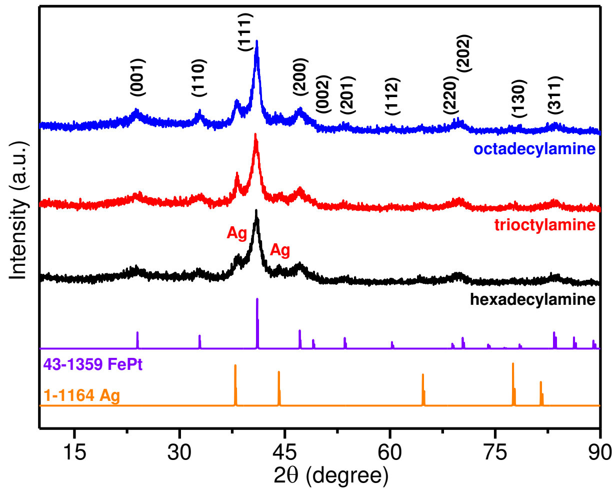

Fig. 3.1. XRD patterns of the as-synthesized FePt nanoparticles in three different solvents of hexadecylamine (black), trioctylamine (red) and octadecylamine (blue), as well as standard XRD spectra of $L1_0$-FePt (PDF 43-1359) and Ag (PDF 1-1164).

To confirm the high ordering of the FePtAg nanoparticles, we carried out magnetism analysis by PPMS. Room temperature measurement of the magnetization shows that the as-synthesized FePtAg (Fig. 3.2) exhibits a hysteresis meaning that the partially ordered FePtAg nanoparticles are ferromagnetic at room temperature. The corresponding coercivity is 2.84 kOe, 2.81 kOe, and 5.23 kOe for hexadecylamine, trioctylamine and octadecylamine solvents, respectively. FePt based nanoparticles with this magnitude coercivity, synthesized by one-pot method, is the first time to be reported as far as we know. Fig. 3.2d illustrates the order parameter and coercivity change along the solvents. The order parameter S^2 was determined by the ratio of the integrated intensity of the (110) and (111) peaks. The calculated S^2 is 0.199, 0.168 and 0.165 for octadecylamine, hexadecylamine and trioctylamine, respectively. Therefore, the FePtAg nanoparticles synthesized in octadecylamine have largest ordering parameter and coercivity.

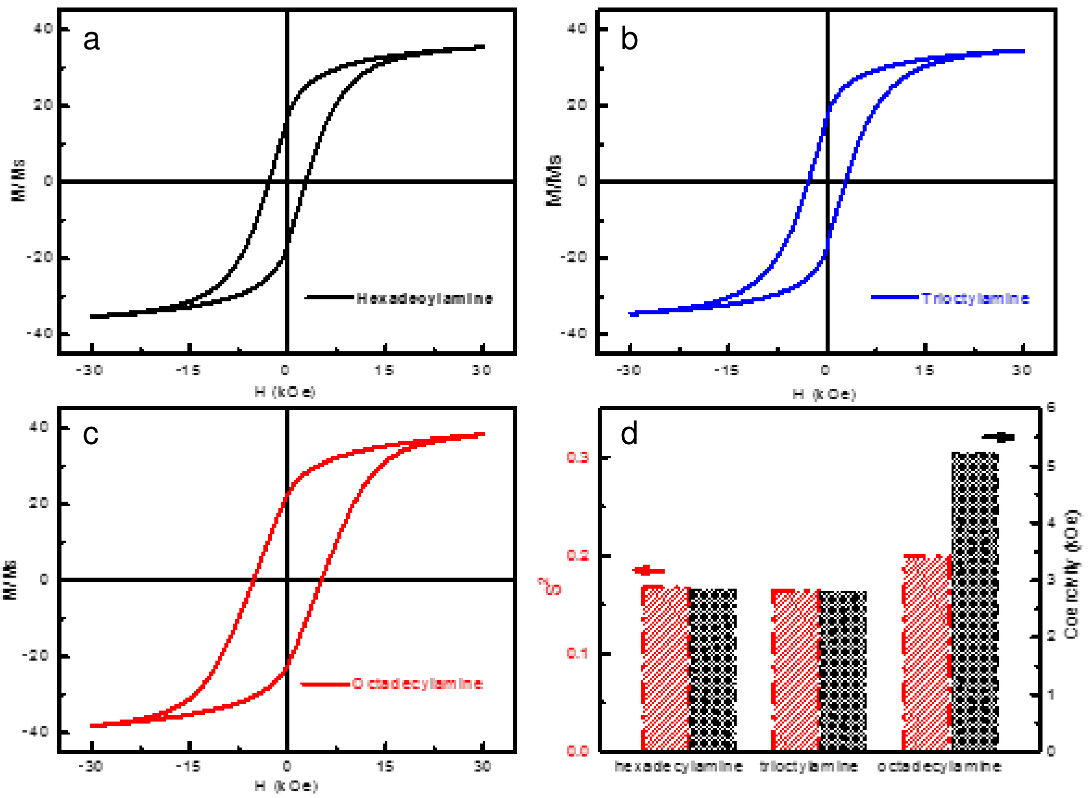

Fig. 3.2 Room temperature hysteresis curves of the synthesized FePtAg particles within hexadecylamine a), trioctylamine b), octadecylamine c) solvents, and d) the calculated chemical order parameter and the room temperature coercivity as a function of the solvents.

In order to characterize the size and morphology of the as-synthesized FePtAg nanoparticles in three different solvents, we performed TEM measurement. Low-magnification and high-magnification images of the FePtAg nanoparticles synthesized in these solvents can be seen in Fig. 3.3a~c). As can be seen in the high-magnification images (Fig. 3.3 d~f)), the FePtAg nanoparticles synthesized in hexadecylamine and octadecylamine exhibit a spherical morphology with uniform size distribution (Fig.3.4 c and f). While, FePtAg synthesized in trioctylamine are highly sintered, with a wide size distribution (fig. 3.4e).

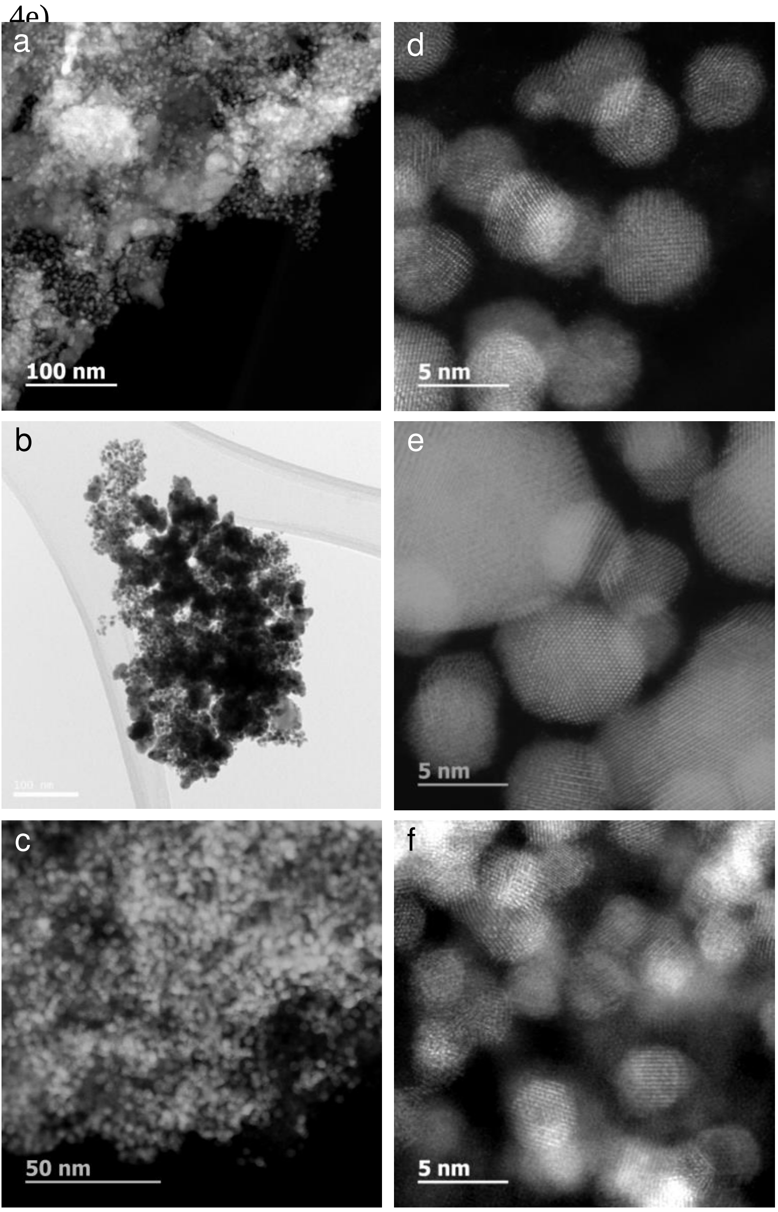

Fig. 3.3. a~c) Low magnification TEM pictures for FePt Ag synthesize in octadecylamine, hexadecylamine and trioctylamine solvents, respectively. d~f)According high magnification TEM images.

Size distribution of these three type particles is summarized in Fig. 3.4 by the box chat plot, the mean particle diameter and dispersion of the FePtAg nanoparticles increase in the sequence octadecylamine<hexadecylamine<trioctylamine. The FePtAg based nanoparticles synthesized in octadecylamine shows smallest particle in size (~3.5 nm) and with most uniform distribution. It is well known that the coercivity of magnetic grains is affected by both the degree of ordering and the particle volume, and FePt nanoparticles with larger size are easier to order during thermal treatment. It is meaningful that our ~3.5 nm FePtAg nanoparticles synthesized in octadecylamine show small enough particle size and substantial coercivity.

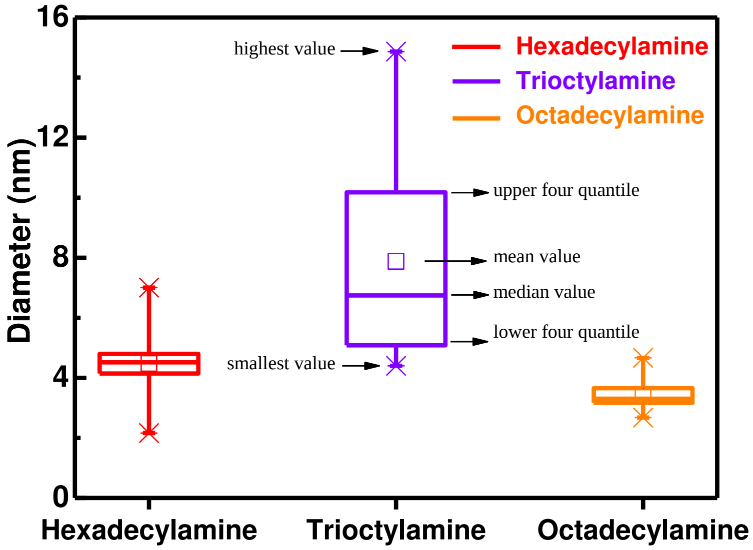

Fig. 3.4 The size distribution of the synthetized FePtAg nanoparticles. The box is determined by the upper four quantile and the lower four quantile. The hollow point in the box is the mean size, the cross line in the box is the median size, the whiskers above and below the box represents the highest value and the smallest size, respectively.

To characterize the element distribution of Fe, Pt, and Ag in the nanoparticles, we carried out STEM EDX and EDX mapping measurement. Fig. 3.5a shows the low magnification TEM image of FePtAg nanoparticles synthesized in hexadecylamine solvent. The EDX spectrum confirms the composition of FePtAg nanoparticles is consisted with Fe, Pt, and Ag. The extra Cu peak could be assigned to the carbon coated Cu grid used for loading the nanoparticles. EDX spectral images demonstrate that Fe, Pt, and Ag atoms are distributed in each particles, and Ag atoms could be with lower content in the smaller particles, as shown in Fig. 3.5 c)~e).

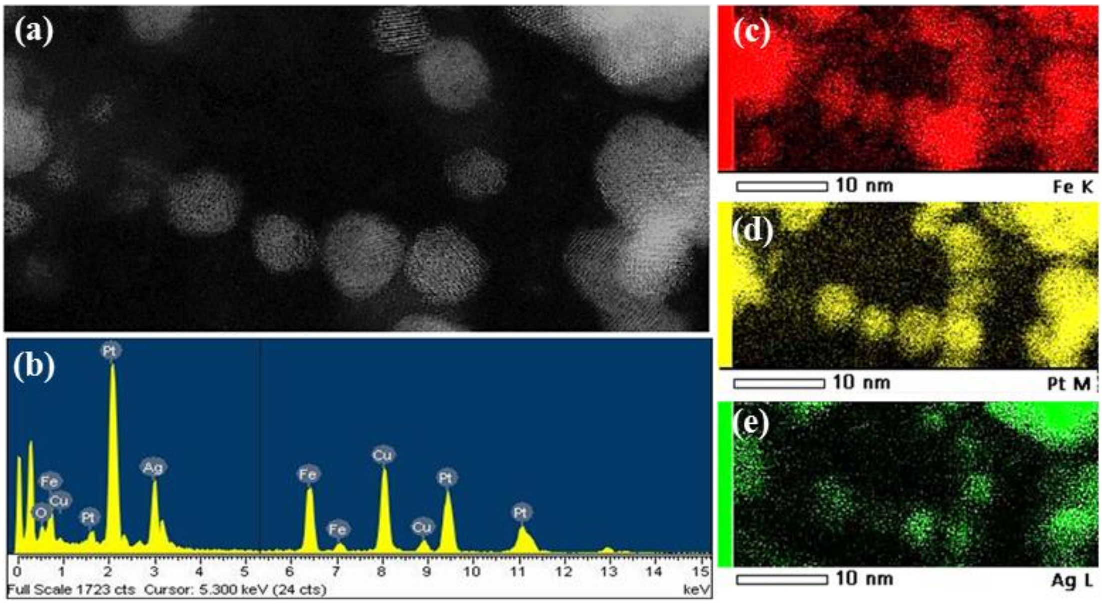

Fig. 3.5 HAADF-STEM image and EDXS analysis. (a) Low magnification HAADF-STEM image of FePtAg nanoparticles synthesized in hexadecylamine. (b) STEM-EDXS spectrum of FePtAg nanoparticles. EDXS elemental mapping with separate maps shown for Fe (c), Pt (d), and Ag (e).

The compositions of the as-synthesized FePtAg nanoparticles were measured by XRF, as shown in Table 3.1. $Fe_{49}Pt_{39}Ag_{12}$ was obtained by using hexadecylamine solvent, and $Fe_{51}Pt_{39}Ag_{10}$ was obtained for both trioctylamine and octadecylamine, indicating Fe rich phase of the as-synthesized FePtAg nanoparticles. FePtAg synthesized in three different solvents have minor difference in composition, demonstrating that similar processes occurred during the synthesis.

Table 3.1. The composition of as-synthesized FePtAg nanoparticles in three solvents

Solvent	Precursor	XRF results
Hexadecylamine	$Fe_{36}Pt_{36}Ag_{28}$	$Fe_{49}Pt_{39}Ag_{12}$
Trioctylamine	$Fe_{36}Pt_{36}Ag_{28}$	$Fe_{51}Pt_{39}Ag_{10}$
Octadecylamine	$Fe_{36}Pt_{36}Ag_{28}$	$Fe_{51}Pt_{39}Ag_{10}$

3.3 Discussion

Up to now, silver has been largely studied for the process of the phase transformation of the $L1_0$ FePt. Understanding the location of the third element and mechanisms by which the additive influence the $L1_0$ ordering process would assist in the development of FePt media. So far, two main mechanisms are predominant in order to explain the role of Ag in the ordering of PtFe.

3.3.1 The strain effect

This was proposed by Hsu *et al.* that Ag underlayer had been used to reduce the FePt ordering temperature, due to the slightly larger unit cell as shown in Table 3.2.[160] The FePt unit cells were reported to stretch in the film plane by XRD analysis. At the same time, there was a contraction of the FePt unit cells along the plane normal direction, which results in the $L1_0$–FePt ordering at reduced temperature. This was explained as the strain induced by crystalline misfit, as supported by the subsequent studies of Xu et al. and Kang et al.[161-162] With a 4 nm Ag top layer on the FePt layer, the phase transformation temperature of the FePt film can decrease.[163] X-ray photoelectron spectroscopy (XPS) analysis indicates that Ag diffused into FePt grains, meanwhile, the $L1_0$–FePt phase transformation was promoted. The diffusion of Ag into the FePt layer can increase the mobility of the atoms and result in further crystallization of the film. Moreover, the volume expansion caused by the diffusing Ag atoms could supply large elastic energy to the FePt grains which facilitates the structural transformation.

Table 3.2 Atomic volume summary of relevant atoms

Atom	**Atomic radius (Å)**	**Atomic volume (cm^3/mol)**
Fe	1.56	7.1
Pt	1.77	9.1
Ag	1.65	10.3
Au	1.74	10.2
Cu	1.45	7.1

3.3.2 Diffusion effect

The diffusion of Ag into the FePt layer can increase the mobility of the atoms and result in further crystallization of the film. Moreover, the volume expansion caused by the diffusing Ag atoms could supply large elastic energy to the FePt grains which facilitates the structural transformation. For the location of silver in FePtAg alloys, Chen et al. performed anomalous X-ray scattering (AXS) and extended X-ray absorption fine structure (EXAFS) studies and concluded that a small part of Ag was in FePt lattice by replacing Fe, while most of Ag segregated from FePt and formed fcc phase.[164] First principles study demonstrated that Ag atom substituting for a Fe site is more energetically preferable than that of substituting for a Pt, thus Ag atom should replace Fe site.[165] Wang et al. studied Ag addition effects on FePt ordering by in-situ heating in HRTEM, they reported that Ag atoms segregate from the FePtAg grain first to form an amorphous nucleation center at the grain boundary and then grow/crystallize as more Ag atoms come in this area, accompanied by the ordering transition of the mother grain.[166] From our perspective, the FePtAg could first nucleate as a disordered solid-solution state. Subsequently, the Ag atoms diffuse out of the FePt lattice, during the parallel FePt transformation to the $L1_0$ crystal structure due to diffusion/defect which mechanism is consistent with above literature.

3.3.3 The role of the solvents

Solvents can affect the rates of chemical reactions, chemical equilibria, product yielding rate and the chemical reaction mechanism and various inorganic FePt nanostructures with controlled morphologies have been produced in different organic solvents. However, the solvent effects were rarely discussed due to complex organic reactions occurred companied with the FePt nano-crystal growth. Besides, precursor concentration, surfactants and heating conditions always offer comprehensive effects on the FePt nanostructures. In order to study the solvents effects on controlled synthesis of FePtAg nanoparticles, we design the reaction system. The dielectric constant and viscosity of solvents are suggested to be the main factor to determine the morphology (sheet-like, herbs-like and net-like) of inorganic Co_3O_4 crystals synthesized by solvothermal method.[167] In a solvent with low dielectric constants, the concentration of ions is relatively high, corresponding to a high supersaturation and better ion diffusion capability. The solvent viscosity can impact the diffusion and nucleation rate of the Co_3O_4 nanocrystals. For our FePtAg nanoparticles synthesized by polyol process method, FePtAg simultaneously nuclei and grow at lower temperature, followed by particle growth and phase transformation at higher temperature. We suggest that more nuclei centers formed in octadecylamine than hexadecylamine and trioctylamine solvents during the nuclei process, leaving less cations in solvent. In the following crystal growth process via ion-by-ion addition, FePtAg grow slower in octadecylamine due to higher concentration of nuclei centers and lower concentration cations, thus, the FePtAg nanoparticles synthesized in octadecylamine would be more uniform and smaller in size.

3.4 Conclusions

In this section, we describe a facile solvent-assisted one-step synthesis of highly ordered $L1_0$ FePt nanoparticles. Our method is based on the formation of the FePt in the presence of octadecylamine solvent and Ag additive, which was chosen to in-situ promote the ordering. Our data show that 5.23 kOe high coercivity FePt/Ag nanoparticles with diameter of 3.5 ± 0.5 nm and very uniform size distribution can be achieved, comparing to the literature (4.8 kOe, 5.8 ± 2.3 nm diameter FePt/Au), (4.5 kOe, 6.5 ± 0.5 nm FePt/Au), (4.8 kOe, 7~15 nm FePt/Cu), and (7.6 kOe, large particle size and wide distribution FePt/Ag). Furthermore, the one-step doping method can efficiently decrease the FePt ordering temperature than postannealing technologies (>550 °C). The solvent was found to significantly affect the chemical ordering and growth of FePt nanoparticles. Replacing the octadecylamine with hexadecylamine or trioctylamine solvents, 2.84 kOe/2.81 kOe FePt/Ag nanoparticles were obtained; however, the as-synthesized particles grew bigger and were more widely distributed in size than using octadecylamine.

Chapter 4

Ordered FePtCu nanoparticles with core–shell structure and enhanced ORR

4.1 Introduction

Ordered FePtCu mineral, tulameenite, is a natural deposit of the composition of $FePt_2Cu$, which has attracted extensive research interests in 1950s. Isothermal equilibrium curves of ternary FePtCu at 600 °C and 1000 °C can be seen in Fig. 4.1.[168] From which we can see that addition of Cu can reduce the ordering temperature of FePtCu. Copper is miscible in FePt alloy system, however, the origin of this decrease in the ordering temperature is still under debate, since calorimetric studies have revealed no difference in the ordering kinetics between ternary additions of Cu to replace Pt and a Fe content higher than the equiatomic composition.[169] In experiments, Maeda *et al.* and Platt *et al.* observed that Cu improved the transformation of FePt and deduced that Cu additive increased the driving force of the FePt disorder–order transformation.[170-171] Takahashi *et al.* found that Cu promoted the ordering and suggested that Cu additive improved the diffusivity of the alloy by lowering the melting point.[172]

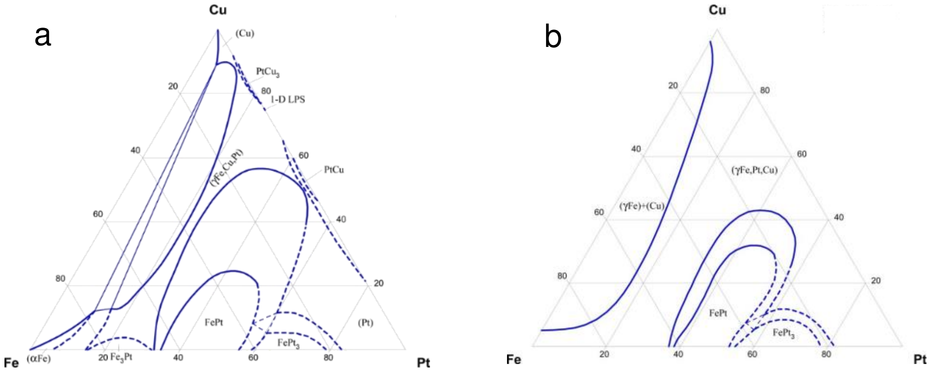

Fig. 4.1 The phase diagram of FePtCu: isothermal section at a) 600°C and b) 1000 °C, respectively.[168]

In this chapter, we report a one–pot method to directly synthesize FePtCu nanostructure with ordered $L1_0$-FePtCu structure and enhanced ORR catalysis performance.[108] XRD analysis results show predominant (001) and (110) characteristic peaks of $L1_0$ super-lattice, demonstrating that Cu doping promotes the $L1_0$ ordering. With the Cu concentration increasing from 10 percent to 30 percent, the (001) and (111) peaks of FePtCu gradually shift to higher degree than *fct*-FePt, and exactly match $L1_0$-FePtCu peaks when Cu concentration is 40%. HAADF-STEM image and EDX analysis show that as-synthesized FePtCu nanoparticles are with 30 nm mean diameter and core-shell CuFePtCu structure. The shell thickness is about 8 nanometers and the core diameter is about 14 nm. The optimized core–shell $Fe_{45}Pt_{35}Cu_{20}$ catalyst with Pt-enriched surface exhibits 0.5 A/mg_{Pt} mass activity, which is a factor of 4 better than that of commercial Pt/C (0.13 A/mg_{Pt}). Clearly, this one-step synthesis of core-shell structure FePtCu catalyst is highly promising for ORR and other electrochemical processes.

4.2 Results

The XRD spectra of $(FePt)_{100-x}Cu_x$ (x=10, 20, 30 and 40) nanoparticles with standard $L1_0$ FePt/FePtCu XRD spectra as reference are shown in Fig. 4.2a. The four samples show very similar peaks, which are assigned to (001), (110), (111), (200), (002), (201), (112), (220), and (202) peaks of *fct*–FePtCu (PDF No. 26–528) based on the XRD analysis. The occurrence of the characteristic $L1_0$ superlattice peaks at around 24.1° (001) and 32.9° (110) indicates that the Cu additive can efficiently promote the phase transformation at these concentrations. In order to investigate the Cu doping effect on the FePtCu ordering, we carried out refined XRD analysis shown in Fig. 4.2b.

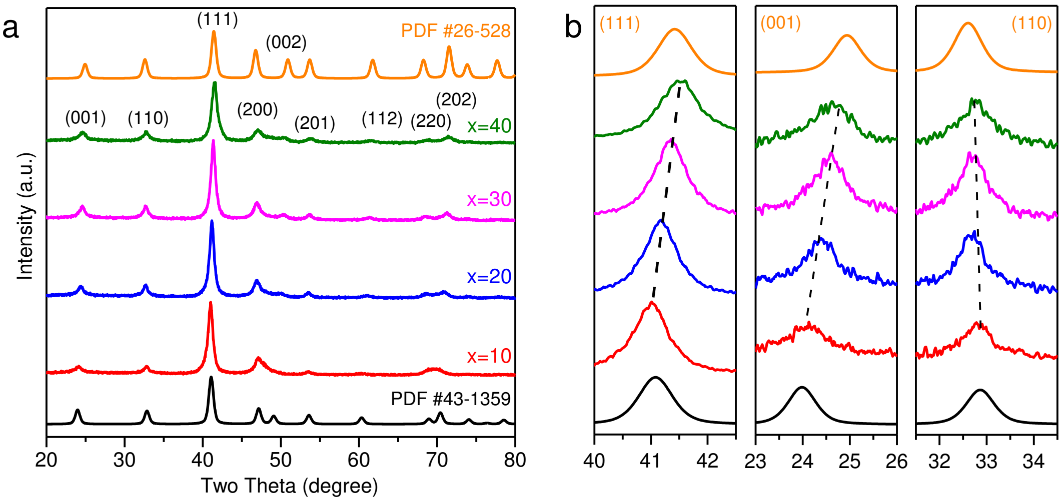

Fig. 4.2 a) XRD spectra of the as-synthesized $(FePt)_{100-x}Cu_x$ (x=10, 20, 30 and 40) Nanoparticles. b) Enlarged sections of the (001), (110) and (111) peaks for the 2θ range of 23°~26°, 31°~35°, and 40°~43°.

For $Fe_{45}Pt_{45}Cu_{10}$ with low Cu content, the (001), (110), and (111) peaks match with *fct*–FePt (PDF No. 43–1359). With an increasing Cu concentration, the (001) and (111) peaks shift to higher 2θ degree, whereas the (110) peaks shift to lower 2θ degree, gradually approaching the *fct*–FePtCu (PDF No. 26–528) peaks. It is well known that an expansion of the FePt *a*–axis is accompanied with a contraction of the FePt *c*–axis along with the additive content increase, which promotes the $L1_0$ ordering process.[160] Besides, another $L1_0$ superlattice (002) peak gradually arises when the Cu concentration is higher than 20%. Based on the above XRD analysis, we conclude that the *fct*–FePtCu alloy nanoparticles are synthesized as a result and that the Cu alloy effect is the driving force for this ordering transformation.

Fig. 4.3a shows the CV curves for FePtCu and Pt/C catalysts in O_2–saturated electrolyte at 50 mV/s. Characteristic adsorption/desorption processes of under–potentially deposited H_{upd} at low potential of –0.05~0.30 V and hydroxyl layer on the catalyst surface at potential of 0.60~0.70 V were clearly seen. The catalytic activity of $Fe_{40}Pt_{40}Cu_{20}$ Nanoparticles is apparently higher than that of the other FePtCu compositions due to its higher OH_{ad} reduction current peak at ~0.7 V. Fig. 4.3b shows the ORR polarization curves for the four catalysts and Pt/C by using rotation disk electrode linear voltammetry. $Fe_{40}Pt_{40}Cu_{20}$ Nanoparticles show the highest onset potential among the four catalysts demonstrating that the core–shell structure FePtCu enhances the catalytic performance of FePtCu.

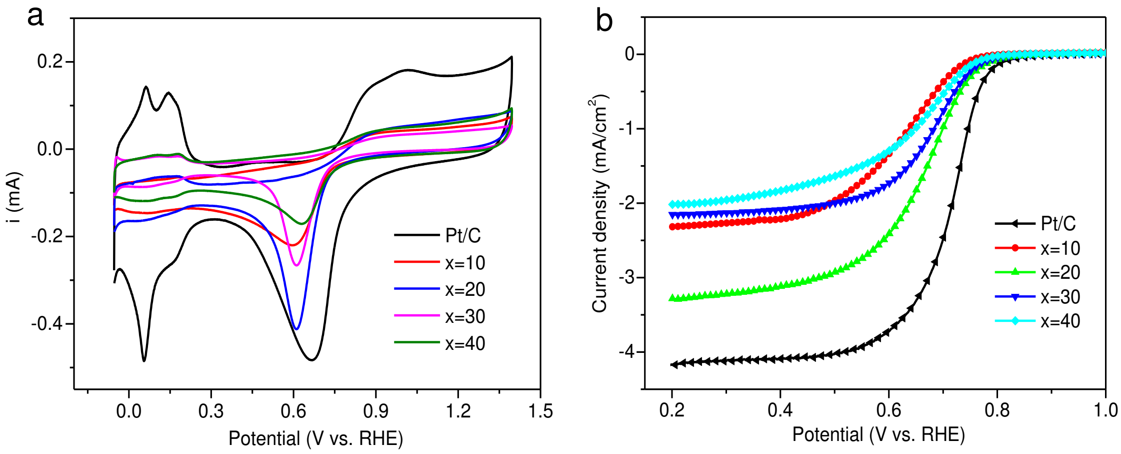

Fig. 4.3 **a**) CV curves of $(FePt)_{100-x}Cu_x$ and commercial Pt/C at 50 mV/s in O_2 saturated 0.5 M H_2SO_4 electrolyte, and (b) ORR polarization curves.

To characterize the morphology and elemental distribution of FePtCu with various Cu doping content, we carried out electron microscope analysis, including SEM, STEM and

STEM–EELS/EDX, as shown in Fig. 4.4. With 10% Cu doping, the FePtCu particles show sphere morphology and diameter arranges from 11.1 nm to 24.2 nm, mean diameter of 16.1 nm. STEM–EDXs mapping shows that Fe, Cu, and Pt atoms are uniformly distributed through these particles, demonstrating solid solution alloy structure of $Fe_{45}Pt_{45}Cu_{10}$. When the share of Cu increases to 20%, the particles grow bigger with particle diameter ranges from 17.8 to 43.1 nm (mean diameter 32.7 nm). Meanwhile, elemental mapping images show that core–shell structure of CuFePt formed for $Fe_{40}Pt_{40}Cu_{20}$ nanoparticles, with Cu–rich core and FePt–rich shell. When the Cu composition increases to 40%, the $Fe_{30}Pt_{30}Cu_{40}$ exhibited predominantly a sintered morphology as shown in Fig. 4.4e, f). This can be explained that Cu doping lowers the melting temperature of FePtCu, and increase the atomic diffusivity, thereby enhancing the kinetics of ordering.[173] Elemental mapping images show that $Fe_{30}Pt_{30}Cu_{40}$ particles are solid solution alloy structure.

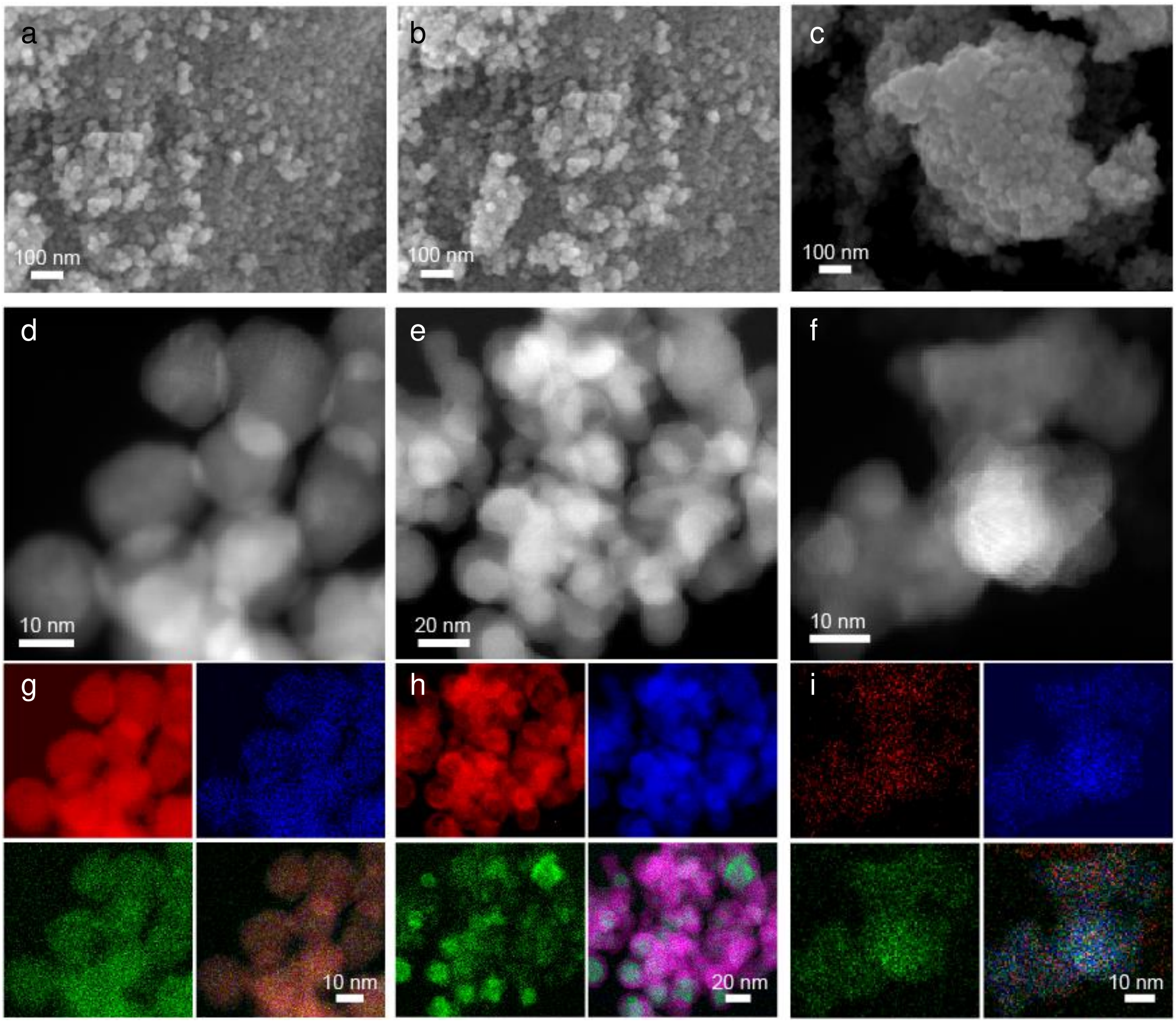

Fig. 4.4. a~c) SEM, low–magnification images of $Fe_{45}Pt_{45}Cu_{10}$, $Fe_{40}Pt_{40}Cu_{20}$ and $Fe_{30}Pt_{30}Cu_{40}$, respectively. d~f) High–resolution HAADF images of $Fe_{45}Pt_{45}Cu_{10}$, $Fe_{40}Pt_{40}Cu_{20}$ and $Fe_{30}Pt_{30}Cu_{40}$, respectively. g~i) STEM-EELS maps of Fe (red), Cu (blue) and Pt(green) edges for $Fe_{45}Pt_{45}Cu_{10}$, $Fe_{40}Pt_{40}Cu_{20}$ and $Fe_{30}Pt_{30}Cu_{40}$, respectively.

From above analysis, we can see that the Cu content has strong effects on FePtCu morphology, size, elemental distribution in our one–pot synthesis method, and thus catalysis performance for ORR. Motivated by studying Fe/Pt composition effect on FePtCu structure and searching for more efficient catalyst, we fix the optimized Cu content of 20% and adjust the Fe and Pt ratio as Fe$_x$Pt$_{80–x}$Cu$_{20}$. The XRD spectra (Fig. 4.5a) of FePtCu Nanoparticles synthesized in various Fe/Pt ratios and fixed to 20% Cu content resemble those of (FePt)$_{100–x}$Cu$_x$ nanoparticles and with L1$_0$ phase. The Fe$_x$Pt$_{80–x}$Cu$_{20}$ peaks are between L1$_0$–FePt and L1$_0$–FePtCu, which can be more clearly observed in the (110), (001), and (111) peaks shown in 4.5b. When the Fe content is decreased from 50% to 30%, the (001)/(110) peaks of as–synthesized Fe$_x$Pt$_{80–x}$Cu$_{20}$ nanoparticles are barely shifted, and the (111) peaks are slightly shifted toward lower diffraction angle, which means that the lattice parameter increases. This is reasonable due to a larger size of Pt atoms (1.77 Å) than Fe (1.56 Å), as shown in Table 3.2.

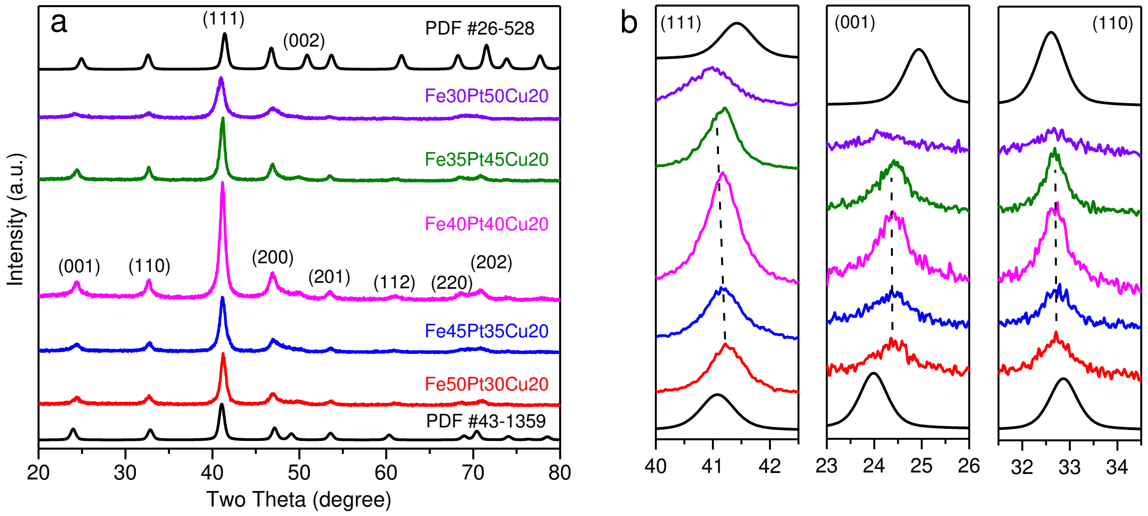

Fig. 4.5 a) XRD spectra of the as-synthesized Fe$_x$Pt$_{80–x}$Cu$_{20}$ (x=30, 35, 40, 45 and 50) nanoparticles. b) Enlarged sections of the (001), (110) and (111) peaks for the 2θ range of 23º~26º, 31º~35º, and 40º~43º.

Besides, the FePtCu nanoparticles with various atom ratios have different ordering degree and surface structure due to the composition effect, which is also important for catalysis. Fig. 4.6a shows the ORR polarization curves of $Fe_xPt_{80-x}Cu_{20}$ nanoparticles, in which the $E_{1/2}$ values of the alloys correspond to the following order: $Fe_{45}Pt_{35}Cu_{20}$ > Pt/C ≥ $Fe_{40}Pt_{40}Cu_{20}$ > $Fe_{30}Pt_{50}Cu_{20}$ ≥ $Fe_{50}Pt_{30}Cu_{20}$ > $Fe_{35}Pt_{45}Cu_{20}$, with values of 0.71, 0.70, 0.70, 0.66, 0.66, and 0.64 V (vs. RHE), respectively. Moreover, the onset potential of $Fe_{45}Pt_{35}Cu_{20}$ was reduced by nearly 40 mV compared to that of Pt/C. Fig. 4.6b shows the mass activities measured at half wave potential. The mass activity shows the same sequence as the $E_{1/2}$ values and $Fe_{35}Pt_{45}Cu_{20}$ nanoparticles exhibited comparable mass activity with a value of 0.50 A/mg_{Pt}, which is 4 times higher than that of commercial Pt/C. Furthermore, the as–synthesized $Fe_{45}Pt_{35}Cu_{20}$ catalyst is superior to the commercial Pt/C and can save 74.3% of Pt at a potential of 0.7 V. We measure the ORR polarization curves of $Fe_{45}Pt_{35}Cu_{20}$ at different rotation speeds, i.e., 400, 900 and 1600 rpm, respectively, as shown in Fig. 4.6c. Then we can calculate electron transfer number (*n*) according to Koutecky–Levich equation. Fig. 4.6d shows the j^{-1} versus $\omega^{1/2}$ plots at 0.6 V, 0.7 V and 0.8 V for $Fe_{45}Pt_{35}Cu_{20}$ nanoparticles. The number of electrons calculated from the slop is 3.6, which demonstrates that it is mainly four-electron transfer process of FePtCu. The stability of the $Fe_{45}Pt_{35}Cu_{20}/C$ catalyst for ORR was tested between 0.6 and 1.0 V in N_2–saturated 0.5 M H_2SO_4 with a scan rate of 100 mV/s.

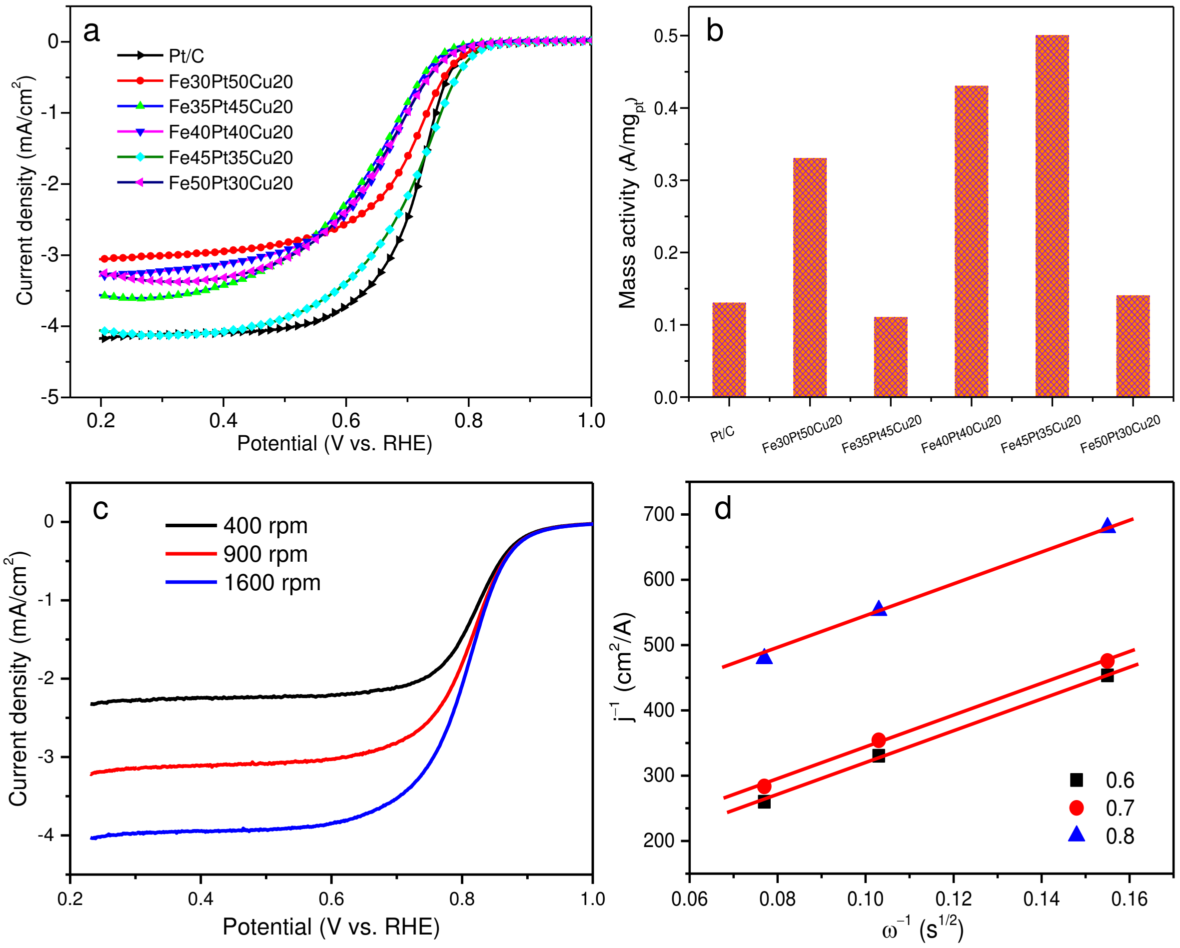

Fig. 4.6 a) ORR polarization curves of $Fe_xPt_{80-x}Cu_{20}$ and commercial Pt/C. b) ORR mass activities and specific activities, accordingly. c) Rotation-rate dependent current–potential curves for $Fe_{45}Pt_{35}Cu_{20.}$ d) The calculated Koutecky-Levich cures at 0.6, 0.7 and 0.8 V for $Fe_{45}Pt_{35}Cu_{20.}$

The CV and ORR polarization curves of the $Fe_{45}Pt_{35}Cu_{20}$ nanoparticles before and after 1000 cycles show a slight 3.0% decay of the current density at the half–wave potential, demonstrating sufficient stability, as shown in Fig. 4.7a, b. While, the benchmark Pt/C catalyst durability test under the same measure conditions are shown in Fig. 4.7c, d. The current density of Pt/C decays 34.2% after 1000 cycles. Previously reported binary *fct*–FePt that decays 14.0% under the same electrochemical conditions.[96] These results show that our ternary *fct*–FePtCu are with enhanced durability than both commercial Pt/C and binary *fct*–FePt.

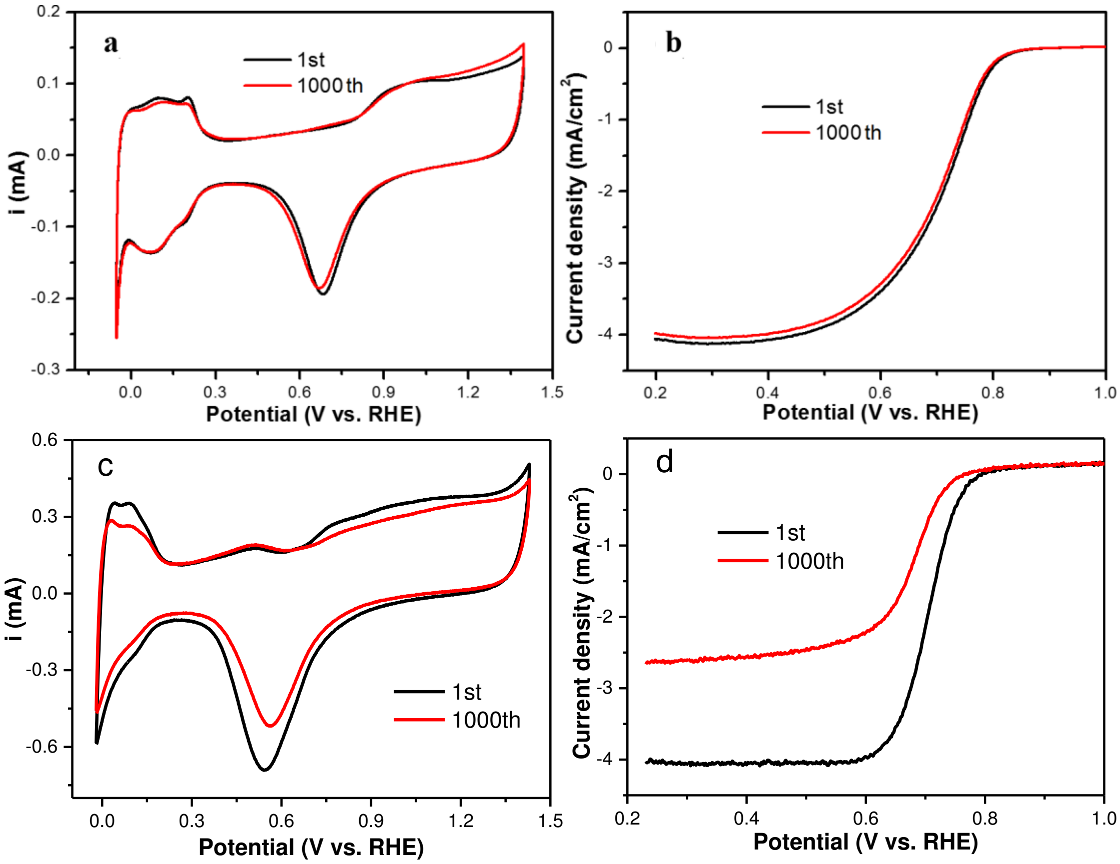

Fig 4.7. Cycling–stability tests of $Fe_{45}Pt_{35}Cu_{20}$ and Pt/C. a~b) The CV and polarization curves of $Fe_{45}Pt_{35}Cu_{20}$ before and after 1000 electrochemical cycles in N_2 saturated 0.5 M H_2SO_4 electrolyte. c~d) The CV and polarization curves of Pt/C before and after 1000 electrochemical cycles.

To characterize the composition and structure effects on the catalytic performance, as-fabricated $Fe_{45}Pt_{35}Cu_{20}$ nanoparticles were investigated by HAADF-STEM and EDXs mapping analysis as shown in Fig. 4.8. The diameter of the nanoparticles range from 17.8 to 37.9 nm and the mean diameter is 28.7 nm. The elemental mapping provides clear evidence of the core–shell structure. However, if the Fe/Pt ratio deviates too much from the optimal one, it results in significant change of the morphology and structure of FePtCu nanoparticles shown in Fig. 4.8a, c. The $Fe_{30}Pt_{50}Cu_{20}$ has a uniform nanoparticle size ranging from 11.1 to 24.0 nm, with a mean diameter of 16.7 nm, which is smaller compared to nanoparticles with 45% iron (Fig. 4.8b). Decreasing the Fe content to 30% results in an alloy structure, demonstrating that the Fe content is also critical for the formation of alloy and core–shell structures. For $Fe_{50}Pt_{30}Cu_{20}$, a low magnification STEM image shows that the particles were sintered with diameter ranges from 13.0 to 38.2 nm. The EELS spectrum of $Fe_{50}Pt_{30}Cu_{20}$ in Fig. 4.8c shows that it is accompanied with a partial

CuFePtCu core–shell structure with a Cu–rich core and a FePt–rich shell. Increasing the Fe content from 45% to 50% makes the particles partial core–shell caused by sintering induced atom diffusion. Thus, we may conclude that the better catalytic performance of $Fe_{45}Pt_{35}Cu_{20}$ is due to the composition optimization of a well–crystallized core–shell structure.

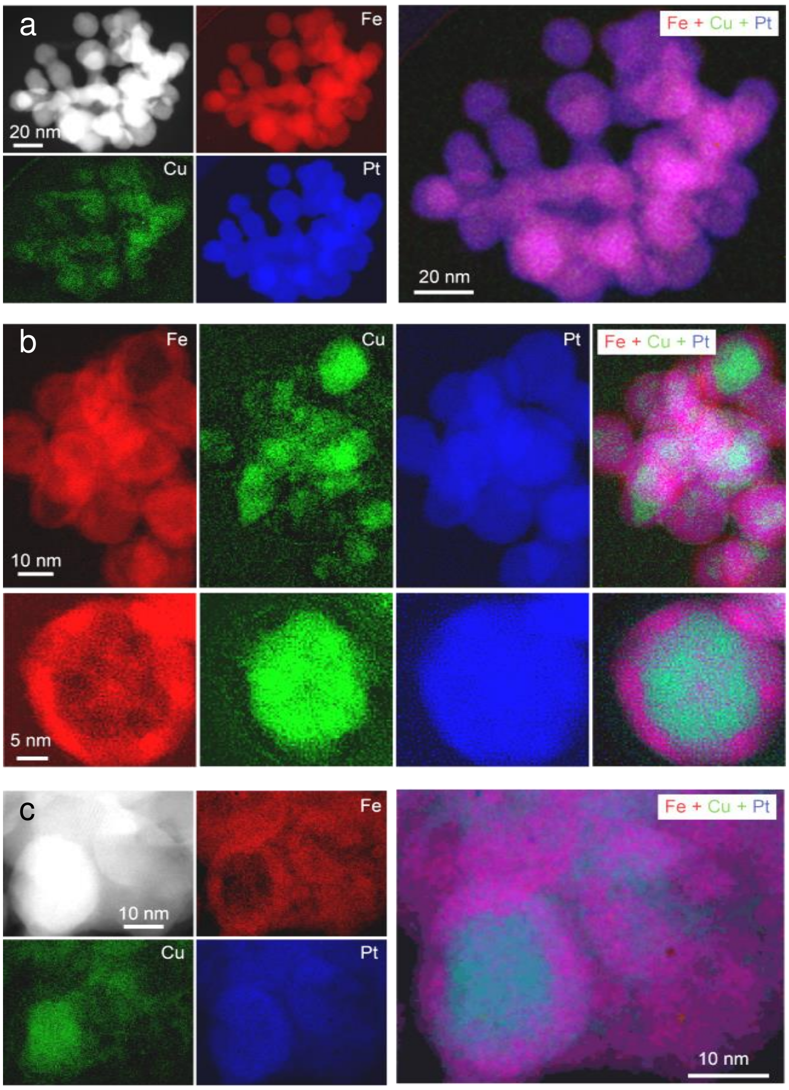

Fig 4.8. a) HAADF-STEM image of $Fe_{30}Pt_{50}Cu_{20}$ and EELS elemental mapping of Fe (red), Cu (green), Pt (blue) and their overlap. b) Elemental distribution analysis of $Fe_{45}Pt_{35}Cu_{20}$. c) Elemental distribution analysis of $Fe_{50}Pt_{30}Cu_{20}$.

Fig. 4.9 shows an atomic resolution image and elemental distribution of a surface region of the $Fe_{45}Pt_{35}Cu_{20}$ core–shell catalyst. The surface of $Fe_{45}Pt_{35}Cu_{20}$ indicates an enrichment of platinum at its surface. Fig. 4.9d is an enlarged image of the selected area marked by a blue rectangle of Fig. 4.9a. The STEM electron beam direction is parallel to the [101] crystal direction of $L1_0$–FePtCu. Along this crystal orientation, the Fe/Cu and Pt atoms are located in the same atomic column and in alternately distributed [101] direction. An atomic structure model of the tetragonal phase of FePtCu along the [101] projection and a simulated HAADF image were superimposed on the HAADF image. The surface termination of the particles is parallel to the (010) crystal plane of $L1_0$–FePtCu. Fig. 4.9b~c shows the EELS elemental mapping of Fe, Cu and Pt and their overlay at atomic scale, in which the atom columns of each of the Fe and Pt elements are clearly resolved. Furthermore, comparing the intensity elemental mapping results reveals that there is a Pt enrichment layer (approximately 4~5 atomic layers) at the surface of core–shell structure, as can be seen from Fig. 4.9c. Fig. 4.9e shows the EELS line scan spectrum imaging of Fe K, Pt L, and Cu K of the arrow marked area in a region of Fig. 4.9c, which shows an obvious platinum enrichment at the surface with 5 atom layers. To carefully check these waves, we can see that the Fe, Cu, and Pt atoms are located in the same atom columns. This platinum enrichment finding is also confirmed by the EELS elemental mapping of other particles. Pt segregation at crystal surfaces have been reported previously for Pt-based alloys.[174] Preferential elemental segregation at the surface can result from differences in surface energy and/or atomic radius between the metal elements. An element with lower surface energy is more likely to segregate to the surface to minimize the overall Gibbs energy of a particle.[174] Thus, larger Pt atoms that diffuse to the outermost layer are energetically favored, thus releasing the elastic energy/strain in the antiparticles. The core–shell structure $Fe_{45}Pt_{35}Cu_{20}$ with 4~5 layers Pt surface not only exposes the stable $L1_0$–FePtCu shell with Pt enrichment surface to oxygen that is more robust than a Pt monolayer or alloy surfaces, but also offers desired core-shell interactions and alloy effects for optimal catalysis.

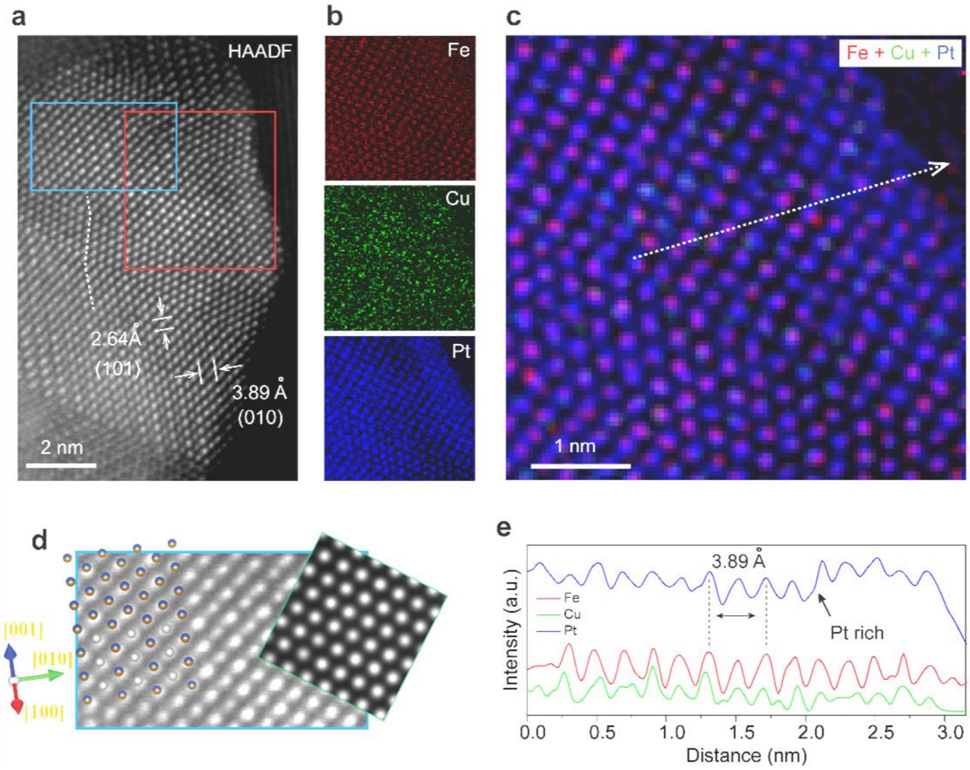

Fig. 4.9. Elemental distribution and surface analysis of $Fe_{45}Pt_{35}Cu_{20}$: a) Atomic resolution HAADF image of a surface region of the $Fe_{45}Pt_{35}Cu_{20}$ core–shell catalyst. b) EELS mapping of red square region marked in Fig 4.9a, showing the Fe, Cu and Pt atomic distributions. c) Overlaid of the atomic maps of Fig. 4.9b. d) An atomic model of $L1_0$–FePtCu and a simulated HAADF image of $L1_0$–FePtCu along [101] projection. (e) Atomically resolved elemental composition profiles along [010] direction (shown in Fig. 4.9c) using EELS signal of Fe K (red), Cu K (green), Pt L (blue) edges, respectively. In this analyzed region, the surface termination is parallel to the (010) crystal plane of $L1_0$–FePtCu. At the particle surface, the Pt concentration increases indicating enrichment of Pt.

In order to have other proofs of the phase transformation, we also characterized the magnetic properties of $Fe_xPt_{80-x}Cu_{20}$ nanoparticles. As can be seen in Fig. 4.10, the $Fe_{30}Pt_{50}Cu_{20}$ nanoparticles magnetic behavior exhibits a hysteresis with a two–phase behavior, which means that a partially ordered FePtCu phase was formed in this composition with a coercivity of 0.9 kOe. When the Fe contents was increased to 35%, the coercivity of the nanoparticles increased to 4.8 kOe indicating that the nanoparticles contain a hard magnetic FePtCu phase. Further increase of the Fe contents yielded 2.1 kOe, 3.6 kOe, and 3.1 kOe coercivity for $Fe_{40}Pt_{40}Cu_{20}$, $Fe_{45}Pt_{35}Cu_{20}$, and $Fe_{50}Pt_{30}Cu_{20}$ nanoparticles, respectively. Thus, the as–synthesized FePtCu nanoparticles are ferromagnetic, due to the Cu–alloying effect and the phase transition of FePt.

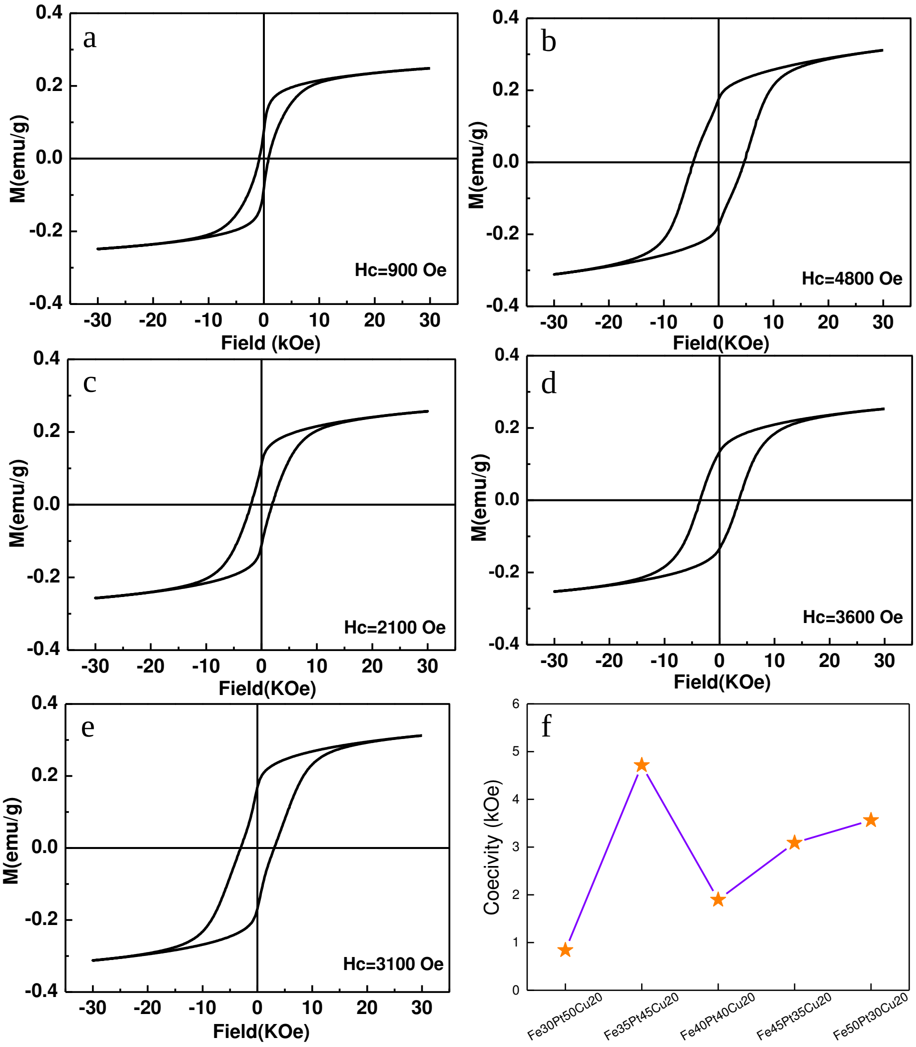

Fig 4.10 Room tempertaure a) hysteresis loops, and b) coercivity of the as-synthesized nanoparticles: $Fe_{30}Pt_{50}Cu_{20}$, $Fe_{35}Pt_{45}Cu_{20}$, $Fe_{40}Pt_{40}Cu_{20}$, $Fe_{45}Pt_{35}Cu_{20}$, and $Fe_{50}Pt_{30}Cu_{20}$.

4.3 Conclusion

In conclusion, a polyol solvent method was employed to prepare composition adjustable ordered $L1_0$–FePtCu nanoparticles as active and stable ORR catalyst. The Cu alloying effect is the driving force of the $L1_0$–FePt ordering, which is effective up to a Cu content of 40%. High resolution STEM techniques and X-ray diffraction provided insight into the composition effects on their ordering, core–shell/alloy structures, morphology and ORR performance. As shown above, the particle size increases with the Fe or Cu ratio, and the particles are sintered for Fe (50%) and Cu (> 20%). The Fe and Cu content is critical to form a Cu/FePtCu core/shell structure, for Cu content with 20% ratio and Fe with more than 40%. Optimized $Fe_{45}Pt_{35}Cu_{20}$ nanoparticles with core–shell and a 4~5 atomic layer Pt-rich surface structure show better ORR catalysis performance than commercial Pt/C, or 4 times better mass activity and also good stability. The results demonstrate a new way to improve Pt catalysis for ORR and it will help to develop $L1_0$–FePt based core–shell nanoparticles for ORR for fuel cells and other electrochemical reactions. Our work provided a proof of a concept that high performance *fct*–FePt ORR catalyst are not only ordered, but also have a core–shell structure.

Chapter 5

Evolution of FePtCu catalytic nanoparticles at atomic-scale

5.1 Introduction

In the last chapter, we demonstrated a one–pot method to realize core–shell Cu/FePt nanoparticles with ordered structure, leading to a highly enhanced catalytic activity. This type of synthesis constitutes a good strategy to improve efficiency of a chemical reaction, whereby reactants are subjected to successive multi-step chemical reactions in just one reactor. A one–pot procedure can thus minimize chemical waste, save time, and simplify practical aspects. Various Pt-based catalyst have also been synthesized by one–pot method, although the reaction mechanism behind is not sufficient clear.

Taking FePtCu system as a model system, we present an atomic scale (quasi) in-situ study of the growth mechanism of one-pot synthesized FePtCu nano-catalyst using aberration-corrected scanning TEM coupled with spatial elemental analysis by EELS/EDXS. By tracking both morphology and composition evolution during the synthesis, we reveal the growth mechanisms of FePtCu nano-catalyst at different growth stages. The precursor starts with Cu cluster and undergoes an anisotropic growth forming CuFePt core-shell with branched shape, and then grows in CuFePt core-shell hexapod. Then, suface diffusion dominated growth leading the deposition of Fe and Pt into the concave surface forming core-shell CuFePt octahedron. Finally, bulk atom diffusion dominated growth formed evolves the nanoparticle into solid solution FePtCu alloy. We correlate this morphology and composition evolution with catalytic activity and stability. Our finding provides a comprehensive understanding of the "growth cycle" of FePtCu nano-catalyst and aids rational synthesis of low–Pt catalysts for efficient electrochemical energy conversion.

5.2 Results

5.2.1 Reaction time series

Low-magnification TEM imaging was used to characterize their morphology, size and uniformity for FePtCu nanoparticles acquired at 20 minutes, as shown in Fig. 5.1a. We can see that FePtCu particles synthesized at 20 min are uniform in size and with branched shape morphology. The inset is an AADF-STEM image of a single nanoparticle, which shows obvious six branches shape, namely, hexapod shape. Diameter analysis was carried out using ImagJ software, and 20 min FePtCu particles are about 18.6 nm in diameter, as shown in Fig. 5.1b. High-magnification TEM imaging was used to characterize the microstructure of 20 min FePtCu, as shown in Fig. 5.1c. Correlated with analysis of its FFT image of Fig. 5.1d, we can see that a zone axis of [1–10] direction and a cubic structure of FePtCu were obtained. Besides, we can index its lattice planes of 111, 220 and 002 families, from which it shows that the six branches of 20 min FePtCu grow along *z*–axis and equivalent directions. To investigate the crystalline and surface structure, which is critical for ORR due to it is a hetero-catalysis reaction and only surface atoms directly take part in the catalysis reactions, special attention has been paid on the surface of FePtCu particles. Fig. 5.1e is an enlarged image of HRTEM, indicating the cubic lattice and a particle with high crystalline face index exposure. The same analysis protocol has been applied to FePtCu acquired at 40 min, 1 h and 2 h reaction time in the following.

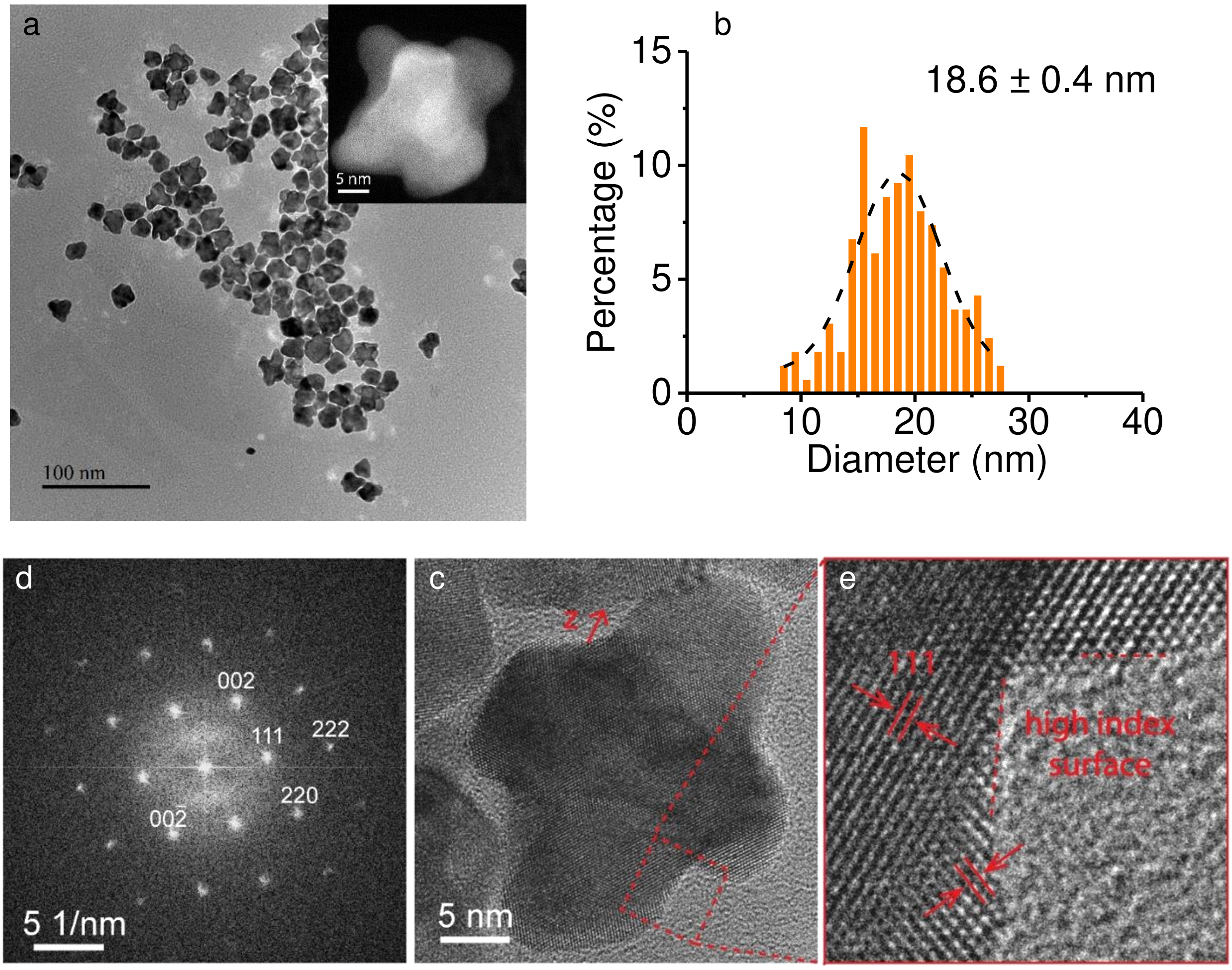

Fig. 5.1 a) Low-magnification TEM image of FePtCu synthesized at 20 min, (The inset is a HAADF-STEM image of a single nanoparticle). b) Diameter analysis of as-prepared FePtCu of 20 min. d) High-resolution TEM image of FePtCu synthesized at 20 min, and c) FFT image for identification of the corresponding zone axis, as well as e) a zoom-in image as marked area of Fig. 5.1d.

Fig. 5.2a is low-magnification TEM image of FePtCu nanoparticles after 40 minutes, with the same shape of hexapod as 20 min. In this case, the size increases by 12.9%, with diameter of 21.0 nm as shown in Fig. 5.2b. It means that anisotropic growth dominates the particle growth before 40 min. Fig. 5.2c is a high-resolution HAADF-STEM image of a single particle acquired at 40 min. Chemical ordering is observed along the *z*–axis direction, as can be clearly seen from the magnified image of the red underlined part (Fig. 5.2e) and FFT image (Fig. 5.2d). This atomic resolved image shows strong evidence of chemical ordering structure and anisotropic growth along *z*–axis. It also demonstrates that a slightly bulk atom diffusion occurs from 20 min to 40 min, which induced the phase transformation from cubic hexapod particle to partially ordering hexapod. Fig. 5.2d still shows the particle exposures with high crystalline index surface.

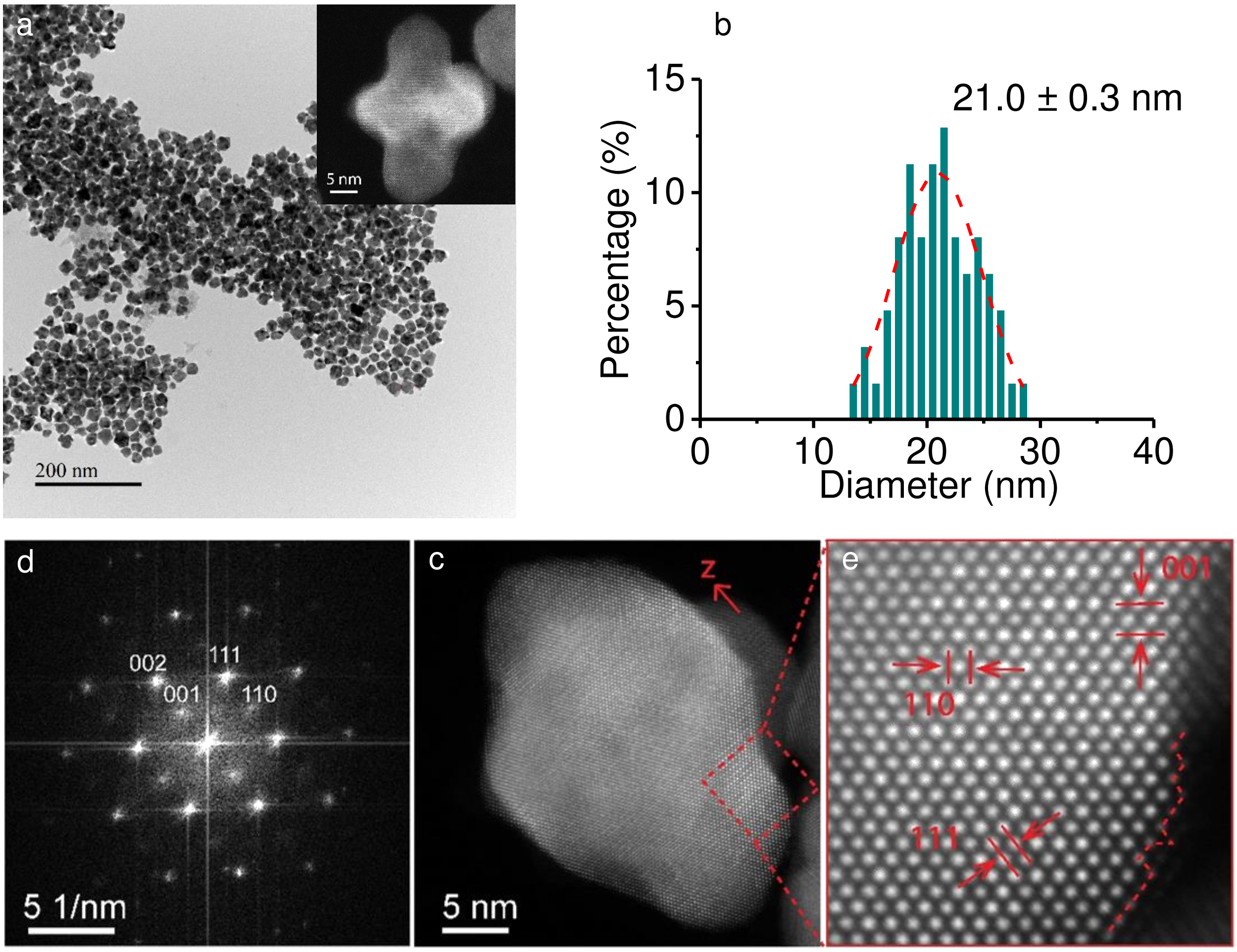

Fig. 5.2 a) Low-magnification TEM image of FePtCu synthesized at 40 min, (The inset is a HAADF-STEM image of a single nanoparticle). b) Diameter analysis of as-prepared FePtCu of 40 min. d) High-resolution TEM image of FePtCu synthesized at 40 min, and c) its FFT image, as well as e) a zoom-in image as marked area of Fig. 5.2d.

Fig. 5.3a is a low-magnification TEM image of FePtCu nanoparticles acquired at 1 h, demonstrating a truncated-octahedron shape. While its size is about 15.8 nm with narrower size distribution as shown in Fig. 5.3b. The size decrease, as compared to 40 min, can be explained by that TEM imaging is a 2 dimension projection of 3 dimension objects. There are some empty space of branched shape particles, which means the calculated diameter of whom based on TEM image should be larger than a solid particle with the same amount of atoms. The shape evolution from branch shape into polyhedron shape indicates violent surface atom diffusion occurs from particle branches to its empty space during this period, which also contributes to the size decrease of TEM results. Fig. 5.3c is a high-resolution HAADF-STEM image of a single particle acquired at 1 h, slightly ordering is observed along the *z*–axis direction, as can be seen from its zoom-in image (Fig. 5.3e) and FFT image (Fig. 5.3d). By analyzing the high-resolution TEM and HAADF image, it show that 1 h FePtCu particles are mainly truncated-octahedron surrounded by 111/110 surfaces. As compared between 40 min and 1 h particles, obvious morphology evolution from branch shape to truncated-octahedron shape takes place, along with particle size, however the associated microstructure show negligible difference.

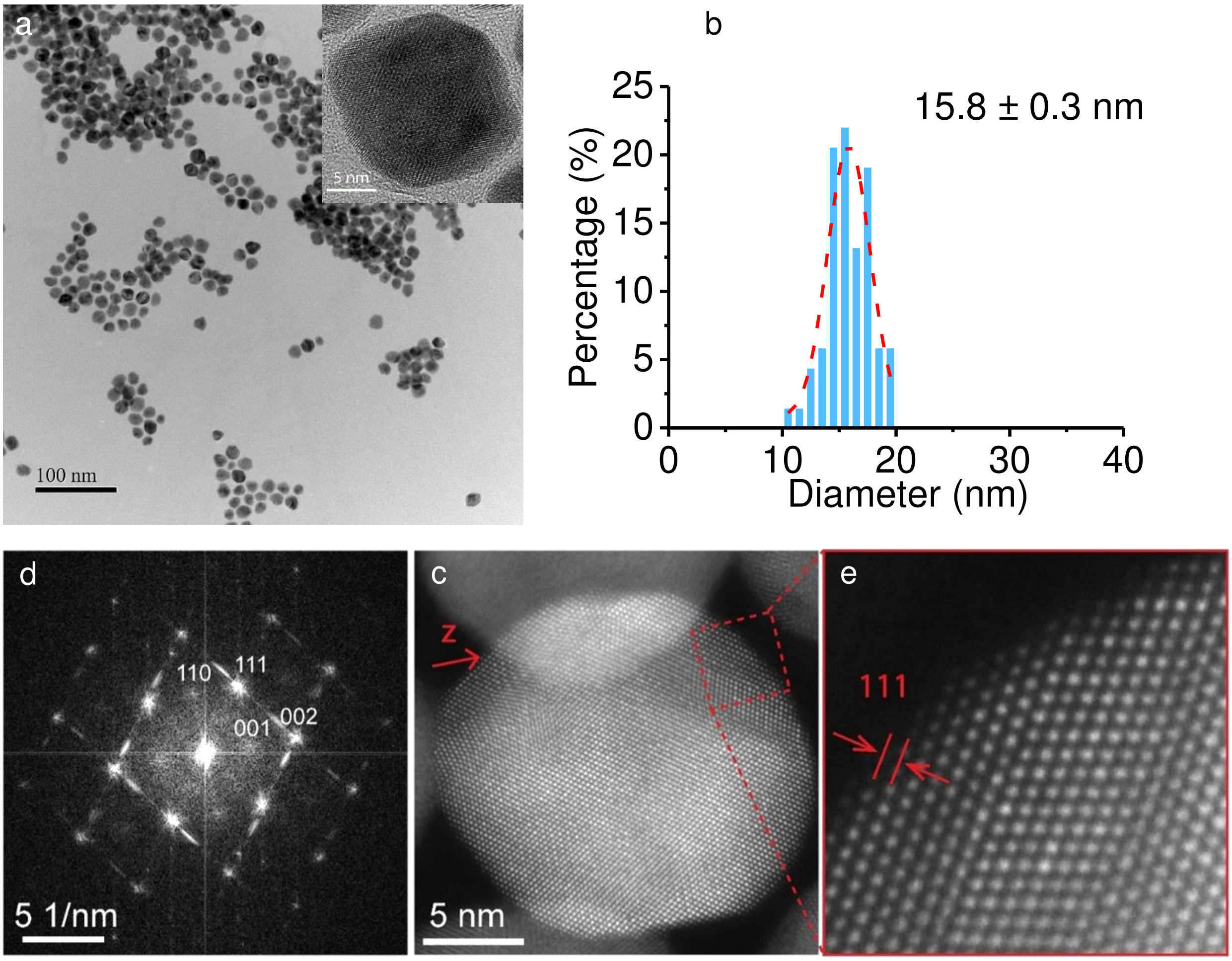

Fig. 5.3 a) Low-magnification TEM image of FePtCu synthesized at 1 h, (The inset is a HAADF-STEM image of a single nanoparticle). b) Diameter analysis of as-prepared FePtCu of 1 h. d) High-resolution TEM image of FePtCu synthesized at 1 h, and c) its FFT image, as well as e) a zoom-in image as marked area of Fig. 5.3d.

Fig. 5.4a is a low-magnification TEM image of FePtCu nanoparticles acquired at 2 h, demonstrating nearly sphere shape, with larger size and become uneven as compared to 1 h particles. They are about 19.7 nm based on the diameter analysis as shown in Fig. 5.4b.

Fig. 5.4c is a high-resolution HAADF–STEM image of a single particle acquired at 2 h. Chemical ordering is clearly seen from the magnified area (Fig. 5.4e) and corresponding FFT spectrum (Fig. 5.4d). After 2h, FePtCu nanoparticles are mainly limited by 111 surfaces.

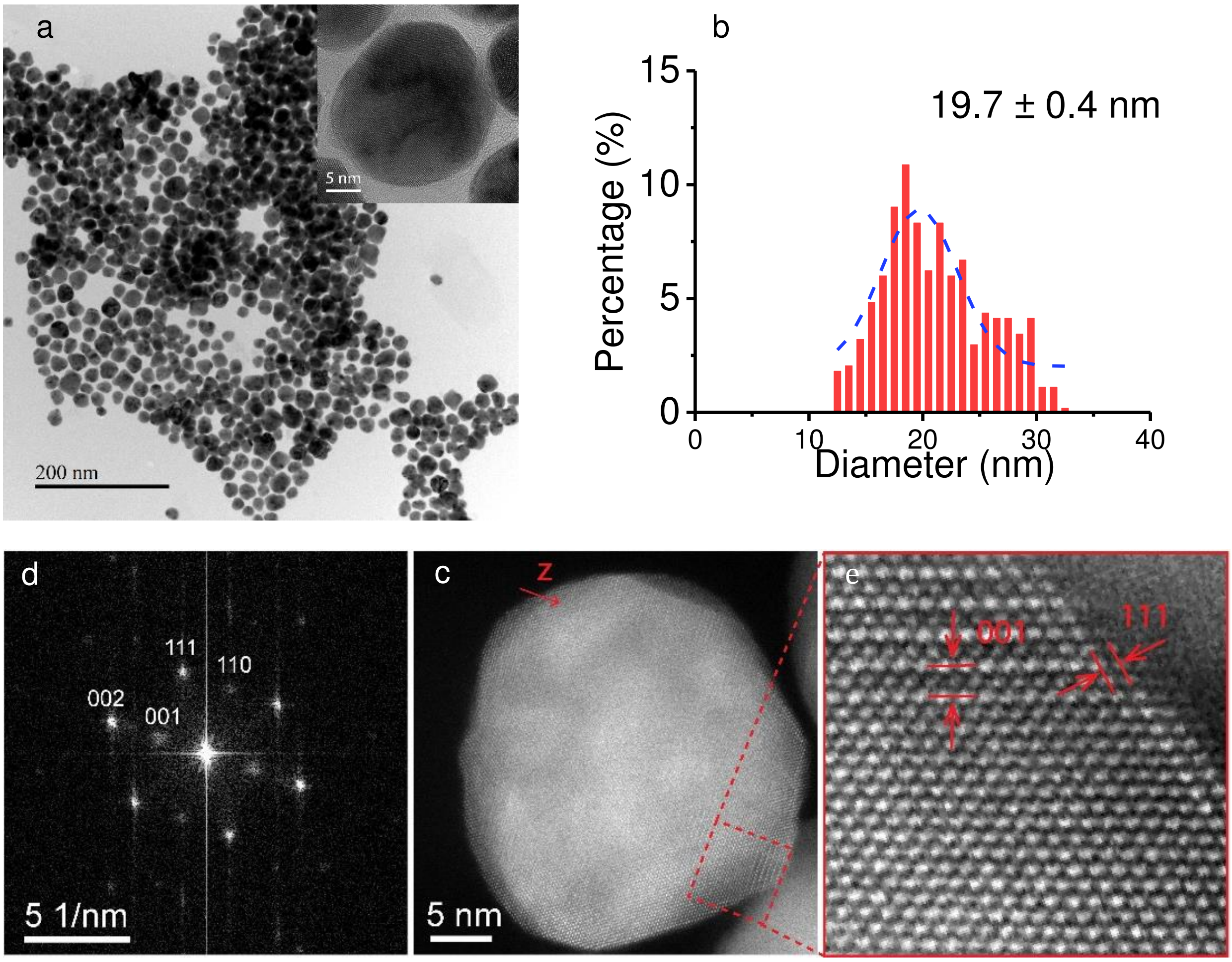

Fig. 5.4 a) Low-magnification TEM image of FePtCu synthesized at 2 h, (The inset is a HAADF-STEM image of a single nanoparticle). b) Diameter analysis of as-prepared FePtCu of 2 h. d) High-resolution TEM image of FePtCu synthesized at 2 h, and c) Corresponding FFT, as well as e) High magnification of marked area of Fig. 5.4d showing the limiting (111) projected surfaces ad connecting steps.

In order to recover and monitor the elemental evolution of FePtCu nanoparticles taken at the various reaction stages, we carried out STEM–EELS analysis on FePtCu nanoparticles, as shown in Fig. 5.5. Fe element is with red colour, Cu element is with green colour and Pt element is with blue colour. Core–shell structure of CuFePt can be seen for 20 min samples, which are Cu–rich in core and FePt–rich in shell. EELS line profile crossing a single particle can better show the element distribution inside one particle, thus the core–shell structure. TEM analytic investigation of hexapods FePtCu indicates a fast nucleation of Cu, which grows into branched shape, acting as template for following Fe/Pt attachment on the surface/shell.

For 40 min sample, it is with the same morphology and core–shell structure as 20 min, while it is with larger size, which means crystalline growth (mainly Fe and Pt) dominate this process.

For 1 h FePtCu nanoparticles, they are with polyhedron shape and core–shell CuFePt structure. It proves that surface atom diffusion mainly dominate this process, which can also explain the size decrease from 20 min to 1 h.

For 2 h FePtCu, it is uniform FePtCu alloy, which means Cu diffused out of the core and uniformly distributed in the particles and bulk atom diffusion effect mainly dominate this period.

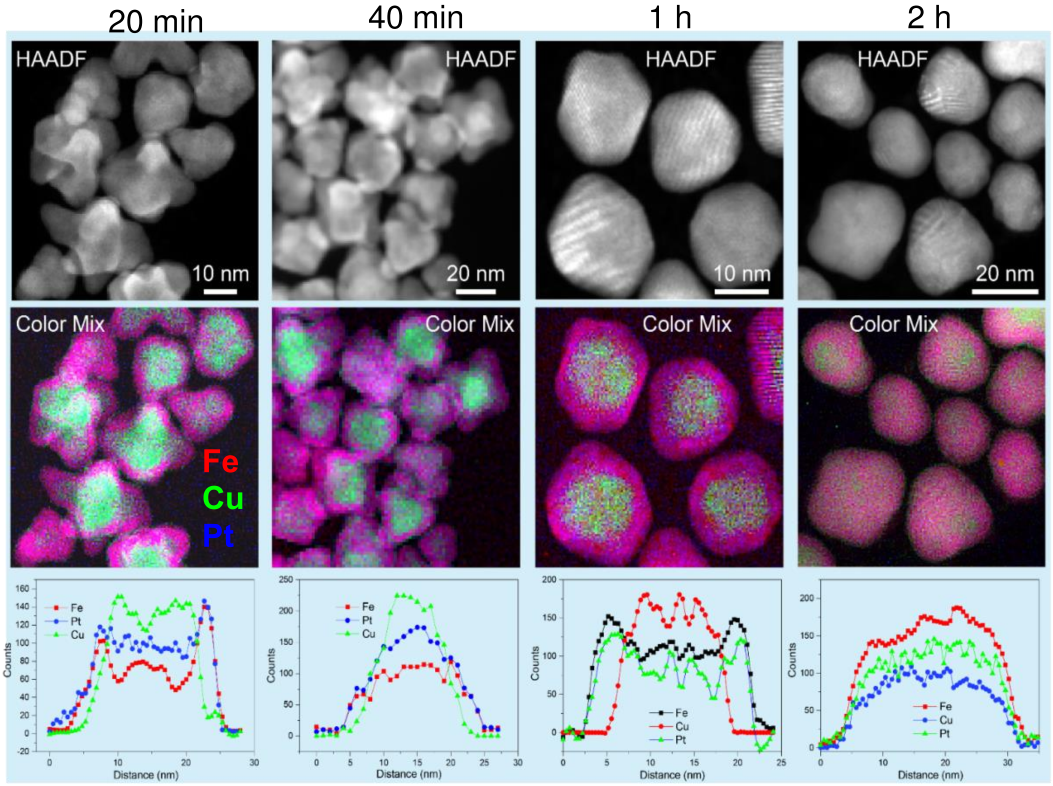

Fig. 5.5 STEM-HAADF image and elemental mapping image of FePtCu nanoparticles prepared at 20 min, 40 min, 1 h and 2 h, respectively. In the middle, it is according colour-mix image of STEM-EELS mapping, red colour is Fe, green colour is Cu and blue colour is Pt. The bottom spectra are line profiles crossing the single FePtCu nanoparticle at various reaction time.

5.2.2 Temperature behavior in the TEM

To confirm this morphology evolution and elemental diffusion, especially on Cu diffusion inside the particle, we carried out heating of CuFePt particles and characterization in TEM. The HAADF and STEM-EELS images are shown in Fig. 5.6, under thermal treatment at 300 °C and 500 °C for 1 hour, respectively. As we can see from the Fig. 5.6a, hexapods CuFePt particles keep branched shape and core–shell structure after heating at 300 °C, indicating FePtCu is stable below this temperature. For 500 °C annealing, the branches of hexapods CuFePt degrade (surface diffusion) and the particles evolve into irregular polyhedron shape, as can be seen from the HAADF image. STEM-EELS images show uniform FePtCu alloy after 500 °C annealing, demonstrating more thermostable of alloy structure than core–shell and bulk diffusion of Fe, Pt and Cu atoms.

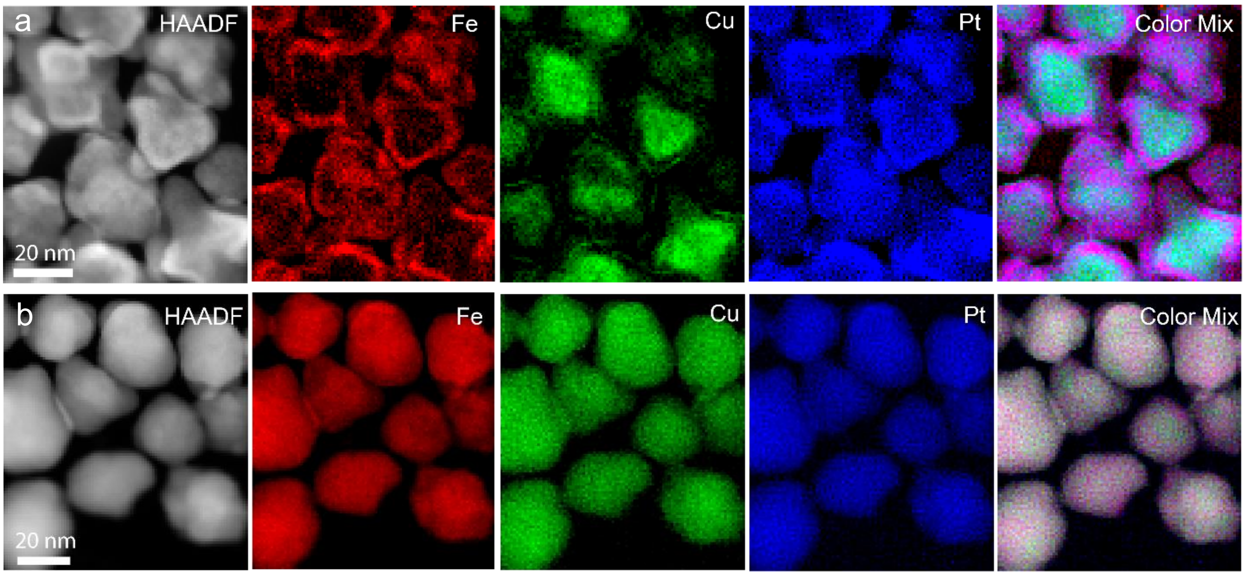

Fig. 5.6 STEM-EELS analysis of 40 min FePtCu particles, after *in-situ* annealing in microscope at a) 300 °C, and b) 500 °C for 1 hour.

The electrocatalytic properties of FePtCu particles with various morphologies and commercial Pt/C were evaluated as shown in Fig. 5.7. Cyclic voltammetry curves in N_2 saturated 0.1 M $HClO_4$ electrolyte at 50 mV/s scan rate can be seen in Fig. 5.7a. The CV curves of FePtCu show typical CV behavior as Pt/C, demonstrates characteristic electrocatalysis behavior of Platinum. Fig. 5.7b shows the linear sweep voltammetry curves of FePtCu and Pt/C, indicating activity following the order of 20 min > 1h > 2h > Pt/C. A significant positive shift of FePtCu was observed in the half–wave potential, implying a significant ORR activity increase of FePtCu. The high ORR activities in Fig. 5.7c represent a factor of 3.4~12.1 increase in Pt specific mass activity for hexpods CuFePt, 3.2~11.7 increase for truncated–octahedron CuFePt, and 2.7~5.3 increase for sphere FePtCu, as compared with Pt/C. The activity increase of hexapods CuFePt is due to its specific structure of exposed high index surface and core-shell structure. The activity increase of truncated–octahedron CuFePt is due to its core–shell structure with truncated octahedron shape. Stability is another important factor for ORR catalyst and we perform cycling measurement on as-synthesized FePtCu nanoparticles. CV and polarization curves of FePtCu and commercial Pt/C after 5000 cycling are shown in Fig. 5.7d and Fig. 5.7e. The electrochemical measurement was carried out between 0.6 and 1.0 V in O_2 saturated 0.1 M $HClO_4$ electrolyte. FePtCu show good stability and have minor difference in CV and polarization curves as compared to Pt/C, while the according mass activity following an order of 1h > 2h > 20 min > Pt/C. Their half-wave potential decrease ratios are 0.5%, 3.1%, 5.3% and 14.9 %, respectively, which demonstrate as-synthesized FePtCu particles are with both higher mass activity and durability than commercial Pt/C.

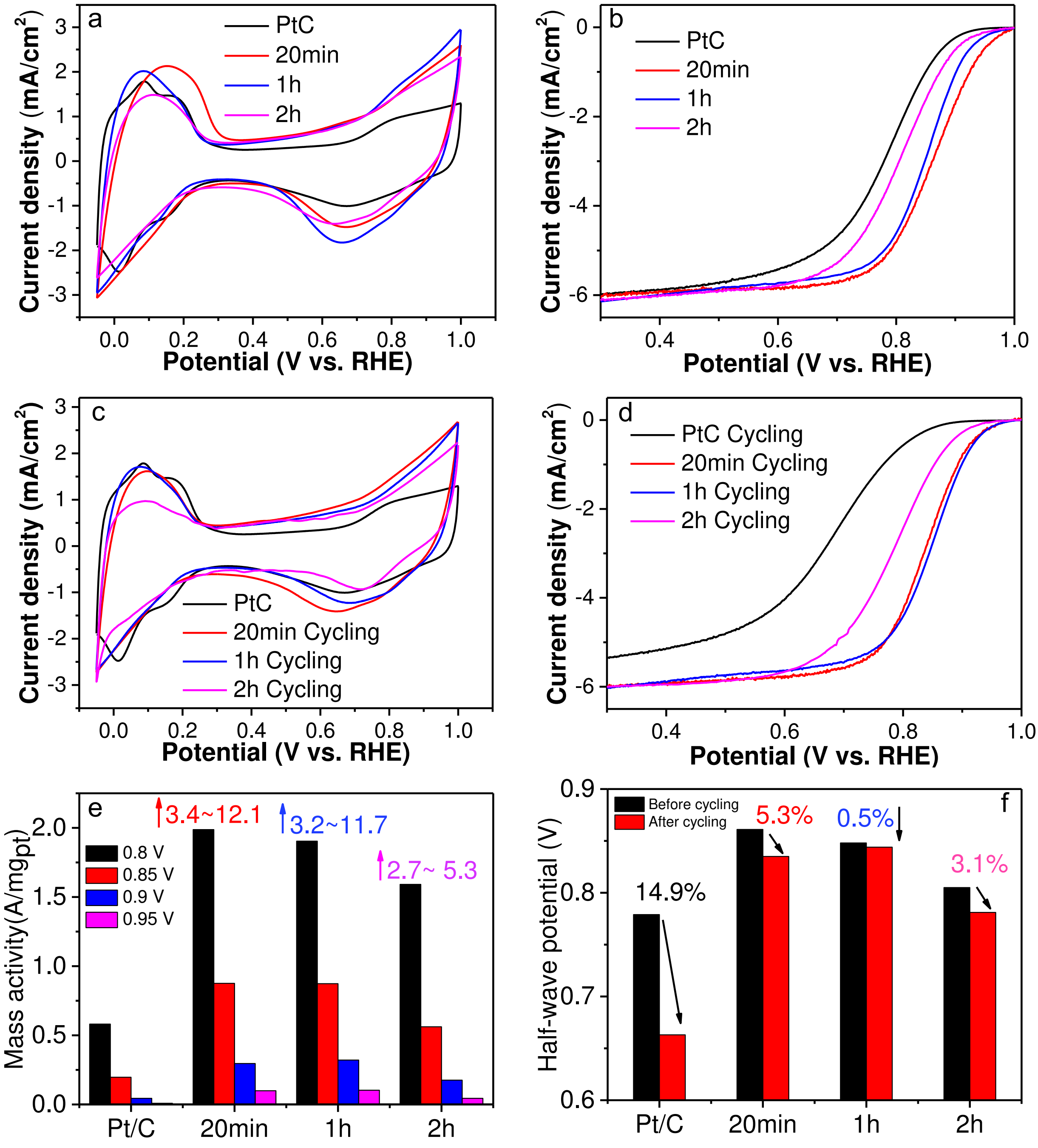

Fig. 5.7 Electrochemical performance of Pt/C and FePtCu acquired at difference reaction time. a) Cyclic voltammetry at 50 mV/s in 0.1 M $HClO_4$ electrolyte. b) ORR polarization curves at 5 mV/s and 1600 r/m rotation speed. Calculated specific mass activity at different polarization potential. Half-wave potential degradation after cycling for 5000 cycles.

5.3 Discussion

For imaging analysis, we can find that nuclei and growth of FePtCu in one–pot method follow a sequence of branch, truncated-octahedron and sphere shape at different reaction stages, as shown in Fig. 5.8. During the crystalline growth processes, anisotropic growth, surface atom diffusion and bulk atom diffusion complete each other to dominate the particle growth, results in morphology and structure evolution of FePtCu. This anisotropic growth has also been reported in solution synthesis of NiPt.[175] And the morphology evolution of NiPt from branched shape into truncated octahedron shape under thermal treatment below 300 °C.[70] Further increase the annealing temperature to 500 °C, nearly sphere shape of NiPt has been obtained.

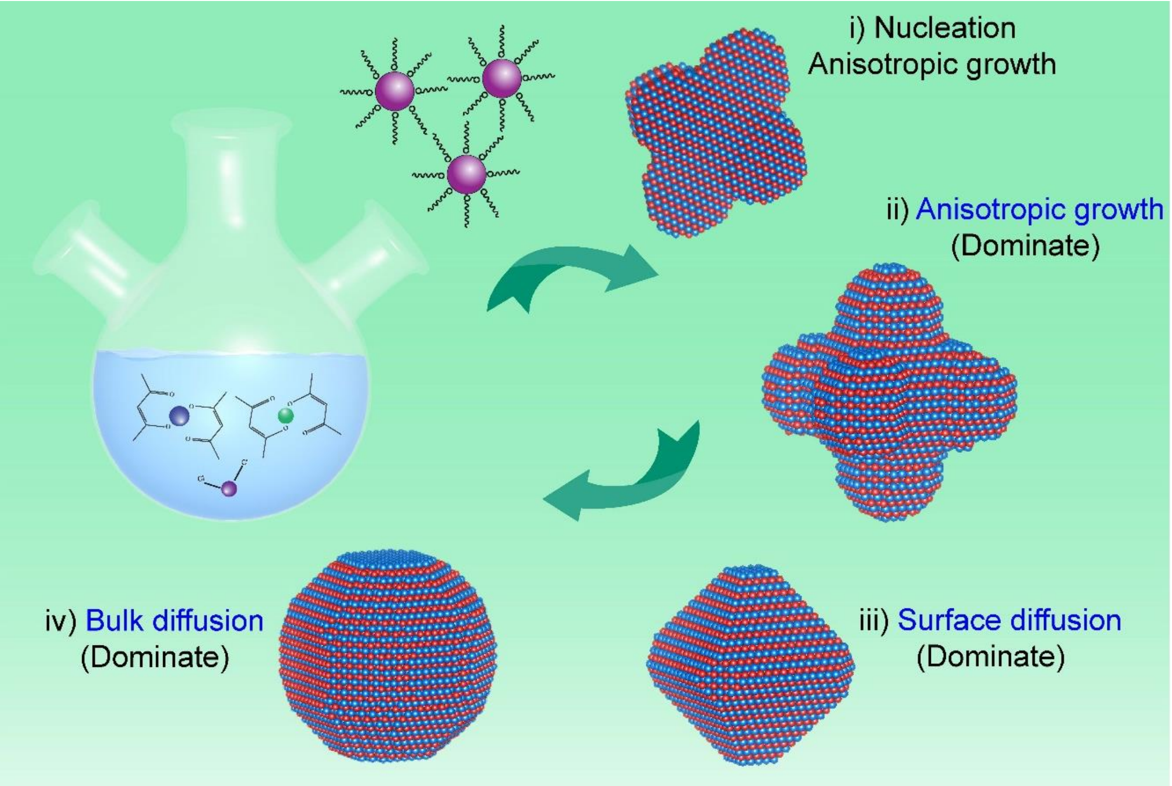

Fig. 5.8. Illustration of morphology and structure evolutions of one–pot synthesis of FePtCu nanoparticles at different reaction stage. i) Anisotropic nucleation and growth of branched shape and core-shell CuFePt. ii) Particle growth stage based on branched shape FePtCu. iii) Surface atoms diffuse from the branches to the surface, forming core–shell CuFePt with truncated-octahedron shape, dominated by surface diffusion. iv) Sphere shape particle with solid solution phase of FePtCu formed, demonstrating that bulk diffusion dominates the reactions.

5.4. Conclusion

In conclusion, crystalline growth behaviors of FePtCu during one–pot synthesis has been uncovered by advanced TEM imaging and spectrum technologies. Anisotropic growth, surface atoms diffusion and bulk atoms diffusion were proved to complete and dominate crystalline growth in sequence, resulting in branched shape and core–shell CuFePt, truncated-octahedron shape and core–shell CuFePt, sphere shape and alloy FePtCu nanoparticles, accordingly. Thus, shape controlled FePtCu nanoparticles with various exposed surface and core–shell/alloy structures can be synthesized by an efficient one–pot method at different reaction time, which also demonstrates high activity and high durability for oxygen reduction reaction. The truncated octahedron CuFePt (1 h) show 11.7 times higher mass activity than Pt/C, and only 0.5% half-wave potential degradation after 5000 cycling. The hexapod CuFePt (20 min) shows 12.1 times higher mass activity than Pt/C, and 3.1% half–wave potential loss after cycling. Nearly sphere shape alloy FePtCu (2 h) shows 5.3 times higher mass activity than Pt/C, and 2.9% half–wave potential loss after cycling. In contrast, Pt/C shows 14.9% half–wave potential loss after cycling under the same measurement conditions. This study is with significant importance for guiding the rational synthesis of low–Pt catalyst for oxygen reduction reaction.

Chapter 6

General conclusion and perspectives

Chemical ordered FePt nanoparticles have been synthesized by one–pot method, with Ag and Cu additives. The mechanisms for FePt phase transformation by Ag and Cu additives have been studied and have been shown to be different. Ag has larger atomic size and low solubility in FePt alloy. In our solution synthesis, Fe, Pt, Ag atoms simultaneously nucleate as alloys and grow at lower temperature, followed by particle growth and phase transformation at higher temperature. Ag diffuses out of the ternary alloy and leaves vacancies in the lattices, which promotes the diffusion of Fe/Pt atoms and thus enhance FePt ordering.

Chemical ordered FePtAg nanoparticles were successfully synthesized in three high boiling temperature solvents, hexadecylamine, trioctylamine, and octadecylamine with a one–step method. The solvent has a major impact on the chemical ordering and crystallization of the as-synthesized FePtAg nanoparticles. The room temperature coercivity as high as 5.23 kOe can be achieved for FePtAg synthesized in octadecylamine solvent, and the particles are with super fine size less than 4 nm. The coercivities of FePtAg particles synthesized in hexadecylamine and trioctylamine are 2.84 kOe and 2.81 kOe, respectively. They are with larger particle size distribution in hexadecylamine and sintered/aggregated into 5~15 nm particles in trioctylamine. More nuclei centers are formed in octadecylamine solvent than hexadecylamine/trioctylamine during the initial nuclei process, leaving less cations in solvent. In the following crystal growth process via ion-by-ion addition, FePtAg grow slowly in octadecylamine due to higher concentration of nuclei centers and lower concentration cations, thus, the FePtAg nanoparticles synthesized in octadecylamine would be uniform and smaller.

In contrast, Cu has a similar atom size as Fe and high solubility in FePt alloy. In this case, we have synthesized, by one–pot protocol, ordered FePtCu alloys with various compositions and it is clearly shown that Cu promotes the chemical ordering by alloying effect. The Cu alloying effect is the driving force of the FePtCu ordering, it is effective up to a Cu content of 40%. The crystalline behavior of FePtCu during the alloys formation steps has been unveiled by investigating the intermediate times of formation using atomic scale transmission electron microscopy techniques. The particle size increases with the Fe or Cu composition ratio, and the particles may sinter for Fe (50%) and Cu (> 20%). Therefore, the FePtCu composition is critical to form a CuFePt core–shell structure in the case of Cu with 20% ratio and Fe with more than 40%. Optimized $Fe_{45}Pt_{35}Cu_{20}$ nanoparticles with core–shell and a 4~5 atomic layer Pt-rich surface structure show better ORR catalysis performance than commercial Pt/C, or 4 times mass activity along with good stability.

The crystalline growth of FePtCu during one–pot synthesis has been uncovered by advanced TEM imaging and spectrometry investigations. Anisotropic growth, surface and bulk atoms diffusion were proved to compete and govern the nanoparticle growth in sequence, resulting in branched shape, core–shell CuFePt, truncated-octahedrons and core–shell Cu–FePt, sphere shape and alloy FePtCu nanoparticles, sequentially. Thus, shape controlled FePtCu nanoparticles with limiting surfaces and core–shell/alloy structures can be synthesized by an efficient one–pot method at different reaction times leading to high activity and high durability for oxygen reduction reaction. The truncated octahedron Cu–FePt (1 h) show 11.7 times higher mass activity than Pt/C, and only 0.5% half-wave potential degradation after 5000 cycling. The hexapod CuFePt (20 min) shows 12.1 times higher mass activity than Pt/C, and 3.1% half–wave potential loss after cycling. Nearly sphere shape alloy FePtCu (2 h) shows 5.3 times higher mass activity than Pt/C, and 2.9% half–wave potential loss after cycling. This is contrast to Pt/C which undergoes 14.9% half–wave potential loss after cycling under the same measurement conditions.

The next steps to further enhance the oxygen reduction catalysis performance may include preparing well dispersed FePt/C catalyst after removing silver from FePtAg with super fine size, due to its small size and magnetism which causes serious aggregation problem.

Smaller size FePtCu with modified platinum surface also needs further investigation. Theoretical calculations will be very useful to elucidate the intrinsic relationship between the structure and the high electrocatalytic activities, as well as guiding the synthesis of low-Pt alloy catalyst. Membrane electrode of fuel cell device measurement is needed to characterize the catalyst in real fuel cell environment.

Biographical Note

Education:

2005 – 2009 **B. Eng.** Microelectronics

Northwestern Polytechnical University

2012 – 2015 **M. Eng.** Nanoscience and nanotechnology

Hubei University, Supervised by Prof. Hao Wang

2015 – 2019 **Ph.D.** Physics

Hubei University, Supervised by Prof. Hao Wang

Max Plank Institute for Solid State Research, Supervised by Prof. Dr. Peter A. van Aken

University of Caen Normandy, CNRS, Supervised by Dr. Pierre Ruterana

Conference Contributions:

[1] EMRS-2019 Spring, 2019. 05, Nice, Oral contribution, *Graduate Students Award*

[2] StEM workshop Ringberg Castle, 2019. 07, Oral contribution

[3] EMAT workshop, Antwerpen, 2019. 06, Poster contribution

[4] StEM workshop Ringberg Castle, 2018. 07, Poster contribution

[5] ISGC 2017, May 2017, La Rochelle, France, Poster contribution

[6] The 2nd ISECS, June 2016, Xiamen, China, Poster contribution

Honors and Awards:

Scholarship Award, China Scholarship Council

Graduate Students Award, EMRS-2019 Spring Conference

Outstanding Master's Thesis of Hubei Province

List of Publications:

[1] **X. Chen**, H. Wang, H. Wan, T. Wu, D. Shu, L. Shen, Y. Wang, P. Ruterana, P. D. Lund and H. Wang

Nano Energy 2018, 54, 280 (*Journal Cover Paper*)

[2] **X. Chen**, Y. Wang, H. B. Wang, D. Shu, J. Zhang, P. Ruterana and H. Wang

J. Mater. Chem. C 2017, 5, 5316 (*Journal Cover Paper*)

[3] J. C. Yu, **X. Chen**, (first co-author) Y. Wang, H. Zhou, M. N. Xue, Y. Xu, Z. S. Li, C. Ye, J. Zhang, P. A. van Aken, P. D. Lund and H. Wang

J. Mater. Chem. C 2016, 4, 7302

[4] **Xu Chen**, Yi Wang, Tianci Wu, et al, One–pot Synthesis of Efficient FePtCu Catalyst: Morphology and Composition Evolution Characterization by Quasi in-situ STEM

Paper in preparation

[5] H. B. Wang, Y. Li, **X. Chen**, D. Shu, X. Liu, X. N. Wang, J. Zhang, H. Wang, Y. Wang and P. Ruterana

J. Magn. Magn. Mater. 2017, 422, 470

[6] J. J. Xiang, H. B. Wang, X. N. Wang, **X. Chen**, T. C. Wu, H. Z. Wan, Y. Z. Liu and H. Wang

RSC Adv. 2019, 9, 4001

[7] D. Shu, H. B. Wang, Y. Wang, Y. Li, X. Liu, **X. Chen**, X. N. Peng, X. Wang, P. Ruterana and H. Wang

Int. J. Hydrog. Energy 2017, 42, 20888

[8] H. B. Wang, Y. Li, D. Shu, **X. Chen**, X. Liu, X. Wang, J. Zhang and H. Wang

Int. J. Energy Res. 2016, 40, 1280.

References

1. Strasser, P.; Gliech, M.; Kuehl, S.; Moeller, T., Electrochemical processes on solid shaped nanoparticles with defined facets. *Chem. Soc. Rev.* **2018,** *47* (3), 715−735.

2. Seh, Z. W.; Kibsgaard, J.; Dickens, C. F.; Chorkendorff, I.; Nørskov, J. K.; Jaramillo, T. F., Combining theory and experiment in electrocatalysis: Insights into materials design. *Science* **2017,** *355* (6321), 4998.

3. Stamenkovic, V. R.; Strmcnik, D.; Lopes, P. P.; Markovic, N. M., Energy and fuels from electrochemical interfaces. *Nat. Mater.* **2016,** *16*, 57.

4. Bonaccorso, F.; Colombo, L.; Yu, G.; Stoller, M.; Tozzini, V.; Ferrari, A. C.; Ruoff, R. S.; Pellegrini, V., Graphene, related two−dimensional crystals, and hybrid systems for energy conversion and storage. *Science* **2015,** *347* (6217), 1246501.

5. Li, W.; Liu, J.; Zhao, D., Mesoporous materials for energy conversion and storage devices. *Nat. Rev. Mater.* **2016,** *1*, 16023.

6. Shao, M.; Chang, Q.; Dodelet, J. P.; Chenitz, R., Recent Advances in Electrocatalysts for Oxygen Reduction Reaction. *Chem. Rev.* **2016,** *116* (6), 3594−3657.

7. X. Li; Zhao, T. S., Advances in Fuel Cells. *Elsevier Ltd, Oxford, UK* **2007**.

8. Panayiotou, G.; Kalogirou, S.; Tassou, S., PEM Fuel Cells for Energy Production in Solar Hydrogen Systems. *Recent Patents on Mechanical Engineering* **2010,** *3*, 226−235.

9. Xiong, Y.; Yang, Y.; DiSalvo, F. J.; Abruna, H. D., Pt−Decorated Composition−Tunable Pd−Fe@Pd/C Core−Shell Nanoparticles with Enhanced Electrocatalytic Activity toward the Oxygen Reduction Reaction. *J. Am. Chem. Soc.* **2018,** *140* (23), 7248−7255.

10. Tian, X. L.; Luo, J. M.; Nan, H. X.; Zou, H. B.; Chen, R.; Shu, T.; Li, X. H.; Li, Y. W.; Song, H. Y.; Liao, S. J.; Adzic, R. R., Transition Metal Nitride Coated with Atomic Layers of Pt as a Low−Cost, Highly Stable Electrocatalyst for the Oxygen Reduction Reaction. *J. Am. Chem. Soc.* **2016,** *138* (5), 1575−1583.

11. Qian, J.; Shen, M.; Zhou, S.; Lee, C. T.; Zhao, M.; Lyu, Z. H.; Hood, Z. D.; Vara, M.; Gilroy, K. D.; Wang, K.; Xia, Y. N., Synthesis of Pt nanocrystals with different shapes using the same protocol to optimize their catalytic activity toward oxygen reduction. *Mater. Today* **2018,** *21* (8), 834−844.

12. Chen, S.; Niu, Z.; Xie, C.; Gao, M.; Lai, M.; Li, M.; Yang, P., Effects of Catalyst Processing on the Activity and Stability of Pt–Ni Nanoframe Electrocatalysts. *ACS Nano* **2018,** *12* (8), 8697−8705.

13. Vielstich, W.; Yokokawa, H.; Gasteiger, H. A., Handbook of Fuel Cells. **2003**.

14. Briega Martos, V.; Herrero, E.; Feliu, J. M., Effect of pH and Water Structure on the Oxygen Reduction Reaction on platinum electrodes. *Electrochim. Acta* **2017,** *241*, 497−509.

15. Shamim, S.; Sudhakar, K.; Choudhary, B.; Anwer, J., A review on recent advances in proton exchange membrane fuel cells: Materials, technology and applications. *Adv. Appl. Sci. Res.* **2015,** *6*, 89−100.

16. Wang, Y.; Chen, K. S.; Mishler, J.; Cho, S. C.; Adroher, X. C., A review of polymer electrolyte membrane fuel cells: Technology, applications, and needs on fundamental research. *Appl. Energ.* **2011,** *88* (4), 981−1007.

17. Wee, J. H., Applications of proton exchange membrane fuel cell systems. *Renew. Sustain. Energ. Rev.* **2007,** *11* (8), 1720−1738.

18. Yoshida, T.; Kojima, K., Toyota MIRAI Fuel Cell Vehicle and Progress Toward a Future Hydrogen Society. *Electrochem. Soc. Interf.* **2015,** *24* (2), 45−49.

19. Wang, C.; Mao, Z.; Bao, F.; Li, X.; Xie, X., Development and performance of 5kw proton exchange membrane fuel cell stationary power system. *Int. J. Hydrog. Energy* **2005,** *30* (9), 1031−1034.

20. Ladewig, B. P.; Lapicque, F., Analysis of the Ripple Current in a 5 kW Polymer Electrolyte Membrane Fuel Cell Stack. *Fuel Cells* **2009,** *9* (2), 157−163.

21. Hwang, J. J.; Zou, M. L., Development of a proton exchange membrane fuel cell cogeneration system. *J. Power Sources* **2010,** *195* (9), 2579−2585.

22. Wang, X. X.; Swihart, M. T.; Wu, G., Achievements, challenges and perspectives on cathode catalysts in proton exchange membrane fuel cells for transportation. *Nat. Catalysis* **2019,** *2* (7), 578−589.

23. Norskov, J. K.; Rossmeisl, J.; Logadottir, A.; Lindqvist, L.; Kitchin, J. R.; Bligaard, T.; Jonsson, H., Origin of the overpotential for oxygen reduction at a fuel−cell cathode. *J. Phys. Chem. B* **2004,** *108* (46), 17886−17892.

24. Li, D. G.; Lv, H. F.; Kang, Y. J.; Markovic, N. M.; Stamenkovic, V. R., Progress in the Development of Oxygen Reduction Reaction Catalysts for Low−Temperature Fuel Cells. *Annu. Rev. Chem. Biomol.,* 2016, 7, 509−532.

25. Li, H. H.; Ma, S. Y.; Fu, Q. Q.; Liu, X. J.; Wu, L.; Yu, S. H., Scalable Bromide–Triggered Synthesis of Pd@Pt Core–Shell Ultrathin Nanowires with Enhanced Electrocatalytic Performance toward Oxygen Reduction Reaction. *J. Am. Chem. Soc.* **2015,** *137* (24), 7862−7868.

26. Li, Q. H.; Chen, W. X.; Xiao, H.; Gong, Y.; Li, Z.; Zheng, L. R.; Zheng, X. S.; Yan, W. S.; Cheong, W. C.; Shen, R. A.; Fu, N. H.; Gu, L.; Zhuang, Z. B.; Chen, C.; Wang, D. S.; Peng, Q.; Li, J.; Li, Y. D., Fe Isolated Single Atoms on S, N Codoped Carbon by Copolymer Pyrolysis Strategy for Highly Efficient Oxygen Reduction Reaction. *Adv. Mater.* **2018,** *30* (25), 6.

27. Strasser, P., Free Electrons to Molecular Bonds and Back: Closing the Energetic Oxygen Reduction (ORR)−Oxygen Evolution (OER) Cycle Using Core−Shell Nanoelectrocatalysts. *Accounts Chem. Res.* **2016,** *49* (11), 2658−2668.

28. Ren, H.; Wang, Y.; Yang, Y.; Tang, X.; Peng, Y. Q.; Peng, H. Q.; Xiao, L.; Lu, J. T.; Abruna, H. D.; Zhuang, L., Fe/N/C Nanotubes with Atomic Fe Sites: A Highly Active Cathode Catalyst for Alkaline Polymer Electrolyte Fuel Cells. *ACS Catalysis* **2017,** *7* (10), 6485−6492.

29. Sandoval−Rojas, A. P.; Gomez−Marin, A. M.; Suarez−Herrera, M. F.; Climent, V.; Feliu, J. M., Role of the interfacial water structure on electrocatalysis: Oxygen reduction on Pt(111) in methanesulfonic acid. *Catalysis Today* **2016,** *262*, 95−99.

30. Lv, H. F.; Li, D. G.; Strmcnik, D.; Paulikas, A. P.; Markovic, N. M.; Stamenkovic, V. R., Recent advances in the design of tailored nanomaterials for efficient oxygen reduction reaction. *Nano Energy* **2016,** *29*, 149−165.

31. Xiong, Y.; Xiao, L.; Yang, Y.; DiSalvo, F. J.; Abruna, H. D., High–Loading Intermetallic Pt_3Co/C Core−Shell Nanoparticles as Enhanced Activity Electrocatalysts toward the Oxygen Reduction Reaction (ORR). *Chem. Mater.* **2018,** *30* (5), 1532−1539.

32. Rizo, R.; Aran−Ais, R. M.; Padgett, E.; Muller, D. A.; Lazaro, M. J.; Solla−Gullon, J.; Feliu, J. M.; Pastor, E.; Abruna, H. D., $Pt{-}Rich_{core}/Sn{-}Rich_{subsurface}/Pt_{skin}$ Nanocubes As Highly Active and Stable Electrocatalysts for the Ethanol Oxidation Reaction. *J. Am. Chem. Soc.* **2018,** *140* (10), 3791−3797.

33. Nguyen, M. T.; Wakabayashi, R. H.; Yang, M. H.; Abruna, H. D.; DiSalvo, F. J., Synthesis of carbon supported ordered tetragonal pseudo−ternary $Pt_2M'M''$ (M = Fe, Co, Ni) nanoparticles and their activity for oxygen reduction reaction. *J. Power Sources* **2015,** *280*, 459−466.

34. Beermann, V.; Gocyla, M.; Willinger, E.; Rudi, S.; Heggen, M.; Dunin−Borkowski, R. E.; Willinger, M. G.; Strasser, P., Rh−Doped Pt−Ni Octahedral Nanoparticles: Understanding the Correlation between Elemental Distribution, Oxygen Reduction Reaction, and Shape Stability. *Nano Lett.* **2016,** *16* (3), 1719−1725.

35. Wang, D. L.; Yu, Y. C.; Zhu, J.; Liu, S. F.; Muller, D. A.; Abruna, H. D., Morphology and Activity Tuning of Cu3Pt/C Ordered Intermetallic Nanoparticles by Selective Electrochemical Dealloying. *Nano Lett.* **2015,** *15* (2), 1343−1348.

36. Li, J.; Sharma, S.; Liu, X.; Pan, Y. T.; Spendelow, J. S.; Chi, M.; Jia, Y.; Zhang, P.; Cullen, D. A.; Xi, Z.; Lin, H.; Yin, Z.; Shen, B.; Muzzio, M.; Yu, C.; Kim, Y. S.; Peterson, A. A.; More, K. L.; Zhu, H.; Sun, S., Hard−Magnet $L1_0$−CoPt Nanoparticles Advance Fuel Cell Catalysis. *Joule* **2018**, *3*, 1−12.

37. Kulkarni, A.; Siahrostami, S.; Patel, A.; Norskov, J. K., Understanding Catalytic Activity Trends in the Oxygen Reduction Reaction. *Chem. Rev.* **2018,** *118* (5), 2302−2312.

38. Deng, Y. J.; Tripkovic, V.; Rossmeisl, J.; Arenz, M., Oxygen Reduction Reaction on Pt Overlayers Deposited onto a Gold Film: Ligand, Strain, and Ensemble Effect. *ACS Catal.* **2016,** *6* (2), 671−676.

39. Sui, S.; Wang, X. Y.; Zhou, X. T.; Su, Y. H.; Riffatc, S.; Liu, C. J., A comprehensive review of Pt electrocatalysts for the oxygen reduction reaction: Nanostructure, activity, mechanism and carbon support in PEM fuel cells. *J. Mater. Chem. A* **2017,** *5* (5), 1808−1825.

40. Keith, J. A.; Jerkiewicz, G.; Jacob, T., Theoretical Investigations of the Oxygen Reduction Reaction on Pt(111). *ChemPhysChem* **2010,** *11* (13), 2779−2794.

41. Nie, Y.; Li, L.; Wei, Z. D., Recent advancements in Pt and Pt−free catalysts for oxygen reduction reaction. *Chem. Soc. Rev.* **2015,** *44* (8), 2168−2201.

42. Gómez−Marín, A. M.; Rizo, R.; Feliu, J. M., Oxygen reduction reaction at Pt single crystals: a critical overview. *Catal. Sci. Technol.* **2014,** *4* (6), 1685−1698.

43. Gomez–Marin, A. M.; Feliu, J. M., Role of oxygen–containing species at Pt(111) on the oxygen reduction reaction in acid media. *J. Solid State Electrochem.* **2015,** *19* (9), 2831−2841.

44. Clavilier, J.; Armand, D.; Sun, S. G.; Petit, M., Electrochemical adsorption behaviour of platinum stepped surfaces in sulphuric acid solutions. *J. Electroanal. Chem. Interf. Electrochem.* **1986,** *205* (1), 267−277.

45. Dong, J. C.; Zhang, X. G.; Briega Martos, V.; Jin, X.; Yang, J.; Chen, S.; Yang, Z. L.; Wu, D. Y.; Feliu, J. M.; Williams, C. T.; Tian, Z. Q.; Li, J. F., In situ Raman spectroscopic evidence for oxygen reduction reaction intermediates at platinum single−crystal surfaces. *Nat. Energy* **2019**, *4*, 60−67.

46. Jukk, K.; Kongi, N.; Tammeveski, K.; Solla–Gullon, J.; Feliu, J. M., Electroreduction of Oxygen on PdPt Alloy Nanocubes in Alkaline and Acidic Media. *ChemElectroChem* **2017,** *4* (10), 2547−2555.

47. Gomez–Marin, A. M.; Rizo, R.; Feliu, J. M., Oxygen reduction reaction at Pt single crystals: a critical overview. *Catal. Sci. Technol.* **2014,** *4* (6), 1685−1698.

48. Stamenkovic, V. R.; Fowler, B.; Mun, B. S.; Wang, G. F.; Ross, P. N.; Lucas, C. A.; Markovic, N. M., Improved oxygen reduction activity on $Pt_3Ni(111)$ via increased surface site availability. *Science* **2007,** *315* (5811), 493−497.

49. Chen, C.; Kang, Y. J.; Huo, Z. Y.; Zhu, Z. W.; Huang, W. Y.; Xin, H. L. L.; Snyder, J. D.; Li, D. G.; Herron, J. A.; Mavrikakis, M.; Chi, M. F.; More, K. L.; Li, Y. D.; Markovic, N. M.; Somorjai, G. A.; Yang, P. D.; Stamenkovic, V. R., Highly Crystalline Multimetallic Nanoframes with Three–Dimensional Electrocatalytic Surfaces. *Science* **2014,** *343* (6177), 1339−1343.

50. Niu, Z. Q.; Becknell, N.; Yu, Y.; Kim, D.; Chen, C.; Kornienko, N.; Somorjai, G. A.; Yang, P. D., Anisotropic phase segregation and migration of Pt in nanocrystals en route to nanoframe catalysts. *Nat. Mater.* **2016,** *15* (11), 1188.

51. Huang, X. Q.; Zhao, Z. P.; Cao, L.; Chen, Y.; Zhu, E. B.; Lin, Z. Y.; Li, M. F.; Yan, A. M.; Zettl, A.; Wang, Y. M.; Duan, X. F.; Mueller, T.; Huang, Y., High−performance transition metal−doped Pt3Ni octahedra for oxygen reduction reaction. *Science* **2015,** *348* (6240), 1230−1234.

52. Shao, M.; Peles, A.; Shoemaker, K., Electrocatalysis on Platinum Nanoparticles: Particle Size Effect on Oxygen Reduction Reaction Activity. *Nano Lett.* **2011,** *11* (9), 3714−3719.

53. Yano, H.; Inukai, J.; Uchida, H.; Watanabe, M.; Babu, P. K.; Kobayashi, T.; Chung, J. H.; Oldfield, E.; Wieckowski, A., Particle−size effect of nanoscale platinum catalysts in oxygen reduction reaction: an electrochemical and Pt−195 EC−NMR study. *Phys. Chem. Chem. Phys.* **2006,** *8* (42), 4932−4939.

54. Nesselberger, M.; Ashton, S.; Meier, J. C.; Katsounaros, I.; Mayrhofer, K. J. J.; Arenz, M., The Particle Size Effect on the Oxygen Reduction Reaction Activity of Pt Catalysts: Influence of Electrolyte and Relation to Single Crystal Models. *J. Am. Chem. Soc.* **2011,** *133* (43), 17428−17433.

55. Nesselberger, M.; Roefzaad, M.; Hamou, R. F.; Biedermann, P. U.; Schweinberger, F. F.; Kunz, S.; Schloegl, K.; Wiberg, G. K. H.; Ashton, S.; Heiz, U.; Mayrhofer, K. J. J.;

Arenz, M., The effect of particle proximity on the oxygen reduction rate of size−selected platinum clusters. *Nat. Mater.* **2013,** *12* (10), 919−924.

56. Gan, L.; Rudi, S.; Cui, C. H.; Heggen, M.; Strasser, P., Size−Controlled Synthesis of Sub–10 nm $PtNi_3$ Alloy Nanoparticles and their Unusual Volcano−Shaped Size Effect on ORR Electrocatalysis. *Small* **2016,** *12* (23), 3189−3196.

57. Wang, C.; Wang, G. F.; van der Vliet, D.; Chang, K. C.; Markovic, N. M.; Stamenkovic, V. R., Monodisperse Pt_3Co nanoparticles as electrocatalyst: the effects of particle size and pretreatment on electrocatalytic reduction of oxygen. *Phys. Chem. Chem. Phys.* **2010,** *12* (26), 6933−6939.

58. Aran−Ais, R. M.; Solla−Gullon, J.; Gocyla, M.; Heggen, M.; Dunin−Borkowski, R. E.; Strasser, P.; Herrero, E.; Feliu, J. M., The effect of interfacial pH on the surface atomic elemental distribution and on the catalytic reactivity of shape−selected bimetallic nanoparticles towards oxygen reduction. *Nano Energy* **2016,** *27*, 390−401.

59. Jukk, K.; Kongi, N.; Tammeveski, K.; Solla−Gullon, J.; Feliu, J. M., PdPt alloy nanocubes as electrocatalysts for oxygen reduction reaction in acid media. *Electrochem. Commun.* **2015,** *56*, 11−15.

60. He, D. P.; Zhang, L. B.; He, D. S.; Zhou, G.; Lin, Y.; Deng, Z. X.; Hong, X.; Wu, Y.; Chen, C.; Li, Y. D., Amorphous nickel boride membrane on a platinum–nickel alloy surface for enhanced oxygen reduction reaction. *Nat. Commun.* **2016,** *7*, 8.

61. Watanabe, M.; Tryk, D. A.; Wakisaka, M.; Yano, H.; Uchida, H., Overview of recent developments in oxygen reduction electrocatalysis. *Electrochim. Acta* **2012,** *84*, 187−201.

62. Wakisaka, M.; Mitsui, S.; Hirose, Y.; Kawashima, K.; Uchida, H.; Watanabe, M., Electronic structures of Pt−Co and Pt−Ru alloys for Co−tolerant anode catalysts in polymer electrolyte fuel cells studied by EC−XPS. *J. Phys. Chem. B* **2006,** *110* (46), 23489−23496.

63. Stamenkovic, V. R.; Mun, B. S.; Arenz, M.; Mayrhofer, K. J. J.; Lucas, C. A.; Wang, G. F.; Ross, P. N.; Markovic, N. M., Trends in electrocatalysis on extended and nanoscale Pt−bimetallic alloy surfaces. *Nat. Mater.* **2007,** *6* (3), 241−247.

64. Mao, J. J.; Chen, W. X.; Sun, W. M.; Chen, Z.; Pei, J. J.; He, D. S.; Lv, C. L.; Wang, D. S.; Li, Y. D., Rational Control of the Selectivity of a Ruthenium Catalyst for Hydrogenation of 4−Nitrostyrene by Strain Regulation. *Angew. Chem. Int. Edit.* **2017,** *56* (39), 11971−11975.

65. Wang, L.; Zeng, Z.; Gao, W.; Maxson, T.; Raciti, D.; Giroux, M.; Pan, X.; Wang, C.; Greeley, J., Tunable intrinsic strain in two−dimensional transition metal electrocatalysts. *Science* **2019,** *363* (6429), 870−874.

66. Strasser, P.; Koh, S.; Anniyev, T.; Greeley, J.; More, K.; Yu, C. F.; Liu, Z. C.; Kaya, S.; Nordlund, D.; Ogasawara, H.; Toney, M. F.; Nilsson, A., Lattice−strain control of the activity in dealloyed core−shell fuel cell catalysts. *Nat. Chem.* **2010,** *2* (6), 454−460.

67. He, D. S.; He, D. P.; Wang, J.; Lin, Y.; Yin, P. Q.; Hong, X.; Wu, Y.; Li, Y. D., Ultrathin Icosahedral Pt−Enriched Nanocage with Excellent Oxygen Reduction Reaction Activity. *J. Am. Chem. Soc.* **2016,** *138* (5), 1494−1497.

68. Jukk, K.; Kongi, N.; Tammeveski, K.; Aran−Ais, R. M.; Solla−Gullon, J.; Feliu, J. M., Loading effect of carbon–supported platinum nanocubes on oxygen electroreduction. *Electrochim. Acta* **2017,** *251*, 155−166.

69. Vidal−Iglesias, F. J.; Solla−Gullon, J.; Feliu, J. M., *Recent Advances in the Use of Shape−Controlled Metal Nanoparticles in Electrocatalysis*. Springer International Publishing Ag: Cham, 2016, 31−92.

70. Gocyla, M.; Kuehl, S.; Shviro, M.; Heyen, H.; Selve, S.; Dunin−Borkowski, R. E.; Heggen, M.; Strasser, P., Shape Stability of Octahedral PtNi Nanocatalysts for Electrochemical Oxygen Reduction Reaction Studied by in situ Transmission Electron Microscopy. *ACS Nano* **2018,** *12* (6), 5306−5311.

71. Gan, L.; Heggen, M.; Cui, C. H.; Strasser, P., Thermal Facet Healing of Concave Octahedral Pt−Ni Nanoparticles Imaged in Situ at the Atomic Scale: Implications for the Rational Synthesis of Durable High–Performance ORR Electrocatalysts. *ACS Catalysis* **2016,** *6* (2), 692−695.

72. Wang, X.; Vara, M.; Luo, M.; Huang, H. W.; Ruditskiy, A.; Park, J.; Bao, S. X.; Liu, J. Y.; Howe, J.; Chi, M. F.; Xie, Z. X.; Xia, Y. N., Pd@Pt Core−Shell Concave Decahedra: A Class of Catalysts for the Oxygen Reduction Reaction with Enhanced Activity and Durability. *J. Am. Chem. Soc.* **2015,** *137* (47), 15036−15042.

73. Strasser, P.; Kuhl, S., Dealloyed Pt–based core–shell oxygen reduction electrocatalysts. *Nano Energy* **2016,** *29*, 166−177.

74. Cai, B.; Hubner, R.; Sasaki, K.; Zhang, Y. Z.; Su, D.; Ziegler, C.; Vukmirovic, M. B.; Rellinghaus, B.; Adzic, R. R.; Eychmuller, A., Core−Shell Structuring of Pure Metallic Aerogels towards Highly Efficient Platinum Utilization for the Oxygen Reduction Reaction. *Angew. Chem. Int. Edit.* **2018,** *57* (11), 2963−2966.

75. Tian, X. L.; Tang, H. B.; Luo, J. M.; Nan, H. X.; Shu, T.; Du, L.; Zeng, J. H.; Liao, S. J.; Adzic, R. R., High−Performance Core−Shell Catalyst with Nitride Nanoparticles as a Core: Well−Defined Titanium Copper Nitride Coated with an Atomic Pt Layer for the Oxygen Reduction Reaction. *ACS Catalysis* **2017,** *7* (6), 3810−3817.

76. Ma, Y. L.; Gao, W. P.; Shan, H.; Chen, W. L.; Shang, W.; Tao, P.; Song, C. Y.; Addiego, C.; Deng, T.; Pan, X. Q.; Wu, J. B., Platinum−Based Nanowires as Active Catalysts toward Oxygen Reduction Reaction: In Situ Observation of Surface−Diffusion−Assisted, Solid−State Oriented Attachment. *Adv. Mater.* **2017,** *29* (46), 8.

77. Jiang, K.; Zhao, D.; Guo, S.; Zhang, X.; Zhu, X.; Guo, J.; Lu, G.; Huang, X., Efficient oxygen reduction catalysis by subnanometer Pt alloy nanowires. *Sci. Adv.* **2017,** *3* (2), e1601705.

78. Li, M. F.; Zhao, Z. P.; Cheng, T.; Fortunelli, A.; Chen, C. Y.; Yu, R.; Zhang, Q. H.; Gu, L.; Merinov, B. V.; Lin, Z. Y.; Zhu, E. B.; Yu, T.; Jia, Q. Y.; Guo, J. H.; Zhang, L.; Goddard, W. A.; Huang, Y.; Duan, X. F., Ultrafine jagged platinum nanowires enable ultrahigh mass activity for the oxygen reduction reaction. *Science* **2016,** *354* (6318), 1414−1419.

79. Becknell, N.; Son, Y.; Kim, D.; Li, D. G.; Yu, Y.; Niu, Z. Q.; Lei, T.; Sneed, B. T.; More, K. L.; Markovic, N. M.; Stamenkovic, V. R.; Yang, P. D., Control of Architecture in Rhombic Dodecahedral Pt−Ni Nanoframe Electrocatalysts. *J. Am. Chem. Soc.* **2017,** *139* (34), 11678−11681.

80. Liu, J.; Jiao, M. G.; Lu, L. L.; Barkholtz, H. M.; Li, Y. P.; Wang, Y.; Jiang, L. H.; Wu, Z. J.; Liu, D. J.; Zhuang, L.; Ma, C.; Zeng, J.; Zhang, B. S.; Su, D. S.; Song, P.; Xing, W.; Xu, W. L.; Wang, Y.; Jiang, Z.; Sun, G. Q., High performance platinum single atom electrocatalyst for oxygen reduction reaction. *Nat. Commun.* **2017,** *8*, 9.

81. Vukmirovic, M. B.; Teeluck, K. M.; Liu, P.; Adzic, R. R., Single Platinum Atoms Electrocatalysts: Oxygen Reduction and Hydrogen Oxidation Reactions. *Croat. Chem. Acta* **2017,** *90* (2), 225−230.

82. Han, Y. H.; Wang, Y. G.; Xu, R. R.; Chen, W. X.; Zheng, L. R.; Han, A. J.; Zhu, Y. Q.; Zhang, J.; Zhang, H. B.; Luo, J.; Chen, C.; Peng, Q.; Wang, D. S.; Li, Y. D., Electronic structure engineering to boost oxygen reduction activity by controlling the coordination of the central metal. *Energy Environ. Sci.* **2018,** *11* (9), 2348−2352.

83. Han, Y. H.; Wang, Y. G.; Chen, W. X.; Xu, R. R.; Zheng, L. R.; Zhang, J.; Luo, J.; Shen, R. A.; Zhu, Y. Q.; Cheong, W. C.; Chen, C.; Peng, Q.; Wang, D. S.; Li, Y. D.,

Hollow N–Doped Carbon Spheres with Isolated Cobalt Single Atomic Sites: Superior Electrocatalysts for Oxygen Reduction. *J. Am. Chem. Soc.* **2017,** *139* (48), 17269−17272.

84. Chen, Y. J.; Ji, S. F.; Wang, Y. G.; Dong, J. C.; Chen, W. X.; Li, Z.; Shen, R. A.; Zheng, L. R.; Zhuang, Z. B.; Wang, D. S.; Li, Y. D., Isolated Single Iron Atoms Anchored on N−Doped Porous Carbon as an Efficient Electrocatalyst for the Oxygen Reduction Reaction. *Angew. Chem. Int. Edit.* **2017,** *56* (24), 6937−6941.

85. Zitolo, A.; Ranjbar−Sahraie, N.; Mineva, T.; Li, J. K.; Jia, Q. Y.; Stamatin, S.; Harrington, G. F.; Lyth, S. M.; Krtil, P.; Mukerjee, S.; Fonda, E.; Jaouen, F., Identification of catalytic sites in cobalt−nitrogen−carbon materials for the oxygen reduction reaction. *Nat. Commun.* **2017,** *8*, 11.

86. Wang, D. L.; Liu, S. F.; Wang, J.; Lin, R. Q.; Kawasaki, M.; Rus, E.; Silberstein, K. E.; Lowe, M. A.; Lin, F.; Nordlund, D.; Liu, H. F.; Muller, D. A.; Xin, H. L. L.; Abrun, H. D., Spontaneous incorporation of gold in palladium−based ternary nanoparticles makes durable electrocatalysts for oxygen reduction reaction. *Nat. Commun.* **2016,** *7*, 9.

87. Zhang, J. T.; Zhao, Z. H.; Xia, Z. H.; Dai, L. M., A metal−free bifunctional electrocatalyst for oxygen reduction and oxygen evolution reactions. *Nat. Nanotechnol.* **2015,** *10* (5), 444−452.

88. Abroshan, H.; Bothra, P.; Back, S.; Kulkarni, A.; Norskov, J. K.; Siahrostami, S., Ultrathin Cobalt Oxide Overlayer Promotes Catalytic Activity of Cobalt Nitride for the Oxygen Reduction Reaction. *J. Phys. Chem. C* **2018,** *122* (9), 4783−4791.

89. To, J. W. F.; Ng, J. W. D.; Siahrostami, S.; Koh, A. L.; Lee, Y. J.; Chen, Z. H.; Fong, K. D.; Chen, S. C.; He, J. J.; Bae, W. G.; Wilcox, J.; Jeong, H. Y.; Kim, K.; Studt, F.; Norskov, J. K.; Jaramillo, T. F.; Bao, Z. N., High–performance oxygen reduction and evolution carbon catalysis: From mechanistic studies to device integration. *Nano Res.* **2017,** *10* (4), 1163−1177.

90. Koitz, R.; Norskov, J. K.; Studt, F., A systematic study of metal−supported boron nitride materials for the oxygen reduction reaction. *Phys. Chem. Chem. Phys.* **2015,** *17* (19), 12722−12727.

91. Leonard, N. D.; Wagner, S.; Luo, F.; Steinberg, J.; Ju, W.; Weidler, N.; Wang, H.; Kramm, U. I.; Strasser, P., Deconvolution of Utilization, Site Density, and Turnover Frequency of Fe Nitrogen Carbon Oxygen Reduction Reaction Catalysts Prepared with Secondary N–Precursors. *ACS Catalysis* **2018,** *8* (3), 1640−1647.

92. Yu, H. J.; Shang, L.; Bian, T.; Shi, R.; Waterhouse, G. I. N.; Zhao, Y. F.; Zhou, C.; Wu, L. Z.; Tung, C. H.; Zhang, T. R., Nitrogen–Doped Porous Carbon Nanosheets

Templated from g−C_3N_4 as Metal−Free Electrocatalysts for Efficient Oxygen Reduction Reaction. *Adv. Mater.* **2016,** *28* (25), 5080−5086.

93. Xia, Z. H.; An, L.; Chen, P. K.; Xia, D. G., Non−Pt Nanostructured Catalysts for Oxygen Reduction Reaction: Synthesis, Catalytic Activity and its Key Factors. *Adv. Energy Mater.* **2016,** *6* (17), 29.

94. Lu, Z. Y.; Xu, W. W.; Ma, J.; Li, Y. J.; Sun, X. M.; Jiang, L., Superaerophilic Carbon−Nanotube−Array Electrode for High−Performance Oxygen Reduction Reaction. *Adv. Mater.* **2016,** *28* (33), 7155.

95. Liu, Q.; Du, L.; Fu, G.; Cui, Z.; Li, Y.; Dang, D.; Gao, X.; Zheng, Q.; Goodenough, J. B., Structurally Ordered Fe3Pt Nanoparticles on Robust Nitride Support as a High Performance Catalyst for the Oxygen Reduction Reaction. *Adv. Energy Mater.* **2019,** *9* (3), 1803040.

96. Kim, J.; Lee, Y.; Sun, S. H., Structurally Ordered FePt Nanoparticles and Their Enhanced Catalysis for Oxygen Reduction Reaction. *J. Am. Chem. Soc.* **2010,** *132* (14), 4996.

97. Li, Q.; Wu, L. H.; Wu, G.; Su, D.; Lv, H. F.; Zhang, S.; Zhu, W. L.; Casimir, A.; Zhu, H. Y.; Mendoza–Garcia, A.; Sun, S. H., New Approach to Fully Ordered fct−FePt Nanoparticles for Much Enhanced Electrocatalysis in Acid. *Nano Lett.* **2015,** *15* (4), 2468−2473.

98. Li, J. R.; Xi, Z.; Pan, Y. T.; Spendelow, J. S.; Duchesne, P. N.; Su, D.; Li, Q.; Yu, C.; Yin, Z. Y.; Shen, B.; Kim, Y. S.; Zhang, P.; Sun, S. H., Fe Stabilization by Intermetallic $L1_0$−FePt and Pt Catalysis Enhancement in $L1_0$−FePt/Pt Nanoparticles for Efficient Oxygen Reduction Reaction in Fuel Cells. *J. Am. Chem. Soc.* **2018,** *140* (8), 2926−2932.

99. Liu, Y.; Jiang, Y. H.; Zhang, X. L.; Wang, Y. X.; Zhang, Y. J.; Liu, H. L.; Zhai, H. J.; Liu, Y. Q.; Yang, J. H.; Yan, Y. S., Structural and magnetic properties of the ordered $FePt_3$, FePt and Fe_3Pt nanoparticles. *J. Solid State Chem.* **2014,** *209*, 69−73.

100. Liu, Y.; Jiang, Y. H.; Kadasala, N.; Zhang, X. L.; Mao, C. Y.; Wang, Y. X.; Liu, H. L.; Liu, Y. Q.; Yang, J. H.; Yan, Y. S., Effects of Au content on the structure and magnetic properties of $L1_0$−FePt nanoparticles synthesized by the sol−gel method. *J. Solid State Chem.* **2014,** *215*, 167−170.

101. Hong, S.; H. Yoo, M., Surface energy anisotropy of FePt nanoparticles. 2005, 97.

102. Wu, L. H.; Mendoza−Garcia, A.; Li, Q.; Sun, S. H., Organic Phase Syntheses of Magnetic Nanoparticles and Their Applications. *Chem. Rev.* **2016,** *116* (18), 10473−10512.

103. Rößner, L.; Armbrüster, M., Electrochemical Energy Conversion on Intermetallic Compounds: A Review. *ACS Catalysis* **2019,** *9* (3), 2018−2062.

104. Chung, D. Y.; Yoo, J. M.; Sung, Y. E., Highly Durable and Active Pt–Based Nanoscale Design for Fuel−Cell Oxygen−Reduction Electrocatalysts. *Adv. Mater.* **2018,** *30* (42), 1704123.

105. Yan, Y. C.; Du, J. S. S.; Gilroy, K. D.; Yang, D. R.; Xia, Y. N.; Zhang, H., Intermetallic Nanocrystals: Syntheses and Catalytic Applications. *Adv. Mater.* **2017,** *29* (14), 29.

106. Xiao, W.; Lei, W.; Gong, M.; Xin, H. L.; Wang, D., Recent Advances of Structurally Ordered Intermetallic Nanoparticles for Electrocatalysis. *ACS Catalysis* **2018,** *8* (4), 3237−3256.

107. Wang, D. L.; Xin, H. L. L.; Hovden, R.; Wang, H. S.; Yu, Y. C.; Muller, D. A.; DiSalvo, F. J.; Abruna, H. D., Structurally ordered intermetallic platinum−cobalt core−shell nanoparticles with enhanced activity and stability as oxygen reduction electrocatalysts. *Nat. Mater.* **2013,** *12* (1), 81−87.

108. Chen, X.; Wang, H.; Wan, H.; Wu, T.; Shu, D.; Shen, L.; Wang, Y.; Ruterana, P.; Lund, P. D.; Wang, H., Core/shell Cu/FePtCu nanoparticles with face–centered tetragonal texture: An active and stable low−Pt catalyst for enhanced oxygen reduction. *Nano Energy* **2018,** *54*, 280−287.

109. He, J.; Bian, B.; Zheng, Q.; Du, J.; Xia, W. X.; Zhang, J.; Yan, A.; Liu, J. P., Direct chemical synthesis of well disperse $L1_0$−FePt Nanoparticles with tunable size and coercivity. *Green Chem.* **2016,** *18*, 417.

110. Thanh, N. T. K.; Maclean, N.; Mahiddine, S., Mechanisms of Nucleation and Growth of Nanoparticles in Solution. *Chem. Rev.* **2014,** *114* (15), 7610−7630.

111. Chou, S. W.; Zhu, C. L.; Neeleshwar, S.; Chen, C. L.; Chen, Y. Y.; Chen, C. C., Controlled Growth and Magnetic Property of FePt Nanostructure: Cuboctahedron, Octapod, Truncated Cube, and Cube. *Chem. Mater.* **2009,** *21* (20), 4955−4961.

112. Xia, Y. N.; Gilroy, K. D.; Peng, H. C.; Xia, X. H., Seed−Mediated Growth of Colloidal Metal Nanocrystals. *Angew. Chem. Int. Edit.* **2017,** *56* (1), 60−95.

113. Guo, S. J.; Zhang, S.; Su, D.; Sun, S. H., Seed−Mediated Synthesis of Core/Shell FePtM/FePt (M = Pd, Au) Nanowires and Their Electrocatalysis for Oxygen Reduction Reaction. *J. Am. Chem. Soc.* **2013,** *135* (37), 13879−13884.

114. Sun, X.; Li, D.; Guo, S.; Zhu, W.; Sun, S., Controlling core/shell Au/FePt nanoparticle electrocatalysis via changing the core size and shell thickness. *Nanoscale* **2016,** *8* (5), 2626−2631.

115. Figueroa–Cosme, L.; Gilroy, K. D.; Yang, T. H.; Vara, M.; Park, J. H.; Bao, S. X.; da Silva, A. G. M.; Xia, Y. N., Synthesis of Palladium Nanoscale Octahedra through a One−Pot, Dual−Reductant Route and Kinetic Analysis. *Chem. Eur. J.* **2018,** *24* (23), 6133−6139.

116. Reichardt, C., Solvents and Solvent Effects in Organic Chemistry,Third Edition. *WILEY–VCH* **2003**.

117. Yang, T. H.; Gilroy, K. D.; Xia, Y. N., Reduction rate as a quantitative knob for achieving deterministic synthesis of colloidal metal nanocrystals. *Chem. Sci.* **2017,** *8* (10), 6730−6749.

118. Chen, X.; Wang, Y.; Wang, H. B.; Shu, D.; Zhang, J.; Ruterana, P.; Wang, H., Direct one−pot synthesis of $L1_0$−FePtAg nanoparticles with uniform and very small particle sizes. *J. Mater. Chem. C* **2017,** *5* (22), 5316−5322.

119. Sun, S.; Murray, C. B.; Weller, D.; Folks, L.; Moser, A., Monodisperse FePt Nanoparticles and Ferromagnetic FePt Nanocrystal Superlattices. *Science* **2000,** *287* (5460), 1989.

120. Sun, S.; Zeng, H., Size−Controlled Synthesis of Magnetite Nanoparticles. *J. Am. Chem. Soc.* **2002,** *124* (28), 8204−8205.

121. Sun, S.; Anders, S.; Thomson, T.; Baglin, J. E. E.; Toney, M. F.; Hamann, H. F.; Murray, C. B.; Terris, B. D., Controlled Synthesis and Assembly of FePt Nanoparticles. *The J. Phys. Chem. B* **2003,** *107* (23), 5419−5425.

122. Wang, D. Y.; Chou, H. L.; Cheng, C. C.; Wu, Y. H.; Tsai, C. M.; Lin, H. Y.; Wang, Y. L.; Hwang, B. J.; Chen, C. C., FePt nanodendrites with high−index facets as active electrocatalysts for oxygen reduction reaction. *Nano Energy* **2015,** *11*, 631−639.

123. Guo, S. J.; Li, D. G.; Zhu, H. Y.; Zhang, S.; Markovic, N. M.; Stamenkovic, V. R.; Sun, S. H., FePt and CoPt Nanowires as Efficient Catalysts for the Oxygen Reduction Reaction. *Angew. Chem. Int. Edit.* **2013,** *52* (12), 3465−3468.

124. Yang, J. H.; Jiang, Y. H.; Liu, Y.; Zhang, X. L.; Wang, Y. X.; Zhang, Y. J.; Wang, J.; Li, W.; Cheng, X., Effects of SiO_2 content on the structure and magnetic properties of $L1_0$−FePt nanoparticles synthesized by the sol−gel method. *Mater. Lett.* **2013,** *91*, 348−351.

125. Kang, S.; Harrell, J. W.; Nikles, D. E., Reduction of the fcc to $L1_0$ ordering temperature for self–assembled FePt nanoparticles containing Ag. *Nano Lett.* **2002,** *2* (10), 1033−1036.

126. Kang, S. S.; Nikles, D. E.; Harrell, J. W., Synthesis, chemical ordering, and magnetic properties of self−assembled FePt−Ag nanoparticles. *J. Appl. Phys.* **2003,** *93* (10), 7178−7180.

127. Wang, H. B.; Shang, P. J.; Zhang, J.; Guo, M. W.; Mu, Y. P.; Li, Q.; Wang, H., One−Step Synthesis of High−Coercivity $L1_0$−FePtAg Nanoparticles: Effects of Ag on the Morphology and Chemical Ordering of FePt Nanoparticles. *Chem. Mater.* **2013,** *25* (12), 2450−2454.

128. Zafiropoulou, I.; Tzitzios, V.; Boukos, N.; Niarchos, D., Ordering kinetics of chemically synthesized FePt nanoparticles. *J. Magn. Magn. Mater.* **2007,** *316* (2), 169−172.

129. Tzitzios, V.; Basina, G.; Colak, L.; Niarchos, D.; Hadjipanayis, G., Direct chemical synthesis of $L1_0$ FePt nanoparticles. *J. Appl. Phys.* **2011,** *109* (7), 07A718.

130. Tzitzios, V.; Basina, G.; Tzitzios, N.; Alexandrakis, V.; Hu, X. C.; Hadjipanayis, G., Direct liquid phase synthesis of ordered $L1_0$ FePt colloidal particles with high coercivity using an Au nanoparticle seeding approach. *New J. Chem.* **2016,** *40* (12), 10294−10299.

131. Liu, Y.; Jiang, Y. H.; Kadasala, N.; Zhang, X. L.; Mao, C. Y.; Wang, Y. X.; Liu, H. L.; Jiang, X. N.; Yang, J. H.; Yan, Y. S., Effects of Cu addition on the structure and magnetic properties of $L1_0$−FePt nanoparticles prepared by sol–gel method. *J. Sol−Gel Sci. Technol.* **2014,** *72* (1), 156−160.

132. Kang, S. S.; Jia, Z. Y.; Nikles, D. E.; Harrell, J. W., Synthesis, self−assembly, and magnetic properties of $FePt_{(1-x)}Au_x$ nanoparticles. *IEEE Trans. Magn.* **2003,** *39* (5), 2753−2757.

133. Kinge, S.; Gang, T.; Naber, W. J. M.; Boschker, H.; Rijnders, G.; Reinhoudt, D. N.; van der Wiel, W. G., Low−Temperature Solution Synthesis of Chemically Functional Ferromagnetic FePtAu Nanoparticles. *Nano Lett.* **2009,** *9* (9), 3220−3224.

134. Yu, Y. S.; Mukherjee, P.; Tian, Y.; Li, X. Z.; Shield, J. E.; Sellmyer, D. J., Direct chemical synthesis of $L1_0$–FePtAu nanoparticles with high coercivity. *Nanoscale* **2014,** *6* (20), 12050−12055.

135. Inaba, M.; Quinson, J.; Bucher, J. R.; Arenz, M., On the Preparation and Testing of Fuel Cell Catalysts Using the Thin Film Rotating Disk Electrode Method. *Jove−Journal of Visualized Experiments* **2018,** (133), 10.

136. Inaba, M.; Quinson, J.; Arenz, M., pH matters: The influence of the catalyst ink on the oxygen reduction activity determined in thin film rotating disk electrode measurements. *J. Power Sources* **2017,** *353*, 19−27.

137. Wakabayashi, R. H.; Paik, H.; Murphy, M. J.; Schlom, D. G.; Brutzam, M.; Uecker, R.; van Dover, R. B.; DiSalvo, F. J.; Abruna, H. D., Rotating Disk Electrode Voltammetry of Thin Films of Novel Oxide Materials. *J. Electrochem. Soc.* **2017,** *164* (14), 1154−1160.

138. Wang, W.; Wang, Z. Y.; Yang, M. M.; Zhong, C. J.; Liu, C. J., Highly active and stable Pt(111) catalysts synthesized by peptide assisted room temperature electron reduction for oxygen reduction reaction. *Nano Energy* **2016,** *25*, 26−33.

139. Wang, C.; Daimon, H.; Onodera, T.; Koda, T.; Sun, S., A General Approach to the Size− and Shape−Controlled Synthesis of Platinum Nanoparticles and Their Catalytic Reduction of Oxygen. *Angew. Chem.* **2008,** *120* (19), 3644−3647.

140. Guo, S. J.; Zhang, S.; Sun, S. H., Tuning Nanoparticle Catalysis for the Oxygen Reduction Reaction. *Angew. Chem. Int. Edit.* **2013,** *52* (33), 8526−8544.

141. Martens, S.; Asen, L.; Ercolano, G.; Dionigi, F.; Zalitis, C.; Hawkins, A.; Bonastre, A. M.; Seidl, L.; Knoll, A. C.; Sharman, J.; Strasser, P.; Jones, D.; Schneider, O., A comparison of rotating disc electrode, floating electrode technique and membrane electrode assembly measurements for catalyst testing. *J. Power Sources* **2018,** *392,* 274−284.

142. Shinozaki, K.; Zack, J. W.; Pylypenko, S.; Pivovar, B. S.; Kocha, S. S., Oxygen Reduction Reaction Measurements on Platinum Electrocatalysts Utilizing Rotating Disk Electrode Technique II. Influence of Ink Formulation, Catalyst Layer Uniformity and Thickness. *J. Electrochem. Soc.* **2015,** *162* (12), 1384−1396.

143. Garsany, Y.; Baturina, O. A.; Swider−Lyons, K. E.; Kocha, S. S., Experimental Methods for Quantifying the Activity of Platinum Electrocatalysts for the Oxygen Reduction Reaction. *Anal. Chem.* **2010,** *82* (15), 6321−6328.

144. Shinozaki, K.; Zack, J. W.; Richards, R. M.; Pivovar, B. S.; Kocha, S. S., Oxygen Reduction Reaction Measurements on Platinum Electrocatalysts Utilizing Rotating Disk Electrode Technique I. Impact of Impurities, Measurement Protocols and Applied Corrections. *J. Electrochem. Soc.* **2015,** *162* (10), 1144−1158.

145. Williams, D. B.; Carter, C. B., Transmission Electron Microscopy A Textbook for Materials Science. **2009**.

146. Reimer, L., Transmission electron Microscopy. *Springer* **1984,** *1st edition*.

147. Zhou, D., Aberration−Corrected Analytical Transmission Electron Microscopy of Light Elements in Complex Oxides: Application and Methodology. **2015**.

148. Wang, Y., Misfit dislocation and strain relaxation at large lattice mismatched III−V semiconductor interfaces, PhD thesis, **2013**.

149. Liao, Y., Practical Electron Microscopy and Database, www.globalsino.com/EM/ **2018**.

150. Williams, D. B.; Carter, C. B., Transmission Electron Microscopy, a text book for materials science *Springer* **2009,** *2nd Edition*.

151. Cowley, J. M., Diffraction Physics, 3rd Edition, North Holland **1995**.

152. Wang, Y.; Salzberger, U.; Sigle, W.; Suyolcu, Y. E.; van Aken, P. A., Oxygen octahedra picker: A software tool to extract quantitative information from STEM images. *Ultramicroscopy* **2016,** *168,* 46−52.

153. Jones, L.; Yang, H.; Pennycook, T. J.; Marshall, M. S. J.; Van Aert, S.; Browning, N. D.; Castell, M. R.; Nellist, P. D., Smart Align−a new tool for robust non−rigid registration of scanning microscope data. *Adv. Struct. Chem. Imag.* **2015,** *1* (1), 8.

154. Wang, Y.; Suyolcu, Y. E.; Salzberger, U.; Hahn, K.; Srot, V.; Sigle, W.; van Aken, P. A., Correcting the linear and nonlinear distortions for atomically resolved STEM spectrum and diffraction imaging. *Microscopy* **2018,** *67,* 9.

155. Wang, Y.; Huang, M. R. S.; Salzberger, U.; Hahn, K.; Sigle, W.; van Aken, P. A., Towards atomically resolved EELS elemental and fine structure mapping via multi−frame and energy−offset correction spectroscopy. *Ultramicroscopy* **2018,** *184*, 98−105.

156. Zhang, T.; Liedl, T., DNA−Based Assembly of Quantum Dots into Dimers and Helices. *Nanomaterials* **2019,** *9* (3), 10.

157. Hayashi, Y., Pot economy and one−pot synthesis. *Chem. Sci.* **2016,** *7* (2), 866−880.

158. Ferrer, D. A.; Guchhait, S.; Liu, H.; Ferdousi, F.; Corbet, C.; Xu, H.; Doczy, M.; Bourianoff, G.; Mathew, L.; Rao, R.; Saha, S.; Ramon, M.; Ganguly, S.; Markert, J. T.; Banerjee, S. K., Origin of shape anisotropy effects in solution–phase synthesized FePt nanomagnets. *J. Appl. Phys.* **2011,** *110* (1), 014316.

159. Chi, K. M.; Chen, P. Y., Solvent−Dependent, Low−Temperature Solution Phase Synthesis of FePt Nanowires. *J. Nanosci. Nanotechnol.* **2008,** *8* (7), 3379−3385.

160. Hsu, Y. N.; Jeong, S.; Laughlin, D. E.; Lambeth, D. N., Effects of Ag underlayers on the microstructure and magnetic properties of epitaxial FePt thin films. *J. Appl. Phys.* **2001,** *89* (11), 7068−7070.

161. Xu, X. H.; Wu, H. S.; Wang, F.; Li, X. L., The effect of Ag and Cu underlayer on the L10 ordering FePt thin films. *Appl. Surf. Sci.* **2004,** *233* (1), 1−4.

162. Kang, K.; Zhang, Z. G.; Papusoi, C.; Suzuki, T., (001) oriented FePt−Ag composite nanogranular films on amorphous substrate. *Appl. Phys. Lett.* **2003,** *82* (19), 3284−3286.

163. Zhao, Z. L.; Ding, J.; Inaba, K.; Chen, J. S.; Wang, J. P., Promotion of $L1_0$ ordered phase transformation by the Ag top layer on FePt thin films. *Appl. Phys. Lett.* **2003,** *83* (11), 2196−2198.

164. Chen, J. S.; Zhou, Y. Z.; Sun, C. J.; Han, S. W.; Chow, G. M., Where is the Ag in FePt–Ag composite films? *Appl. Phys. Lett.* **2011,** *98* (13), 131914.

165. Chepulskii, R. V.; Curtarolo, S., First principles study of Ag, Au, and Cu surface segregation in FePt−$L1_0$. *Appl. Phys. Lett.* **2010,** *97* (22), 221908.

166. Wang, L.; Gao, T.; Yu, Y., Effects of Ag addition on FePt $L1_0$ ordering transition: A direct observation of ordering transition and Ag segregation in FePtAg alloy films. *J. Appl. Phys.* **2015,** *118* (23), 235304.

167. Yang, W.; Gao, Z.; Ma, J.; Wang, J.; Wang, B.; Liu, L., Effects of solvent on the morphology of nanostructured Co_3O_4 and its application for high–performance supercapacitors. *Electrochim. Acta* **2013,** *112*, 378−385.

168. Gilbert, D.; Wang, L. W.; Klemmer, T.; Thiele, J. U.; Lai, C. H.; Liu, K., Tailoring anisotropy in (001) oriented $(Fe_{1-x}Cu_x)_{55}Pt_{45}$ films. **2013**, 16002.

169. Barmak, K.; Kim, J.; Berry, D. C.; Wierman, K. W.; Svedberg, E. B.; Howard, J. K., Calorimetric studies of the A_1 to $L1_0$ transformation in FePt and related ternary alloy thin films. *J. Appl. Phys.* **2004,** *95* (11), 7486−7488.

170. Platt, C. L.; Wierman, K. W.; Svedberg, E. B.; van de Veerdonk, R.; Howard, J. K.; Roy, A. G.; Laughlin, D. E., $L1_0$ ordering and microstructure of FePt thin films with Cu, Ag, and Au additive. *J. Appl. Phys.* **2002,** *92* (10), 6104−6109.

171. Maeda, T.; Kai, T.; Kikitsu, A.; Nagase, T.; Akiyama, J. i., Reduction of ordering temperature of an FePt–ordered alloy by addition of Cu. *Appl. Phys. Lett.* **2002,** *80* (12), 2147−2149.

172. Takahashi, Y. K.; Ohnuma, M.; Hono, K., Effect of Cu on the structure and magnetic properties of FePt sputtered film. *J. Magn. Magn. Mater.* **2002,** *246*, 259−265.

173. Sun, X.; Kang, S.; Harrell, J. W.; Nikles, D. E.; Dai, Z. R.; Li, J.; Wang, Z. L., Synthesis, chemical ordering, and magnetic properties of FePtCu nanoparticle films. *J. Appl. Phys.* **2003,** *93* (10), 7337−7339.

174. Wang, R. M.; Dmitrieva, O.; Farle, M.; Dumpich, G.; Ye, H. Q.; Poppa, H.; Kilaas, R.; Kisielowski, C., Layer Resolved Structural Relaxation at the Surface of Magnetic FePt Icosahedral Nanoparticles. *Phys. Rev. Lett.* **2008,** *100* (1), 017205.

175. Gan, L.; Cui, C.; Heggen, M.; Dionigi, F.; Rudi, S.; Strasser, P., Element–specific anisotropic growth of shaped platinum alloy nanocrystals. *Science* **2014,** *346* (6216), 1502−1506.

Etude de la transformation de phase dans les nanoparticules FePtM n(M= Ag, Cu) à l'échelle atomique pour la catalyse optimisée de la réduction de l'oxygène

Les piles à combustible à membrane échangeuse de protons sont prometteuses en tant que nouveaux dispositifs de conversion d'énergie en raison de leur rendement élevé et de leur faible impact sur l'environnement. Cependant, les charges de Pt nécessaires pour compenser la mauvaise cinétique de la réaction de réduction de l'oxygène entravent leurs applications à grande échelle. Récemment, il est devenu possible d'améliorer l'activité des catalyseurs en exploitant des effets géométriques et/ou électroniques. Ainsi, les alliages binaires à base de Pt avec une structure ordonnée ont-ils montré une activité et une durabilité améliorées. Ce travail a étudié des nanoparticules FePtAg et FePtCu ordonnées issues de la synthèse « one–pot ». Pour FePtAg, nous avons démontré que la transformation vers la structure ordonnée était induite par le dopage Ag; une coercivité de 5.23 kOe et des nanoparticules de FePtAg de taille ultrafine (3.5 ± 0.5 nm) ont été obtenues. Pour les nanoparticules FePtCu, l'effet d'alliage de Cu s'est avéré constituer la force motrice pour la mise en ordre. En comparaison avec le Pt/C de référence, nos nanoparticules de Cu/FePtCu à structure noyau/coquille optimisées présentent une activité massique 4 fois supérieure avec une atténuation en durabilité de seulement 3% contre 34.2%. Enfin, une activité massique supérieure de 11.7 fois à celle de Pt/C a été obtenue pour des nanoparticules de FePtCu avec une structure cœur/coquille Cu/FePt en forme d'octaèdres tronqués.

Mots-clés: FePt, FePtAg, FePtCu, Microscopie électronique à transmission, Oxydo réduction, Electrocatalyse, Magnétisme, Mise en ordre

Investigation of the Phase transformation in FePtM nanoparticles (M= Ag, Cu) at atomic scale for optimized oxygen reduction catalysis

Proton exchange membrane fuel cells are promising as novel energy conversion devices due to their high efficiency and low environmental impact. However, the platinum loadings needed for compensating the poor kinetics in the oxygen reduction reaction hinder their widespread applications in new energy vehicles and stations. Recently, it has become possible to enhance the catalysts activity based on geometrical and/or electronic effects. In this vein, Pt−based binary alloys with ordered structure have demonstrated enhanced activity and durability, while, contributing to decrease the weight of Pt. In this work, we have investigated ordered FePtAg and FePtCu nanoparticles from one–pot synthesis, with the objective to develop high performance catalysts by improving their activity and durability. In FePtAg, the phase transition to ordered structure was shown to be induced by Ag doping; a high coercivity of 5.23 kOe and ultrafine size FePtAg nanoparticles (3.5 ± 0.5 nm) has been achieved. For the FePtCu nanoparticles, the Cu alloying effect was found to constitute the driving force for ordering. As related to benchmark Pt/C, our optimized core–shell structured Cu/FePtCu nanoparticles exhibited a mass activity 4 times higher with only 3 % durability attenuation in contrast to 34.2% for Pt/C catalyst. Finally, a mass activity of 11.7 times larger than Pt/C was achieved for optimized FePtCu nanoparticles, with core–shell Cu/FePt structure and truncated–octahedron shape.

Keywords: FePt, FePtAg, FePtCu, TEM, ORR, Electrocatalysis, Magnetism, Ordering